creative commons
COMMONS DEED

저작자표시-비영리-변경금지 2.0 대한민국

이용자는 아래의 조건을 따르는 경우에 한하여 자유롭게

- 이 저작물을 복제, 배포, 전송, 전시, 공연 및 방송할 수 있습니다.

다음과 같은 조건을 따라야 합니다:

**저작자표시**. 귀하는 원저작자를 표시하여야 합니다.

**비영리**. 귀하는 이 저작물을 영리 목적으로 이용할 수 없습니다.

**변경금지**. 귀하는 이 저작물을 개작, 변형 또는 가공할 수 없습니다.

- 귀하는, 이 저작물의 재이용이나 배포의 경우, 이 저작물에 적용된 이용허락조건을 명확하게 나타내어야 합니다.
- 저작권자로부터 별도의 허가를 받으면 이러한 조건들은 적용되지 않습니다.

**저작권법에 따른 이용자의 권리는 위의 내용에 의하여 영향을 받지 않습니다.**

이것은 이용허락규약(Legal Code)을 이해하기 쉽게 요약한 것입니다.

Disclaimer

dCollection

이학박사 학위논문

# Studies on Quantum Magnetism in Novel $Cu^{2+}$ Oxides

## 새로운 구리 2+ 산화물을 기반으로 한 양자 자성 연구

2019 년 2 월


서울대학교 대학원

물리천문학부 물리학전공

조 환 범

# Studies on Quantum Magnetism in Novel $Cu^{2+}$ Oxides

새로운 구리 2+ 산화물을 기반으로 한 양자 자성 연구

지도교수 박 제 근

이 논문을 이학박사 학위논문으로 제출함
2019 년 2 월

서울대학교 대학원
물리천문학부
조 환 범

조환범의 이학박사 학위논문을 인준함
2018 년 12 월

위 원 장 김 기 훈 (인)
부위원장 박 제 근 (인)
위 원 박 철 환 (인)
위 원 김 도 헌 (인)
위 원 Yukio Noda (인)

# Abstract

In condensed matter physics, quantum magnetism is an intriguing field focused on novel phenomena, which could not be expected from classical formalisms but is driven by strong quantum mechanical fluctuations. Especially, cuprate systems, which have the oxidization of 2+, have been a promising playground to study quantum magnetism such as quantum spin liquid, a *uud* phase transitions in triangular lattice antiferromagnets, and the breakdown of electrons into spinons, holons, and orbitons because of strong quantum fluctuations from the spin-$S$ = 1/2 and the large coulomb interaction. In this thesis, I succeeded to find novel phenomena relating to the interplay of the strong quantum fluctuations and electron correlation by studying several new cuprate systems: $CuAl_2O_4$ and $CuR_2Ge_2O_8$ ($R$ = Y, La).

The main question of my thesis is how to realize a spin-orbital entangled pseudo-spin state, $J_{eff}$ = 1/2 with $Cu^{2+}$. Although the spin-orbital entangled state been an intriguing topic in condensed matter physics due to related emergent phenomenon such as Kitaev quantum spin liquid, there have been less studies on 3*d* transition metal oxides because the spin-orbital coupling constant of 3*d* ion is smaller than that of Ru (4*d*) or Ir (5*d*) ions. In this work, I show that a cuprate system, $CuAl_2O_4$ hosts a $J_{eff}$ = 1/2 state. Cubic symmetry of the crystal structure verified by x-ray diffraction and Cu K-edge x-ray absorption supports the $J_{eff}$ = 1/2 of $CuAl_2O_4$. X-ray absorption on Cu L-edge also gives direct evidence for the emergence of this state. Moreover, the site inversion of the system and the strong quantum

fluctuations of the frustrated $J_{eff}$ = 1/2 wavefunctions leads to the absence of a long-range order with a possible glassy state from the spin-orbital entangled $J_{eff}$ = 1/2 state.

Following studies are focused on new two-dimensional (2D) quantum ($S$ = 1/2) antiferromagnetic systems: Cu$R_2$Ge$_2$O$_8$ ($R$ = Y and La). According to the analysis of high-resolution x-ray and neutron diffraction experiments, the Cu network of Cu$R_2$Ge$_2$O$_8$ ($R$ = Y and La) exhibits a 2D triangular lattice linked via weak bonds along the perpendicular $b$ axis. Bulk characterizations from 0.08 to 400 K show that they undergo long-range order at 0.51(1) and 1.09(4) K for the Y and La systems, respectively. Interestingly, they also exhibit unusual phase transitions induced by magnetic field. For theoretical understanding, the density functional theory (DFT) band calculations were carried out to find that they are typical charge-transfer-type insulators with a gap of $E_g \cong 2$ eV. Taken together, these observations make Cu$R_2$Ge$_2$O$_8$ ($R$ = Y and La) additional examples of two-dimensional quantum spin triangular antiferromagnets with the low-temperature magnetic ordering.

**Keywords:** quantum magnetism, Mott insulator, spin-orbital coupling, frustration, cuprate, spinel, triangular lattice, sample synthesis.

**Student Number:** 2013-20384

**Abstract** ..... **i**

**List of Tables** ..... **vii**

**List of Figures** ..... **ix**

**1 Introduction** ..... **1**

1.1 Quantum spin systems ..... 1

1.1.1 Large quantum fluctuation ..... 1

1.1.2 Novel phenomena in quantum spin systems ..... 2

1.2 Outline of thesis ..... 10

**2 Experimental Techniques** ..... **16**

2.1 Sample synthesis ..... 16

2.1.1 Flux method ..... 16

2.1.2 Solid state reaction method ..... 19

2.2 Crystal structure analysis ..... 21

2.2.1 X-ray diffraction ..... 21

2.2.2 Rietveld refinement ..... 25

**3 Emergence of Spin-Orbital Entangled $J_{eff}$ = 1/2 state in $CuAl_2O_4$** ..... **29**

3.1 Spin-orbital entangled Kramers doublet $J_{eff}$ = 1/2 ..... 29

3.1.1 Nature of $J_{eff}$ = 1/2 ..... 29

3.1.2 Novel phenomena in $J_{eff}$ = 1/2 compounds ..... 30

3.2 $J_{eff}$ = 1/2 in a 3*d* compound ..... 32

3.2.1 Conditions to induce $J_{eff}$ = 1/2 in a 3*d* compound ..... 32

3.2.2 Candidate materials: $CuAl_2O_4$ ..... 34

3.3 XAS simulation for $CuAl_2O_4$ ..... 38

3.4 XAS experiment on $CuAl_2O_4$ ..... 40

3.5 Discussion and summary ..... 45

3.5.1 Magnetism of $CuAl_2O_4$ ..... 45

3.5.2 Summary ..... 55

**4 Properties of *S* = 1/2 Triangular-Lattice Antiferromagnets $CuY_2Ge_2O_8$ and $CuLa_2Ge_2O_8$ ..... 60**

4.1 Quantum 2D triangular lattice ..... 60

4.1.1 Enhancement of quantum fluctuation effects in 2D quantum triangular lattice ..... 60

4.1.2 Quantum phase trnasitions in 2D triangular HAFM driven by quantum fluctuations ..... 62

4.1.3 Candidate material for 2D triangular HAFM: $CuR_2Ge_2O_8$ (*R* = Y, La) 63

4.2 Crystal structure of $CuR_2Ge_2O_8$ (*R* = Y, La) ..... 64

4.3 Bulk properties of CuR2Ge2O8 (*R* = Y, La) ..... 68

4.3.1 Magnetic measurements ..... 68

4.3.2 Heat capacity measurements ..... 73

4.3.3 DFT calculation ..... 75

4.4 Discussion and summary ..... 77

4.4.1 Novel quasi 2D triangular lattice: Cu$R_2Ge_2O_8$ ..... 77

4.4.2 Summary ..... 79

**5 Outlook and Summary ..... 86**

5.1 Outlook ..... 86

5.2 Summary ..... 87

**Appendix: Electric Dipole Transitions ..... 89**

**Publication lists ..... 105**

**(Abstract in Korean) ..... 107**

**(Acknowledgement) ..... 111**

# List of Tables

2.1 The summary of the crystal structure of $CuLa_2Ge_2O_8$ ..... 26

2.2 The crystal structure of $CuAl_2O_4$ ..... 27

3.1 The profile of the each fitted peak in FIG.3.10 ..... 44

3.2 Comparison of the parameters of simulation and experiment ..... 44

# List of Figures

1.1 Valence-bond states of frustrated antiferromagnets from [Ref.1.6] ..... 3

1.2 (Left) Crystal structure of herbertsmithite looking down along the hexagonal c axis. Copper atoms are blue, oxygen (small) red, and zinc atoms are gray. (Right) Inelastic neutron scattering from the spin excitations, plotted in reciprocal space [Ref.1.5,12] ..... 5

1.3 (a) Kitaev honeycomb model. *x*, *y*, and *z* denote three types of links in the honeycomb lattice [Ref.1.13]. (b) Schematic diagram for thermal Hall effect provoked by Majorana edge current and (c) half-integer thermal Hall conductance measured in Ŭ-$RuCl_3$ [Ref.1.15] ..... 6

1.4 (Upper) The magnetic phase diagram of a triangular XXZ antiferromagnet on a 3ي6 lattice in [Ref.1.21]. The thin solid phase boundaries are calculated through finite-system diagonalizations and the solid ones are done via expansions around the Ising limit. (Lower) Magnetization curves of the *S* = 1/2 triangular lattice HAF with φ= 1 on 3ي6 (short dashes) in [Ref.1.21] ..... 9

1.5 The magnetization data for $Ba_3CoSb_2O_9$, which shows magnetic plateau where *M* = *M*s/3. The spin structure is depicted depending on the magnetic field [Ref.1.23] ..... 10

1.6 The process of spin-orbital separation in a spin chain $Sr_2CuO_3$ [Ref.1.28] ..... 11

2.1 $CuLa_2Ge_2O_8$ single-crystal growth using flux method ..... 17

2.2 Phase diagram of CuO-$Al_2O_3$ with different oxygen partial pressures: (left) $p_{o2}$ =

0.21 and (right) $p_{o2}$ = 0.4 atm [Ref.2.2] ..... 19

2.3 Schematic diagram for solid state reaction method and the phase diagram of CuO-$Y_2O_3$-$GeO_2$ [Ref.2.4] ..... 20

2.4 Picture of a high resolution single-crystal X-ray diffractometer (XtaLAB P200, Rigaku) used to verify single-crystal samples ..... 22

2.5 The refinement results of the single-crystal XRD data of (left) $CuLa_2Ge_2O_8$ and a picture of single-crystal sample taken using an optical microscope (inset), and (right) $CuAl_2O_4$ and a picture of a $CuAl_2O_4$ single-crystal (inset) ..... 23

2.6 The refinement results of the x-ray powder diffraction of Cu$R_2Ge_2O_8$ ($R$=Y and La) and neutron powder diffraction data of $CuY_2Ge_2O_8$ measured on the Echidna beamline, ANSTO ..... 24

3.1 Formation of $J_{eff}$ = 1/2 state in $Sr_2IrO_4$ from [Ref.3.1] ..... 30

3.2 Emergent phenomena in the $J_{eff}$ = 1/2 state (a) the crystal structure of $Sr_2IrO_4$ in [Ref.3.4] (b) the schematic diagram for Majorana fermion in Ŭ-$RuCl_3$ [Ref.3.7] (c) the energy bands in the plane $k_z = 0.6´/a$, where a Weyl point is predicted to exist in $Y_2Ir_2O_7$ [Ref.3.8] ..... 32

3.3 $Cu^{2+}$ ion in tetrahedral CEF induces Mott insulating $J_{eff}$ = 1/2 ground state ..... 33

3.4 Crystal structure of $CuAl_2O_4$. The blue, grey, and red spheres represent Cu, Al, and O atoms, respectively. The $CuO_4$ tetrahedra form a diamond lattice ..... 34

3.5 (a) Copper K-edge and a simulation using FEFF8 software. (b) Comparison of spectra for two different polarizations ..... 35

3.6 (Left) A photo of a $CuAl_2O_4$ single crystal with two-wire contact. (Right) The resistance measurement data and (inset) the Arrhenius plot and its linear fit to estimate the activation energy ..... 37

3.7 XAS process of $Cu^{2+}$ in (a) tetrahedral A-site with $s$ = 1/2 state, (b) tetrahedral A-site with $j_{eff}$ = 1/2 state, and (c) octahedral B-site with $s$ = 1/2 state ..... 38

3.8 Simulation of XAS using CTM4XAS ..... 40

3.9 X-ray absorption spectroscopy data for $CuAl_2O_4$. (a) $L_3$ edge is composed of $t_2$ and $e_g$ contributions (peak Ŭand ɓ respectively) (b) $L_2$ edge is composed of $e_g$ contribution only (peak ɔ) ..... 41

3.10 (Upper) Experimental XAS data and the profile of each fitted peak. (Lower) The main three peaks by subtracting background and the humps from charge transfer transitions: 1, 2, 5 correspond to Ŭ, ɓ, ɔ ..... 43

3.11 The magnetic properties measurement for $CuAl_2O_4$ along the each crystallographic axis ..... 45

3.12 (Left) DC magnetic susceptibility down to 0.5 K using MPMS-XL equipped with $^3$He option. (Right) AC magnetic susceptibility varying the frequency of AC field [Ref.3.11] ..... 47

3.13 (a), (b) Asymmetry of $\varepsilon$SR experiment data at 0.1 and 4 K, respectively using a dilution refrigerator option. The red lines are fitting lines to the data using ôMantidô. (c), (d) Asymmetry data at 2.5 and 15 K, respectively using a cryostat option ..... 48

3.14 The fitting parameters of (a) $A_1$, (b) $\partial_1$, (c) $A_2$, (b) $\partial_2$, which are obtained by fitting the data from dilution refrigerator option and the fitting parameters of (e) $A_1$, (f) $\partial_1$, (g) $A_2$,

(h) $\partial_2$ from cryostat option ..... 50

3.15 (Upper) $^{27}$Al NMR spectra for single-crystal $CuAl_2O_4$ measured at 200 K under the external magnetic field of 2 T. The angle, $d$ between (111) and the field was rotated in the ($\rho\bar{\rho}0$) plane. The dashed line denotes the reference resonance line of $^{27}$Al and a sharp peak near 22.6 MHz comes from $^{63}$Cu in the NMR coil used for calibrating the magnetic field. (Lower) The temperature dependence of NMR spectra at 1.4, 4.2, 50, and 200 K under the external field of 2 T along (111) ..... 53

3.16 The field-cooled and zero-field-cooled spectra below and above $T_f$. Small two peaks are from $^{63}$Cu and $^{65}$Cu in the NMR coil, respectively ..... 54

4.1 Crystal structure of $CuLa_2Ge_2O_8$ in the $I1m1$ unit cell setting. The blue, green, and grey spheres indicate the copper, lanthanum, and germanium atoms, respectively ..... 67

4.2 Magnetic susceptibility and magnetization measurement for $CuR_2Ge_2O_8$ ($R$ = Y and La) ..... 69

4.3 Heat capacity $C_p(T)$ of $CuR_2Ge_2O_8$ ($R$ = Y and La) ..... 74

4.4 (a) The total density of states calculated using the crystal structure of $CuLa_2Ge_2O_8$ with the Coulomb interaction, $U$ = 5 eV. (b) The partial density of states projected on the copper $d$ orbitals ..... 76

4.5 Diagrams of magnetic lattices of selected inorganic quantum 2D triangular systems ..... 79

# Chapter 1
# Introduction

## 1.1 Quantum spin systems

### 1.1.1 Large quantum fluctuation

The fluctuations driven by thermal energy with large spins which are much larger than $S$ = 1/2 are called classical fluctuations. Spins can reorient randomly with time and cycle through different microstates. The classical fluctuation will perish and the spins will freeze or order when the temperature becomes too low. However, for small spins which are close to $S$ = 1/2, a zero-point motion, which persists down to $T$ = 0 K is produced by the uncertainty principle in quantum mechanics [Ref.1.1]. To get intuition that the effects of the quantum (spin) fluctuations are significant in a system with small spins, it is worthwhile to consider the following example. The studies on Heisenberg antiferromagnets on a face-centered cubic lattice with first- and second-nearest neighbor interactions $J$ and $J_2$ show that the quantum fluctuations modify the low-energy spin waves and eventually destroy the long-range order when $J_2/J$=2 [Ref.1.2]. The modified spin-waves due to quantum fluctuations can be modeled by an effective biquadratic interactions of the form:

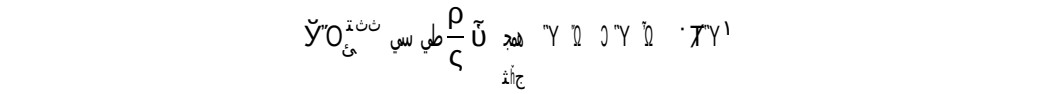

Accordingly, in order to enlarge the effects from the quantum fluctuations, which is of order (1/*S*) the value of spin angular momentum of a system should be small as *S* = 1/2 or 1. Quantum spin systems, therefore, are usually regarded to have small spin moments, inducing substantial effects due to quantum fluctuations.

## 1.1.2 Novel phenomena in quantum spin systems

The study of magnetic systems, where the effects of quantum spins play a dominant role and need to be explained in detail, has evolved into a very active field of research for decades [Ref.1.3]. First of all, P. W. Anderson suggested that on the *S* = 1/2 square lattice, quantum fluctuations could melt the Néel order in two dimensions [Ref.1.4,5]. For spin-1/2 systems with the superexchange interaction of *J*, the energy to form a singlet bond is -3*J*/8 and this energy is lower than that of a Néel bond -*J*/4. Each spin in the singlet bonds is highly entangled with only one other in short range. Such a ground state is modeled as a product of the singlet (or valence) bonds [Ref.1.1]. This is known as a valence-bond solid (VBS) state (FIG.1.1 (a)). Anderson then speculated that the free energy could be further lowered if these singlet bonds resonated from one link of the lattice to the next like Paulingôs model for resonating carbon double bonds in a benzene ring [Ref.1.4-6]. In this picture, through the quantum fluctuations, the ground state wavefunction resonates among the various kinds of VBS states and therefore it has macroscopic quantum entanglement.

This type of the wavefuction is known as a valence-bond liquid or resonating valence-bond (RVB) state (FIG.1.1 (b)) [Ref.1.6]. Moreover, when a valence-bond is formed even at a long-range, the ground state is named a quantum spin liquid (QSL) state (FIG.1.1 (c)). Despite consisting of localized spins, QSL has a non-magnetic ground state and doesn't order even at $T = 0$ K since the spins continue to fluctuate [Ref.1.1,6]. Theoretically, QSLs are expected to show novel phenomena such as inducing exotic excitations with fractional quantum numbers, artificial gauge fields, and superconductivity [Ref.1.1,4,7,8].

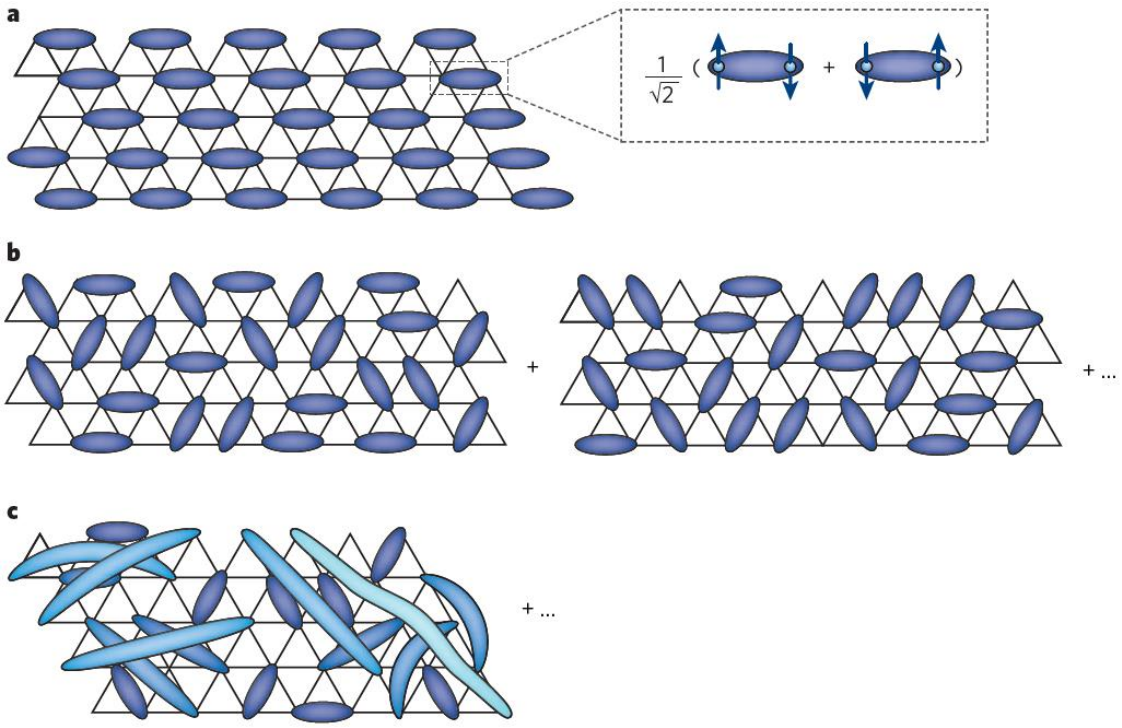


**FIG.1.1 Valence-bond states of frustrated antiferromagnets from [Ref.1.6]. (a) A valence bond solid (VBC) state approximated by a product of the short-ranged valence bonds (inset). (b) A resonating valence bond (RVB) state, formed by superposing various VBC states. (c) A quantum spin liquid (QSL) state with long-ranged valence-bonds.**

To realize QSLs in real materials, basically, spin angular momentum should be $S = 1/2$ and the Hubbard repulsion $U$ should be large enough to make the spins localized. In addition, the system ought to have geometrical frustration, which also enhances the effects of quantum fluctuations and prevents the spins from forming a simple Néel type order. There are only handful of systems reported so far to have QSL states: organic compounds $\kappa$-$(BEDT\text{-}TTF)_2Cu_2(CN)_3$ and $EtMe_3Sb[Pd(dmit)_2]_2$, which have two dimensional (2D) triangular Heisenberg antiferromagnet (HAF) [Ref.1.9,10]; and herbertsmithite $ZnCu_3(OH)_6Cl_2$, having 2D kagome HAF [Ref.1.11]. Especially, in case of herbertsmithite, the spin excitations at low temperature form a broad continuum instead of conventional spin waves expected in ordered antiferromagnets [Ref.1.12]. Such a continuum is a signature of fractional spin excitations, serving as a hallmark of the quantum spin liquid state in herbertsmithite.

So far, the QSLs have been treated in the spin only systems and coupling between spin and orbital degrees of freedom has been ignored [Ref.1.13]. Also, there was belief that spin rotational symmetry is mandatory to make QSL states and, if not, the system tends to approach an ordered state [Ref.1.13]. Kitaev, however, provided a counter example to this belief by suggesting an novel and exactly solvable model in 2D with strong spin-orbital coupling, which breaks the spin rotational symmetry, but producing deconfined spinons existing on top of the QSL ground states [Ref.1.13,14]. This model is called the Kitaev (honeycomb) model. Kitaev considered a spin-1/2 model on a honeycomb lattice with spin-orbital coupling [Ref.1.13,14]. In the honeycomb lattice, all nearest neighbor bonds were divided into three types: $x$ links, $y$ links, and $z$ links as shown in FIG.1.3.

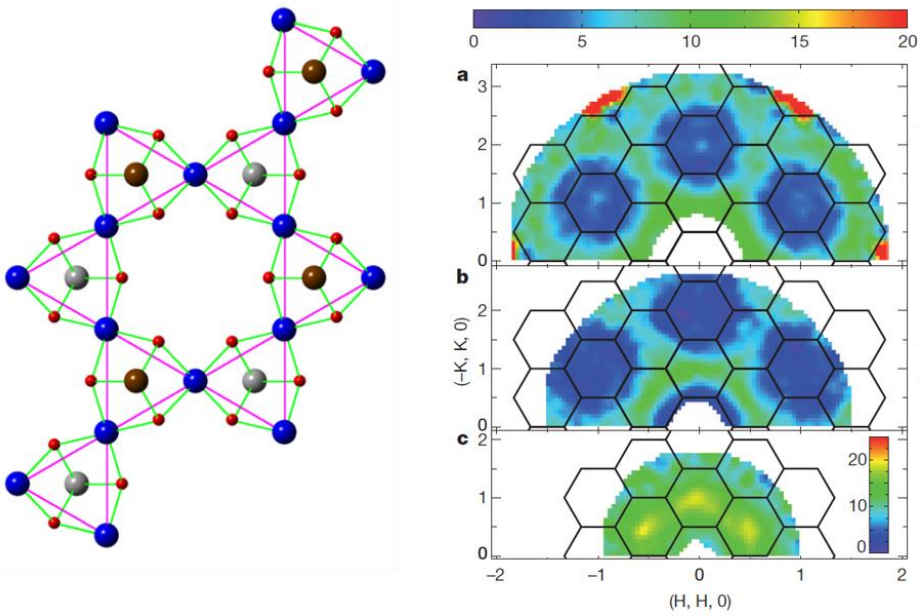


**FIG.1.2 (Left) Crystal structure of herbertsmithite looking down along the hexagonal *c* axis. Copper atoms are blue, oxygen (small) red, and zinc atoms are gray. (Right) Inelastic neutron scattering from the spin excitations, plotted in reciprocal space. [Ref.1.5,12]**

The Hamiltonian is given as follows [Ref.1.13]:

$$\mathcal{H} = \sum_{\langle ij \rangle_x} K_{ij} S_i^x S_j^x + \sum_{\langle ij \rangle_y} K_{ij} S_i^y S_j^y + \sum_{\langle ij \rangle_z} K_{ij} S_i^z S_j^z$$

where $K_{ij}$ is defined as

$$K_{ij} = \begin{cases} K_x & \text{if } \alpha_{ij} = x \\ K_y & \text{if } \alpha_{ij} = y \\ K_z & \text{if } \alpha_{ij} = z \end{cases}$$

Such Kitaev QSLs exhibit two types of fractionalized quasiparticle excitation: itinerant Majorana fermions and $Z_2$ fluxes with a gap [Ref.1.15]. In zero field, the Majorana fermion

has a massless (gapless) Dirac-type dispersion. A Majorana fermion system distinguished by the bulk gap and gapless edge modes can be, in principle, realized under magnetic fields, and the $Z_2$ flux obeys anionic statistics [Ref.1.14-16,]. As a candidate for Kitaev QSL, Ŭ-$RuCl_3$ has attracted recent interest in condensed matter physics. The Ŭ-$RuCl_3$ has a crystal structure of a 2D honeycomb lattice consisting of edge sharing $RuO_6$ octahedra, and the Ru-O-Ru boding angle is close to 90 degrees [Ref.1.17].

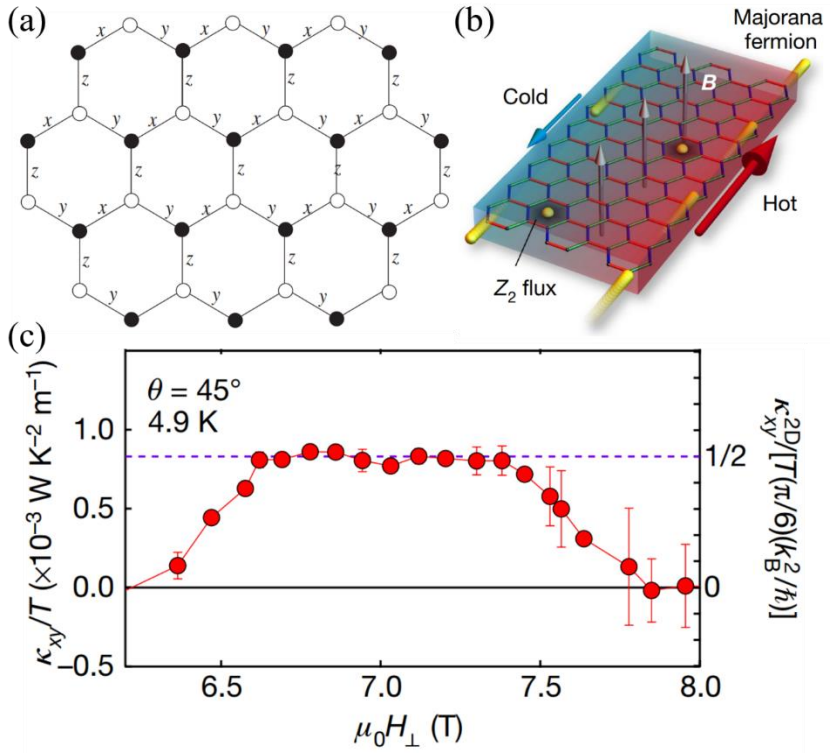


**FIG.1.3 (a) Kitaev honeycomb model. *x*, *y*, and *z* denote three types of links in the honeycomb lattice [Ref.1.13]. (b) Schematic diagram for thermal Hall effect provoked by Majorana edge current and (c) half-integer thermal Hall conductance measured in Ŭ-$RuCl_3$ [Ref.1.15].**

Since the $Ru^{3+}$ ion has a modest spin-orbital coupling (~0.1 eV) and Coulomb interaction $U \sim 1.5$ eV, the ground state is a spin-orbital entangled pseudo spin-$J_{eff} = 1/2$ Mott insulator [Ref.1.18]. Therefore, Ŭ-$RuCl_3$ meets criteria to be the Kitaev model: localized moment, sizable spin-orbital coupling, and ferromagnetic superexchange interaction to the three nearest neighbors. The thermal hall measurement is considered to be a direct tool to detect the fractionalization of the quantum spins [Ref.1.15]. In the Kitaev QSL state, spins are fractionalized into Majorana fermions and $Z_2$ fluxes, and the heat is carried by chiral edge currents of charge-neutral Majorana fermions with half integer thermal Hall conductance [Ref.1.15]. FIG.1.3 shows half-integer thermal Hall conductance measured in Ŭ-$RuCl_3$ [Ref.1.15].

Despite Andersonôs initial trial to find the ground state of 2D triangular HAF without a long-range order, many experimental and theoretical works show that the ground state is different from Andersonôs expectations. According to many studies on 2D triangular HAF, the ground state is ordered so that spins at the vertices of the triangle make 120 degrees to each other, and the quantum fluctuation may not be strong enough to destroy the order [Ref.1.19-22]. However, the quantum fluctuation plays a crucial role when external magnetic field is applied. The energy of quantum fluctuations varies with the magnetic field and it also depends on the spin structure. From these relations, there is a phase transition of the spin structure as the field changes [Ref.1.22]. As the field increases, a plateau emerges accompanying a phase transition from the 120Ástate to an up-up-down (*uud*) phase where $M = \frac{1}{3}Ms$ (*Ms*: the saturated magnetization) in the field dependent magnetization *M*(*H*) curve [Ref.1.20,21]. This behavior can be obtained by using a $S = 1/2$ *XXZ* model

Hamiltonian in ref.1.21:

$$\mathcal{H} = J \sum_{\langle ij \rangle} \frac{1}{2}\left(\sigma_i^+ \sigma_j^- + \sigma_i^- \sigma_j^+\right) + J_z \sum_{\langle ij \rangle} \sigma_i^z \sigma_j^z - h \sum_i \sigma_i^z$$

where the $\sigma_i$ are spin-1/2 operators acting at $i$ and $h$ is a dimensionless magnetic field. The magnetization $\langle M \rangle$ is given by the expectation value of the operator $\frac{1}{V}\sum_i \sigma_i^z$ ($V$ is the total number of the sites on a lattice). The magnetization operator $M$ commutes with the Hamiltonian. Therefore, the energy eigenvalues should be quantized as the eigenvalues of the $\sigma_i$. According to further calculation via finite-system diagonalizations [Ref.1.21], a 3×6 lattice makes the magnetic phase diagram which is partitioned by thin curves. Since there are 18 spin-1/2 and the flipping of a single spin changes $\langle M \rangle$ by $2/V$, the phase diagram of $\langle M \rangle$ are quantized by 1/9 in FIG1.4. From the phase diagram, the magnetization curve shows 1/3 plateau step-like features even in case of the Heisenberg spin limit, where $J_z$ equals to one. To observe this effect, a quantum spin $S$ = 1/2 triangular lattice should be realized experimentally. In spite of the great interest on the triangular HAF in theoretical papers [Ref.1.19-22], real compounds are insufficient to be studied. Among a few examples, $Cs_2CuBr_4$ shows a 1/3 plateau at the low temperature of $\frac{J}{k_B}T_N$ = 0.4 K, which excludes the possible plateau behavior induced by thermal fluctuations [Ref.1.22]. However, due to structural distortions, other interactions such as the Dzyaloshinsky-Moriya interaction also plays a significant role [Ref.1.23]. $Ba_3CoSb_2O_9$ is another candidate for the triangular HAF because the ground state of the $Co^{2+}$ ions, which have $S$ = 3/2, becomes a Kramers doublet, which can be described by the pseudospin-1/2 at low temperatures well below 250 K [Ref.1.23,24]. This system shows a new abnormal

feature where $M = \frac{1}{3}M_s$ as well as the $\frac{5}{1}M_s$ plateau.

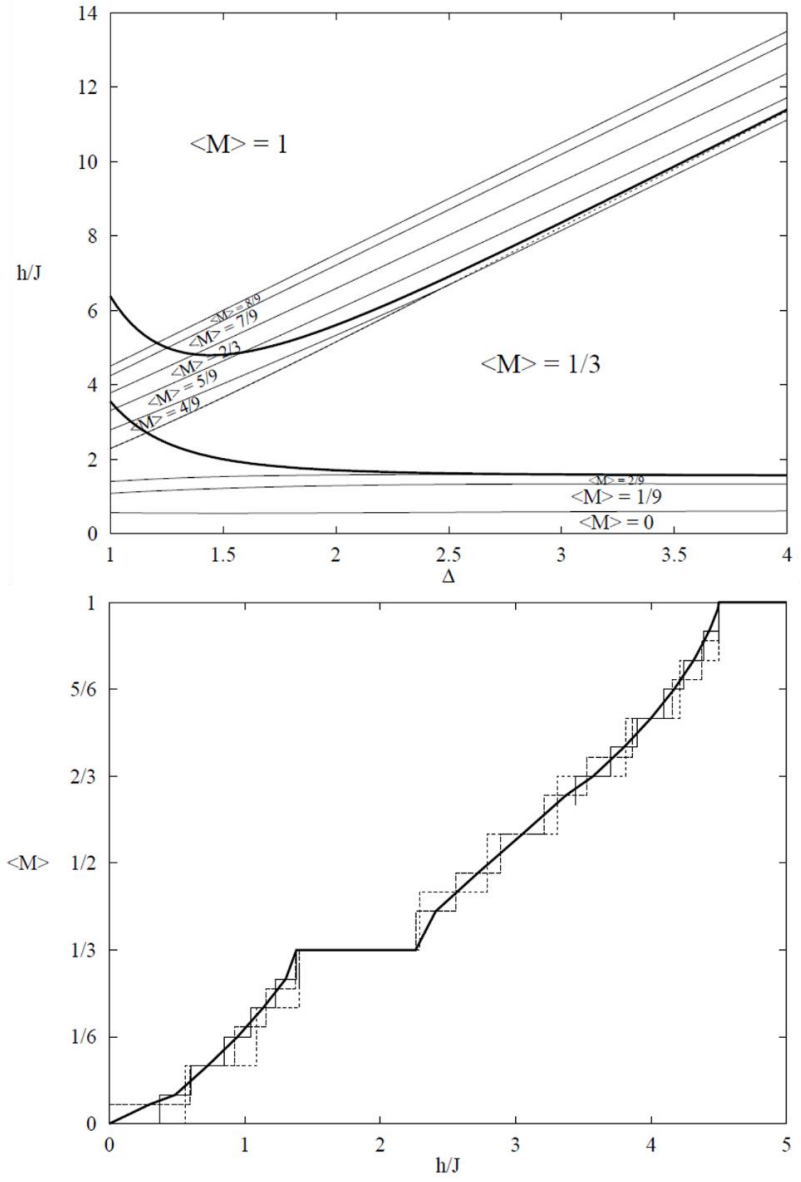


**FIG.1.4 (Upper) The magnetic phase diagram of a triangular XXZ antiferromagnet on a 3ئ6 lattice in [Ref.1.21]. The thin solid phase boundaries are calculated through finite-system diagonalizations and the solid ones are done via expansions around the Ising limit.**

**(Lower) Magnetization curves of the *S* = 1/2 triangular lattice HAF with ɑp= 1 on 3ئ6 (short dashes) in [Ref.1.21].**

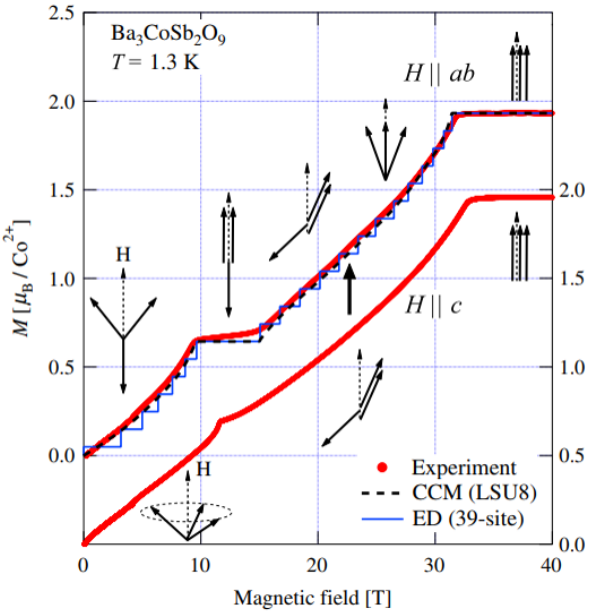


**FIG.1.5 The magnetization data for $Ba_3CoSb_2O_9$, which shows magnetic plateau where *M* = $\frac{0}{V}$*M*s [Ref.1.23]. The spin structure is depicted depending on the magnetic field.**

## 1.2 Outline of thesis

As the examples overviewed in the previous sections, the quantum spin systems are interesting playgrounds to study novel phenomena driven by strong quantum spin fluctuations. Following this concept, I studied quantum spin systems based on cuprate systems. Cuprate systems, especially when the copper ion has oxidation of 2+, have quantum spin-*S* = 1/2 because in many real lattices, the orbital angular momentum is

usually quenched due to the strong Jahn-Teller distortion. With the strong fluctuations from the quantum spin, however cuprate systems can show exotic behavior due to the large electron correlation $U$ leading a Mott insulator [Ref.1.25]. For example, high-$T_C$ superconductivity emerges by doping a charge-transfer insulator such as a 2D square antiferromagnetic lattices $La_2CuO_4$ [Ref.1.25,26]; the quantum spin liquid states are observed in 2D triangular HAFs ə-$(BEDT\text{-}TTF)_2Cu_2(CN)_3$ and $EtMe_3Sb[Pd(dmit)_2]_2$, and a 2D kagome HAF herbertsmithite [Ref.1.9-11]; and the observation of the separation of the electron into independent quasiparticles that carry spin (spions), charge (holons), and orbital degree of freedom (orbitons) was reported in Mott insulator $SrCuO_2$ and $Sr_2CuO_3$ [Ref.1.27,28]. To find intriguing phenomena emerging from strong quantum fluctuations, I studied two novel cuprate systems $CuAl_2O_4$ and $CuR_2Ge_2O_8$ ($R$ = Y, La).

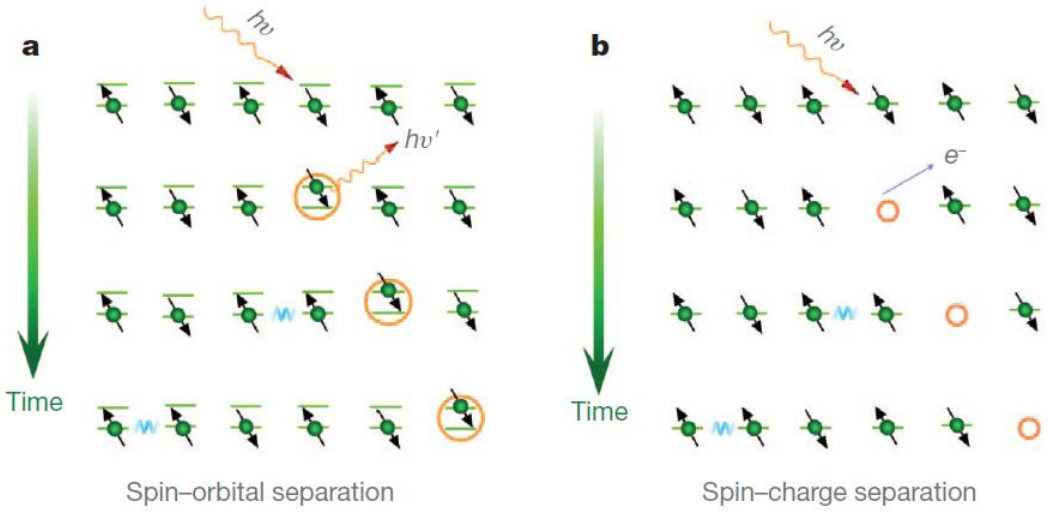


**FIG.1.6 The process of spin-orbital separation in a spin chain $Sr_2CuO_3$ [Ref.1.28]. (a) Sketches of spin-orbital separation and (b) spin-charge separation generated in processes of resonant inelastic x-ray scattering (RIXS).**

In the next chapter, the experimental techniques for studying $CuAl_2O_4$ and $Cu\mathit{R}_2Ge_2O_8$ are introduced. The detailed methods to grow single- and polycrystalline samples are explained in Chapter 2. The structural information for the samples is also provided by identifying the crystal structures though x-ray diffraction techniques and Rietveld refinement. In Chapter 3, I study the emergence of a spin-orbital entangled pseudo spin state $J_{\text{eff}} = 1/2$ in $CuAl_2O_4$. This system has the exotic ground state which is different from spin-$S = 1/2$ of conventional cuprates but has nonzero effective orbital angular momentum. The advent of the unusual ground state is directly proven by x-ray absorption spectroscopy techniques. With the strong quantum fluctuation of the $J_{\text{eff}} = 1/2$, this Mott insulator doesn't show any clue of long-range order but indicates characteristics of an extraordinary disordered state. I study a novel quasi 2D triangular HAF $Cu\mathit{R}_2Ge_2O_8$ ($R$ = Y, La) in the following Chapter 4. By the extensive studies on the lattice structure of $Cu\mathit{R}_2Ge_2O_8$, I verified that the magnetic lattice of the system is more close to a 2D triangular HAF rather than the one-dimensional chain expected in the previous research. The magnetic and thermodynamic measurements and the density functional theory (DFT) calculation of the system also support the nature of a charge-transfer 2D triangular HAF. This system also shows an exotic magnetic phase transition in $M(H)$ which may related to the interlay of the strong quantum fluctuations and the interlayer couplings induced by its buckled layer.

## References

[Ref.1.1] L. Balents, Nature **464**, 199 (2010).

[Ref.1.2] T. Yildirim, A. B. Harris, E. F. Shender, Phys. Rev. B **58**, 6 (1998).

[Ref.1.3] U. Schollwẹ ck, J. Richter, D. J. J. Farnell, R. F. Bishop (Eds.), *Quantum Magnetism* (Springer, Berlin, 2004).

[Ref.1.4] P. W. Anderson, Science **235**, 1196 (1987).

[Ref.1.5] M. R. Norman, Rev. Mod. Phys. **88**, 041002 (2016).

[Ref.1.6] P. W. Anderson, Mater. Res. Bull. **8**, 153 (1973).

[Ref.1.7] N. Read and S. Sachdev, Phys. Rev. Lett. **66**, 1773 (1991).

[Ref.1.8] I. Affleck and J. B. Marston, Phys. Rev. B **37**, 3774 (1988).

[Ref.1.9] Y. Shimizu, K. Miyagawa, K. Kanoda, M. Maesato, and G. Saito, Phys. Rev. Lett. **91**, 107001 (2003).

[Ref.1.10] T. Itou, A. Oyamada, S. Maegawa, M. Tamura, and R. Kato, Phys. Rev. B **77**, 104413 (2008).

[Ref.1.11] P. Mendels, F. Bert, M. A. de Vries, A. Olariu, A. Harrison, F. Duc, J. C. Trombe, J. S. Lord, A. Amato, and C. Baines, Phys. Rev. Lett. **98**, 077204 (2007).

[Ref.1.12] Tian-Heng Han, Joel S. Helton, Shaoyan Chu, Daniel G. Nocera, Jose A. Rodriguez-Rivera, Collin Broholm, and Young S. Lee, Nature **492**, 406 (2012).

[Ref.1.13] Yi Zhou, Kazushi Kanoda, and Tai-Kai Ng, Rev. Mod. Phys. **89**, 025003 (2017).

[Ref.1.14] A. Kitaev, Ann. Phys. **321**, 2 (2006)

[Ref.1.15] Y. Kasahara, T. Ohnishi, Y. Mizukami, O. Tanaka, Sixiao Ma, K. Sugii, N. Kurita,

H. Tanaka, J. Nasu, Y. Motome, T. Shibauchi, and Y. Matsuda, Nature **559**, 227 (2018).

[Ref.1.16] Simon Trebst, arXiv:1701.07056v1.

[Ref.1.17] S. Agrestini, C.-Y. Kuo, K.-T. Ko, Z. Hu, D. Kasinathan, H. B. Vasili, J. Herrero-Martin, S. M. Valvidares, E. Pellegrin, L.-Y. Jang, A. Henschel, M. Schmidt, A. Tanaka, and L. H. Tjeng, Phys. Rev. B **96**, 161107(R) (2017).

[Ref.1.18] K. W. Plumb, J. P. Clancy, L. J. Sandilands, V. Vijay Shankar, Y. F. Hu, K. S. Burch, Hae-Young Kee, and Young-June Kim, Phys. Rev. B **90**, 041112(R) (2014).

[Ref.1.19] A. V. Chubukov, S. Sachdev, and T Senthil, J. Phys.: Condens. Matter **6**, 8891 (1994).

[Ref.1.20] H. Nishimori and S. Miyashita, J. Phys. Soc. Jpn **55**, 4448 (1986).

[Ref.1.21] A. Honecker, J. Phys.: Condens. Matter **11**, 4697 (1999).

[Ref.1.22] T. Ono, H. Tanaka, H. Aruga Katori, F. Ishikawa, H. Mitamura, and T. Goto, Phys. Rev. B **67**, 104431 (2003).

[Ref.1.23] Takuya Susuki, Nobuyuki Kurita, Takuya Tanaka, Hiroyuki Nojiri, Akira Matsuo, Koichi Kindo, and Hidekazu Tanaka, Phys. Rev. Lett. **110**, 267201 (2013).

[Ref.1.24] Hiroyuki Shiba, Yoshifumi Ueda, Kouichi Okunishi, Shojiro Kimura, and Koichi Kindo, J. Phys. Soc. Jpn **72**, 2326 (2003).

[Ref.1.25] Manabu Takahashi and Jun-ichi Igarashi, Phys. Rev. B **59**, 7373 (1999).

[Ref.1.26] C. Weber, K. Haule, and G. Kotliar, Nat. Phys. **6**, 574 (2010).

[Ref.1.27] B. J. Kim, H. Koh, E. Rotenberg, S.-J. Oh, H. Eisaki, N. Motoyama, S. Uchida, T. Tohyama, S. Maekawa, Z.-X. Shen, and C. Kim, Nat. Phys. **2**, 397 (2006).

[Ref.1.28] J. Schlappa, K. Wohlfeld, K. J. Zhou, M. Mourigal, M. W. Haverkort, V. N.

Strocov, L. Hozoi, C. Monney, S. Nishimoto, S. Singh, A. Revcolevschi, J.-S. Caux, L. Patthey, H. M. Rßnnow, J. van den Brink, and T. Schmitt, Nature **485**, 82 (2012).

# Chapter 2
# Experimental Techniques

## 2.1 Sample synthesis

### 2.1.1 Flux method

To grow high quality cuprate single-crystals, a flux method was used. In this method, the ingredient raw materials are put into a crucible with low reactivity, such as a platinum crucible, together with a flux compound acting as a solvent. The mixture (the raw materials and the flux) is dissolved by heating and then cooled slowly to form a single-crystal. In this case, the raw material contains elements that form a single-crystal, and is a chemical compound that directly participates in the chemical reaction. The flux, however, does not participate in the chemical reaction but serves to lower the melting point of the mixture. The raw materials melted in the flux forms a liquid phase of a target compound through a chemical reaction. As the temperature is lowered, the target material becomes solid. At this time, a seed of the target material is formed; the seed gradually grows; and it becomes a crystal. In a crystal, it needs energy to stabilize domain walls. To release the energy, as a crystal grows, the domains merge into a large single-domain reducing the number of

domain walls. Eventually the crystal becomes a single-crystal.

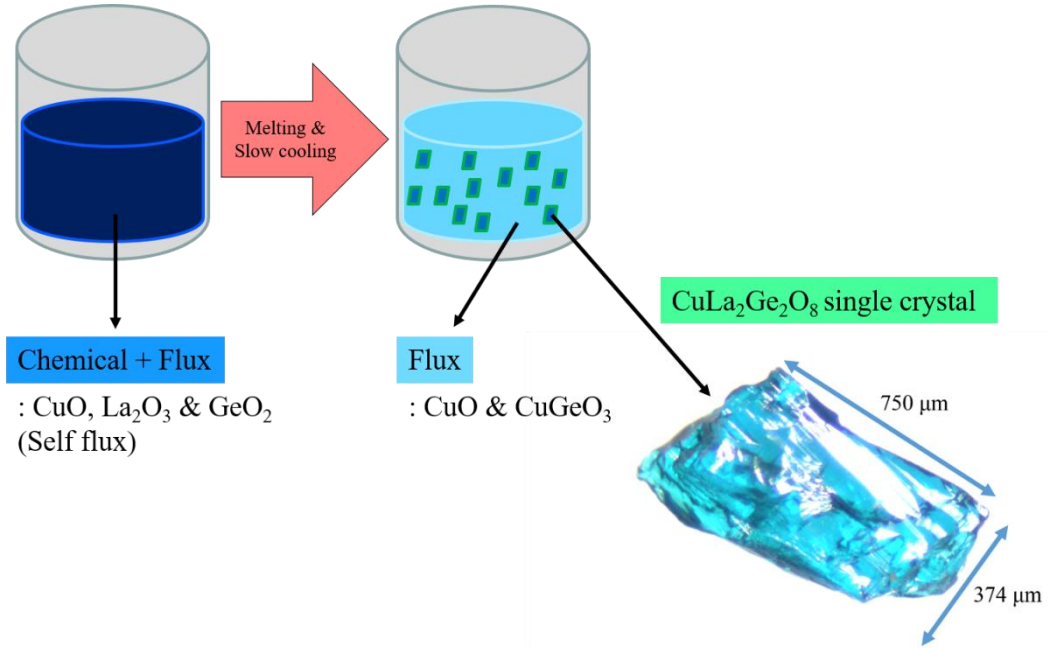


**FIG.2.1 $CuLa_2Ge_2O_8$ single-crystal growth using flux method.**

**$CuLa_2Ge_2O_8$ single-crystal growth**

A target compound of $CuLa_2Ge_2O_8$ was synthesized in single-crystal form via a flux method. To synthesize the single-crystal, CuO and $GeO_2$ powder were used as self-flux so that the ratio of the initial materials was CuO : $La_2O_3$ : $GeO_2$=8:1:6 [Ref.2.1]. The mixture was annealed for 30 minutes at 1260 in a platinum crucible and then slowly cooled down to 1000 at a rate of 2 /hour. Diluted HCl (~17 %) solution was used to remove any residual flux and byproducts like CuO and $CuGeO_3$ from the grown crystals. The typical size of a $CuLa_2Ge_2O_8$ single-crystals is about 0.001 $mm^3$ and a photo of one of the biggest crystals is shown in the FIG.2.1. The color of the crystals is transparent blue and they have

an albite shape. A passing note, despite several attempts with the same flux method it was failed to grow single crystals of $CuY_2Ge_2O_8$, which may well be due to the difference in the ionic size between Y and La.

**$CuAl_2O_4$ single-crystal growth**

According to the phase diagram of CuO-$Al_2O_3$ [Ref.2.2], after CuO and $Al_2O_3$ are mixed at a ratio of 1:1 and then melted at a high temperature under ambient atmosphere (the oxygen partial pressure $p_{o2}$ = 0.2 atm) they are first cooled to an solid $Al_2O_3$ + $CuAlO_2$ phase at about 1260 . It subsequently changes to $CuAl_2O_4$ + $CuAlO_2$ phase at about 1170 . In this case, it is difficult to obtain large $CuAl_2O_4$ crystals because the raw materials react to $CuAlO_2$ firstly at 1260 . However, when the oxygen partial pressure is increased to $p_{o2}$ = 0.4 atm, the area of the $Al_2O_3$ + $CuAlO_2$ phase decreases. This seems to be related to stabilizing $Cu^{2+}$ in $CuAl_2O_4$ by further oxidizing $Cu^{+}$ in $CuAlO_2$. Therefore, it was thought that to reduce the amount of $CuAlO_2$ and increase the amount of $CuAl_2O_4$ phase, the oxygen partial pressure would be increased to 1 by flowing oxygen gas in a closed tube furnace. Initial raw materials of polycrystalline CuO and $Al_2O_3$ were mixed in 1:1 molar ratio with sufficient amount of a flux, anhydrous sodium tetraborate [Ref.2.3]. The mixture in a platinum crucible was annealed using a ceramic tube furnace flowing $O_2$ gas. After heated up to 1350 , it dwelled at 1350 for 24 hours and then slowly cooled down to 750 . After removing the flux by applying diluted HCl (~17 %), I got dark brown single-crystals of $CuAl_2O_4$ (inset in FIG.2.5). The crystal size is up to 1 $mm^3$ with typical octahedral shape of spinel type crystals.

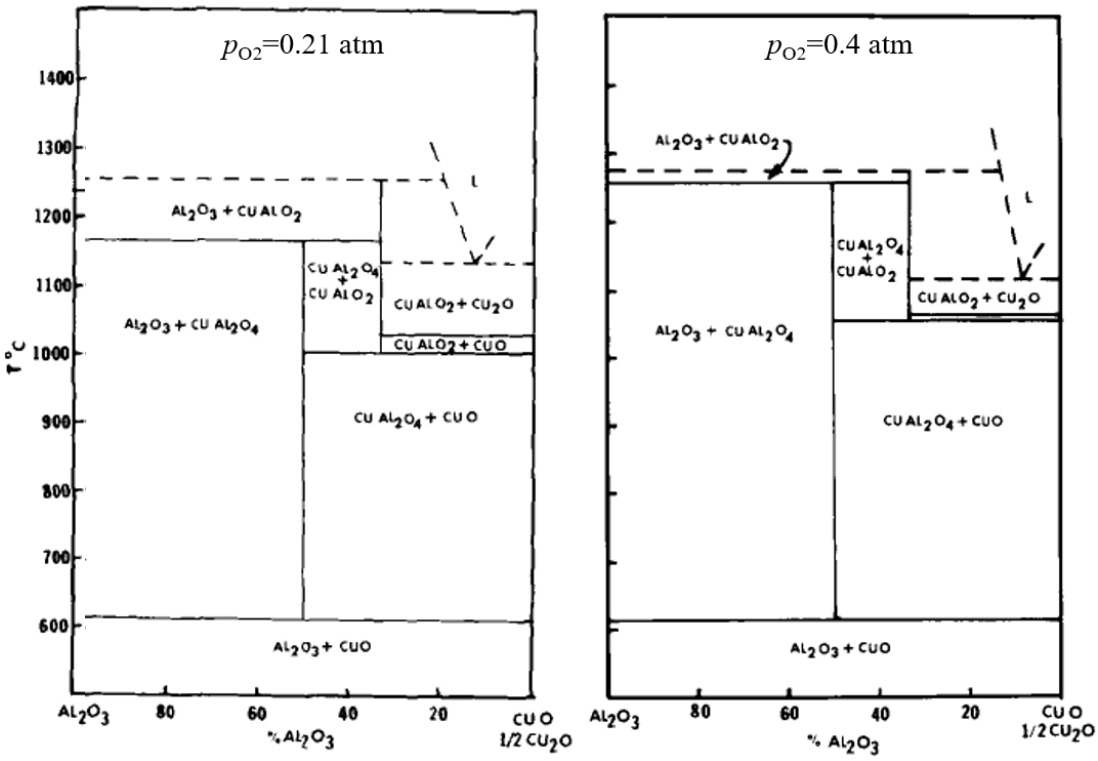


**FIG.2.2 Phase diagram of CuO-$Al_2O_3$ with different oxygen partial pressures: (left) $p_{o2}$ = 0.21 and (right) $p_{o2}$ = 0.4 atm [Ref.2.2].**

## 2.1.2 Solid state reaction method

The solid state reaction method is the most common method to grow polycrystalline samples with crystal size of 1~10 εm. First, the ingredient materials are ground and mixed in a mortar in the stoichiometric ratio of the target compound. The ratio can be changed more or less in case that the raw materials are volatile. The mixture should be pelletized using a pressure die and pressurizing system. The pelletizing process will reduce the

distance between the raw materials, which enhances the reactivity and reduces evaporation of the raw materials. The pellet should be contained in unreactive crucibles such as alumina or platinum crucibles. The type of the crucibles has to be selected by checking the reactivity with the raw materials. Finally, the pellet is heated for a few days at the temperature where the phase of the target material forms. After cooling, the pellet is ground in powder or cracked in small pieces to check the phase of the sample via characterizing techniques such as powder x-ray diffraction (XRD) or energy-dispersive x-ray spectroscopy (EDS or EDX). Until the sample has pure mono-phase of the target material, one should repeat the sequences.

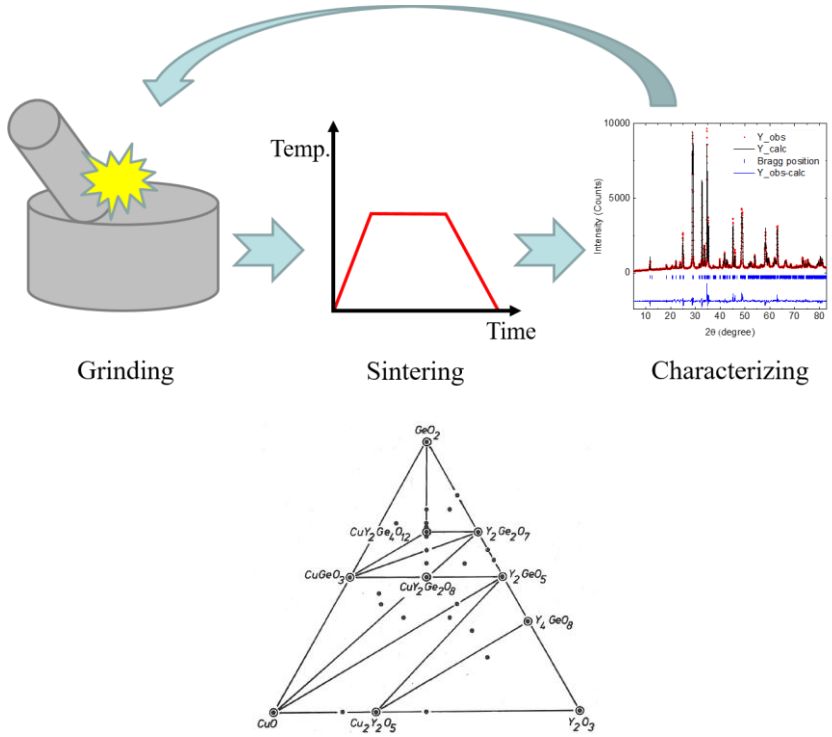


**FIG.2.3 Schematic diagram for solid state reaction method and the phase diagram of CuO-$Y_2O_3$-$GeO_2$ [Ref.2.4].**

I prepared high-quality polycrystalline samples of $CuY_2Ge_2O_8$ and $CuLa_2Ge_2O_8$ by sintering the mixture of CuO, $R_2O_3$ (R=Y and La), and $GeO_2$ in a stoichiometric ratio, 1:1:2 at 850 for 12 hours [Ref.2.4]. The mixture was ground before a final sintering under the same conditions. The finally sintered powder of $CuY_2Ge_2O_8$ ($CuLa_2Ge_2O_8$) was then pelletized and annealed by increasing temperature from 950 to 1100 (1050 ) at 50 steps with a duration of 24 hours at each step: I optimized the final sintering temperature to produce highest-quality samples based on our x-ray diffraction (XRD) data.

## 2.2 Crystal structure analysis

### 2.2.1 X-ray diffraction

**Single-crystal XRD**

This technique is a powerful method to identify the crystal structure of a small single-crystal. After the crystal is mounted on the sample stage, it is exposed to x-ray beam emitted from the collimator. The scattered x-ray from atoms interferes with each other following the Braggôs law and it makes strong signals on the detector. By analyzing the positions and intensities of the peaks, the crystal structure of the sample can be verified. There are strong points in this technique comparing with powder diffraction technique. First, the number of Bragg peaks obtained via single-crystal XRD is much larger than that of powder diffraction. It is possible to collect a few thousands of Bragg peaks by single-crystal XRD but for powder diffraction, random orientation of polycrystalline sample makes a number of

concentric circle signals (usually less than a hundred) on the detector and weak reflection is buried in a background. Therefore, the amount of information is much abundant in the case of single-crystal XRD, which can be used to distinguish small difference among similar crystal structures. To reduce x-ray absorption by the sample, the size of the crystal is standardized to be 100-500 ε m.

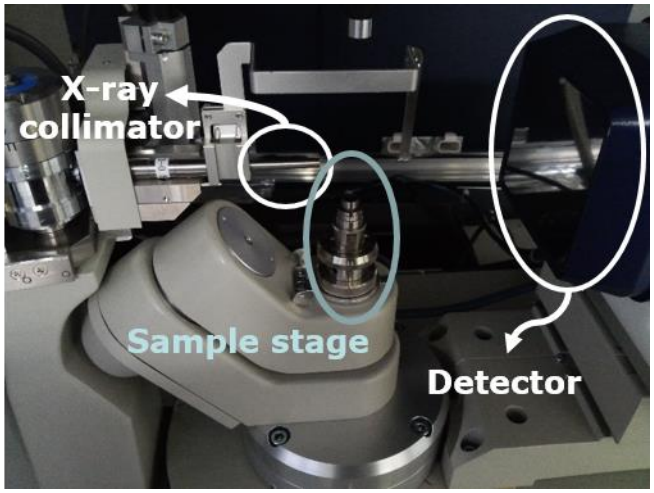


**FIG.2.4 Picture of a high resolution single-crystal X-ray diffractometer (XtaLAB P200, Rigaku) used to verify single-crystal samples.**

In order to identify the crystal structure of single-crystals, the crystals were measured using a high resolution single-crystal X-ray diffractometer (XtaLAB P200, Rigaku) with Mo source (∂ĸŭ=0.710747 ¡ ) at room temperature. For the full structural refinement of $CuLa_2Ge_2O_8$, a small and high-quality single crystal with dimensions of 95Ĭ 70Ĭ 50 ε $m^3$ was used to minimize x-ray absorption effects. Using the high-resolution single-crystal x-ray diffractometer, 3383 Bragg peaks (2369 independent Bragg peaks) were collected. In

the case of identifying the crystal structure of $CuAl_2O_4$ single-crystal, a small crystal with volume of ~0.03 $mm^3$ was measured. The number of total independent Bragg peaks was 148.

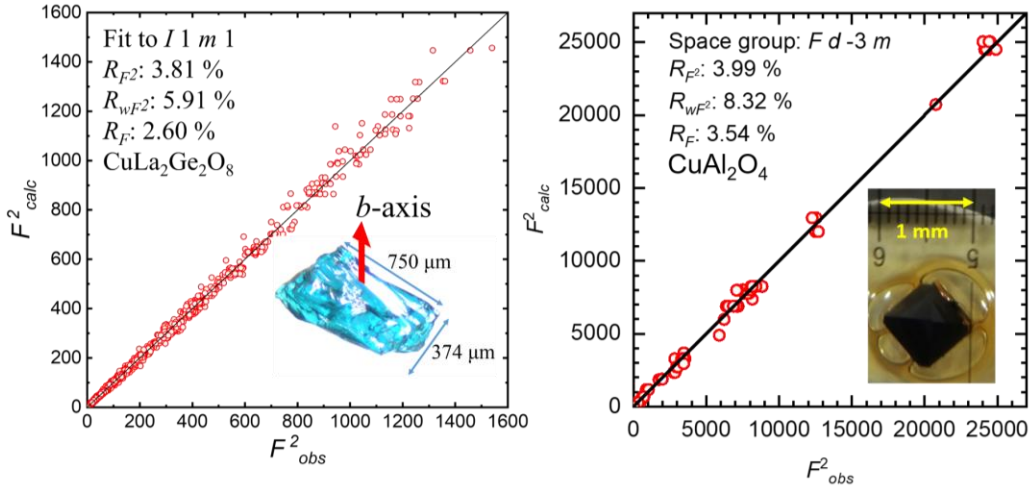


**FIG.2.5 The refinement results of the single-crystal XRD data of (left) $CuLa_2Ge_2O_8$ and a picture of single-crystal sample taken using an optical microscope (inset), and (right) $CuAl_2O_4$ and a picture of a $CuAl_2O_4$ single-crystal (inset).**

**Powder diffraction techniques**

Powder diffraction technique is a more convenient method as compared with singe-crystal XRD. Usually, it is harder to grow a single-crystal than a polycrystalline sample. Thus it is easier to mount the polycrystalline sample on a sample holder because it is not necessary to check the orientation of the sample. I used two different powder diffraction techniques depending on the source of the beam: x-ray and neutron. X-ray source is easier to be accessed in an university laboratory but to acquire neutron source, a neutron beamline facility is required. Despite of the low accessibility, neutron beam is highly demanded to

identify the position of light elements such as oxygen. To check the quality of the polycrystalline samples, two different powder diffraction instruments were used: Miniflex II, Rigaku powder XRD with a wavelength of 1.540590 and 1.544310 ¡ (K$\check{u}_1$ and K$\check{u}_2$, respectively) and a high-resolution neutron diffractometer in beamline Echidna, ANSTO with a wavelength of 2.4378 ¡ .

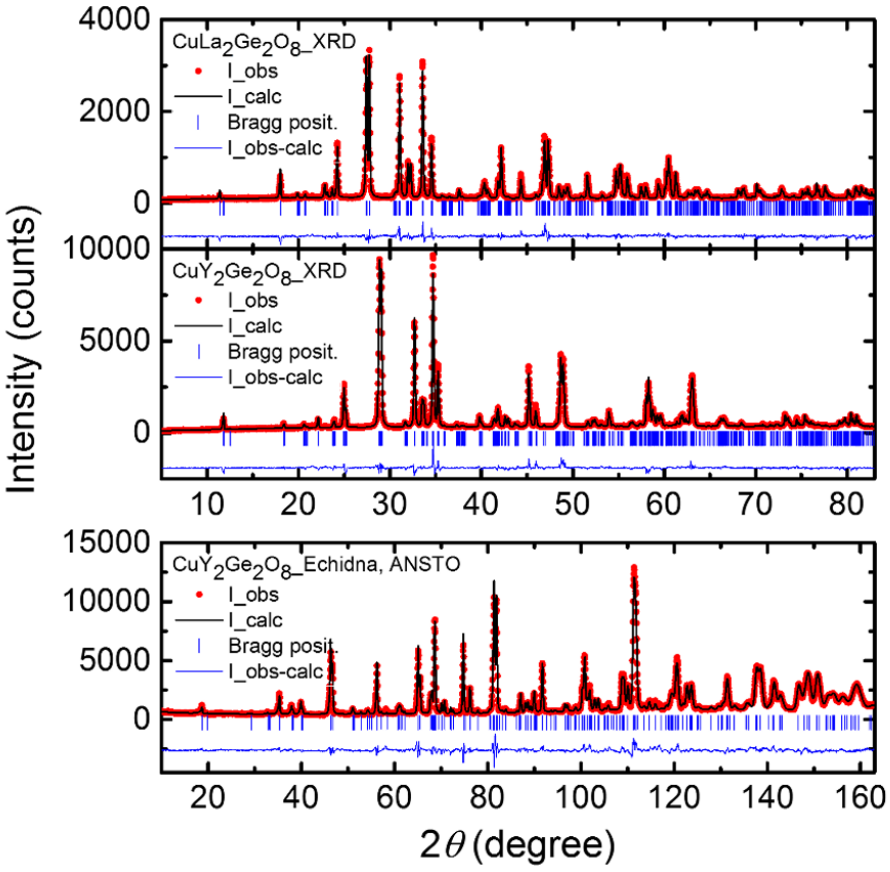


**FIG.2.6 The refinement results of the x-ray powder diffraction of Cu$R_2Ge_2O_8$ ($R$=Y and La) and neutron powder diffraction data of $CuY_2Ge_2O_8$ measured on the Echidna beamline, ANSTO.**

## 2.2.2 Rietveld refinement

**Cu$R_2Ge_2O_8$ ($R$ = Y and La)**

For the analysis of the measured diffraction patterns, the ‘FullProf’ software suite was used [Ref.2.5]. The crystal structure of $CuLa_2Ge_2O_8$ was refined using both the powder XRD and the single-crystal XRD. Usually, lab XRD is known to be an insufficient tool for identifying the oxygen positions. However, with the aid of a number of Bragg peaks from the single-crystal diffractometer, it was possible to verify the crystal structure including the oxygen positions of the system. In case of the single-crystal XRD, the observed intensity, $F^2_{obs}$ and the calculated intensity, or square of structural factor, $F^2_{calc}$ of each Bragg peaks are well matched with each other (FIG.2.5), which is also supported by the small agreement factors: $R_{F2}$, $R_{wF2}$, and $R_F$ in TABLE 2.1. In case of the powder XRD, the simulated profiles of the refined structure have good correspondence with the observed patterns (FIG.2.6). Other structural information obtained by Rietveld refinement such as the fractional atomic positions, thermal parameters, and occupancies are summarized in TABLE 2.1.

To refine the crystal structure of $CuY_2Ge_2O_8$, powder XRD and neutron powder diffraction (NPD) patterns were used. NPD patterns especially provide the information of the oxygen positions, which is hard to estimate from the powder XRD patterns. The simulated profiles of the refined structure also have good correspondence with the observed patterns. From the structural refinement, it turned out that $CuLa_2Ge_2O_8$ and $CuY_2Ge_2O_8$ are isostructural.

**TABLE 2.1 The summary of the crystal structure of $CuLa_2Ge_2O_8$ as obtained from the single-crystal XRD refinement data shown in FIG.2.5.**

| Space group: *I* 1 *m* 1 (No. 8)<br>Cell dimensions: *a* (¡ ) = 8.587(2), *b* (¡ ) = 15.565(6), *c* (¡ ) = 5.199(1), *ß* (Ű = 89.30(1),<br>*V* (¡ $^3$) = 694.9(3), Sample size (ε m$^3$): 95Ĭ 70Ĭ 50 | | | | | | |
|---|---|---|---|---|---|---|
| Atom | Wyckoff letter | Site symmetry | *x/a* | *y/b* | *z/c* | $U_{iso}$ (¡ $^2$) |
| La1 | *b* | 1 | 0.752(1) | 0.12117(2) | 0.526(2) | 0.0094(1) |
| La2 | *b* | 1 | 0.251(1) | 0.12038(2) | 0.526(2) | 0.0087(1) |
| Ge1 | *a* | *m* | 0.003(1) | 0.5000 | 0.573(2) | 0.0056(9) |
| Ge2 | *a* | *m* | 0.498(1) | 0.5000 | 0.479(2) | 0.006(1) |
| Ge3 | *b* | 1 | 0.023(1) | 0.29161(7) | 0.525(2) | 0.0163(7) |
| Cu | *b* | 1 | 0.478(1) | 0.29192(7) | 0.527(2) | 0.0051(7) |
| O1 | *a* | *m* | 0.8401(6) | 0.5000 | 0.778(1) | 0.0104(2) |
| O2 | *a* | *m* | 0.1685(6) | 0.0000 | 0.783(1) | 0.0104(2) |
| O3 | *a* | *m* | 0.841(2) | 0.0000 | 0.774(3) | 0.0104(2) |
| O4 | *a* | *m* | 0.165(2) | 0.5000 | 0.781(3) | 0.0104(2) |
| O5 | *b* | 1 | 0.508(1) | 0.0927(5) | 0.873(2) | 0.0104(2) |
| O6 | *b* | 1 | 0.992(1) | 0.3245(4) | 0.875(2) | 0.0104(2) |
| O7 | *b* | 1 | 0.499(1) | 0.4069(5) | 0.680(2) | 0.0104(2) |
| O8 | *b* | 1 | 0.999(1) | 0.1745(4) | 0.705(2) | 0.0104(2) |
| O9 | *b* | 1 | 0.360(1) | 0.2409(3) | 0.809(2) | 0.0104(2) |
| O10 | *b* | 1 | 0.695(1) | 0.2296(3) | 0.851(2) | 0.0104(2) |
| Atom | $U_{11}$ (¡ $^2$) | $U_{22}$ (¡ $^2$) | $U_{33}$ (¡ $^2$) | $U_{12}$ (¡ $^2$) | $U_{13}$ (¡ $^2$) | $U_{23}$ (¡ $^2$) |
| La1 | 0.0141(1) | 0.0049(1) | 0.0092(1) | 0.0031(4) | -0.00463(9) | 0.0013(4) |
| La2 | 0.0102(1) | 0.0049(1) | 0.0110(1) | 0.0012(4) | 0.00561(9) | -0.0000(4) |
| Ge1 | 0.0078(9) | 0.0059(7) | 0.003(1) | 0 | 0.0005(9) | 0 |
| Ge2 | 0.0062(9) | 0.0052(7) | 0.007(1) | 0 | 0.0010(9) | 0 |
| Ge3 | 0.0211(9) | 0.0130(6) | 0.0147(7) | 0.0029(7) | 0.0041(7) | -0.0011(7) |
| Cu | 0.0070(8) | 0.0015(5) | 0.0068(7) | 0.0010(6) | 0.0071(6) | -0.0011(6) |
| Agreement factors: $\sigma^2$ = 3.26, $R_{F2}$ (%) = 3.81, $R_{wF2}$ (%) = 5.91, $R_F$ (%) = 2.60 | | | | | | |

**$CuAl_2O_4$**

The observed intensity, $F^2_{obs}$ and the calculated intensity, or square of structural factor, $F^2_{calc}$ of each Bragg peaks also show good agreement with each other (FIG.2.5). This leads to sufficiently small (smaller than 10) agreement factors: $R_{F2}$, $R_{wF2}$, and $R_F$. The identified space group is *F d* -3 *m* (No. 227) and the lattice parameter is *a* = 8.083 ¡ . Other structural information obtained by Rietveld refinement such as the fractional atomic positions, thermal parameters, and occupancies are summarized in TABLE 2.2. From the refinement, I could not observe any clue for tetragonal distortion in the unit cell, which means there is no Jahn-Teller distortion even though $Cu^{2+}$ is Jahn-Teller active.

**TABLE 2.2 The crystal structure of $CuAl_2O_4$ as obtained from the Rietveld refinement data shown in FIG.2.5.**

| | Space group: *F d* -3 *m* (No. 227)<br>Cell dimensions: *a*(¡ ) = 8.083(5), *V*(¡ $^3$) = 528.1(5) | | | | | | |
|---|---|---|---|---|---|---|---|
| Atom | Wychoff letter | Site symmetry | *x*/*a* | *y*/*b* | *z*/*c* | $U_{iso}$ (¡ $^2$) | Occupancy |
| Cu1 | *a* | -4 3 *m* | 0 | 0 | 0 | 0.613(52) | 0.029 |
| Al1 | *a* | -4 3 *m* | 0 | 0 | 0 | 0.613(52) | 0.012 |
| Al2 | *d* | -3 *m* | 0.625 | 0.625 | 0.625 | 0.267(54) | 0.071 |
| Cu2 | *d* | -3 *m* | 0.625 | 0.625 | 0.625 | 0.267(54) | 0.012 |
| O | *e* | 3 *m* | 0.3860(2) | 0.3860(2) | 0.3860(2) | 0.913(64) | 0.167 |
| Agreement factors: $R_{F2}$(%) = 3.99, $R_{wF2}$(%) = 8.32, $R_F$(%) = 3.54 | | | | | | | |

## References

[Ref.2.1] J. Campá, E. Gutiérrez-Puebla, M. Monge, C. Valero, J. Mira, J. Rivas, C. Cascales, and I. Rasines, J. Solid State Chem. **120**, 254 (1995).

[Ref.2.2] K. T. JACOB and C. B. ALCOCK, J. Am. Ceram. Soc. **58**, 192 (1975).

[Ref.2.3] Rosa Anna Fregola, Ferdinando Bosi, Henrik Skogby, Ulf H¬lenius, Am. Mineral. **97**, 1821 (2012).

[Ref.2.4] U. Lambert and W. Eysel, Powder Diffraction **1**, 45 (1986).

[Ref.2.5] J. Rodriguez-Carvajal, Physica B **192**, 55 (1993).

# Chapter 3
# Emergence of Spin-Orbital Entangled $J_{eff}$ = 1/2 State in $CuAl_2O_4$

## 3.1 Spin-orbital entangled Kramers doublet $J_{eff}$ = 1/2

### 3.1.1 Nature of $J_{eff}$ = 1/2

A $J_{eff}$ = 1/2 state was found by B. J. Kim in 2008 while studying the origin of insulating properties of $Sr_2IrO_4$ [Ref.3.1]. In this system, the $Ir^{4+}$ ion ($5d^5$) is on the site where six neighboring oxygen atoms form an octahedral crystal electric field (CEF), which induces five electrons (or one hole) in the $t_{2g}$ level. Since the Fermi level is on the wide $t_{2g}$ band, this system should be the band-metal but its actual electronic transport properties are insulating. This phenomenon originates from an interplay of spin-orbital coupling (SOC) and correlation between electrons. For the five electrons in the $t_{2g}$ level, it has total spin ($S$) of 1/2 and total effective angular momentum ($L_{eff}$) of 1. Strong SOC splits the $t_{2g}$ state to $j_{eff} = s + l_{eff}$ states (from now on, the capital letter means total angular momentum of electrons ٱ ث ث ة سي B ٱ ث ث ة and the small letter means angular momentum of one electron or hole). Kramers doublet $j_{eff}$ = 1/2 state, having higher energy, is occupied by one electron

while a quadruple $j_{eff}$ = 3/2 state with lower energy is fully occupied. This is a reversed situation comparing with splitting of atomic level with $s$ = 1/2 and $l$ = 1, which has higher $j$ = 3/2 and lower $j$ = 1/2 state. Therefore, there is a relation of $l_{eff}$ = -$l$. Due to the splitting of the $t_{2g}$ state by SOC, $T_{2g}$ band splits to $J_{eff}$ = 1/2 band and $J_{eff}$ = 3/2 band. Finally, due to the electronic correlation, the $J_{eff}$ = 1/2 state is separated to upper Hubbard band and lower Hubbard band and the ground state becomes a Mott insulator. The explicit form of the spin-orbital entangled Kramers doublet $j_{eff}$ = 1/2 is following:

$$|j_{eff} = 1/2, m_{j_{eff}} = \tilde{N}1/2\acute{0} = \frac{\circ}{\sqrt{1}}(|xy, \quad \mathring{u}\acute{0} \qquad |yz, \tilde{N}\mathring{u}\acute{0} + i|zx, \tilde{N}\mathring{u}\acute{0}),$$

where $xy$, $yz$, $zx$ are the orbital wave functions and $\tilde{N}\mathring{u}$ is the spinor. This ground state consists of the equal amount of $xy$, $yz$, $zx$ orbitals and it is not possible to separate the spin part from the orbital part. This spin-orbital entangled ground state, therefore, does not have orbital order and static Jahn-Teller (J-T) distortion.

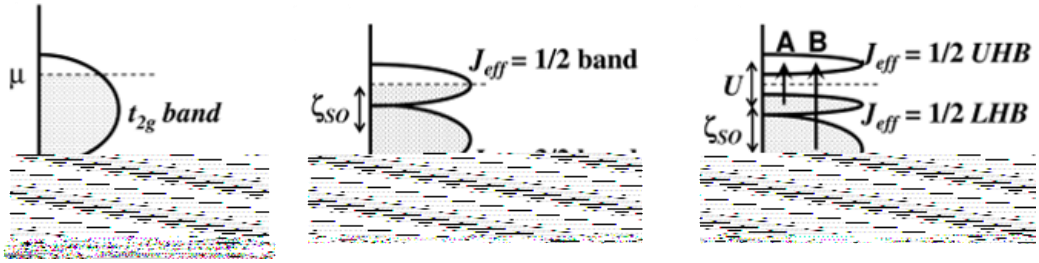


**FIG.3.1 Formation of $J_{eff}$ = 1/2 state in $Sr_2IrO_4$ from [Ref.3.1].**

## 3.1.2 Noble phenomena in $J_{eff}$ = 1/2 compounds

Plenty of intriguing emergent phenomena have been predicted or reported from the

angular moment is usually quenched ($L \neq 0$) and it is difficult to observe the role of SOC.

However, we expect $J_{eff}$ = 1/2 state to be created in 3*d* if the following condition is satisfied. First, there should be five electrons (or one hole) in $t_{2g}$ state. To make the $t_{2g}$ occupied with five electrons, there are two possibilities: $3d^5$ in octahedral CEF and $3d^9$ in tetrahedral CEF. For 3*d* compounds, the electrons prefer a high spin configuration, and therefore, $3d^9$ $Cu^{2+}$ ion in tetrahedral CEF is more probable to induce $j_{eff}$ = 1/2. The second condition is that the $t_2$ state (since tetrahedral CEF does not have an inversion center, from now on, the $t_2$ state will be used instead of the $t_{2g}$) should be degenerate. There should be no structural distortion, which breaks the local symmetry of the cubic tetrahedral CEF ($T_d$) such as J-T distortion. Or, the effective angular momentum will be quenched. Finally, the electronic transport properties show insulating behavior due to the role of electronic correlation.

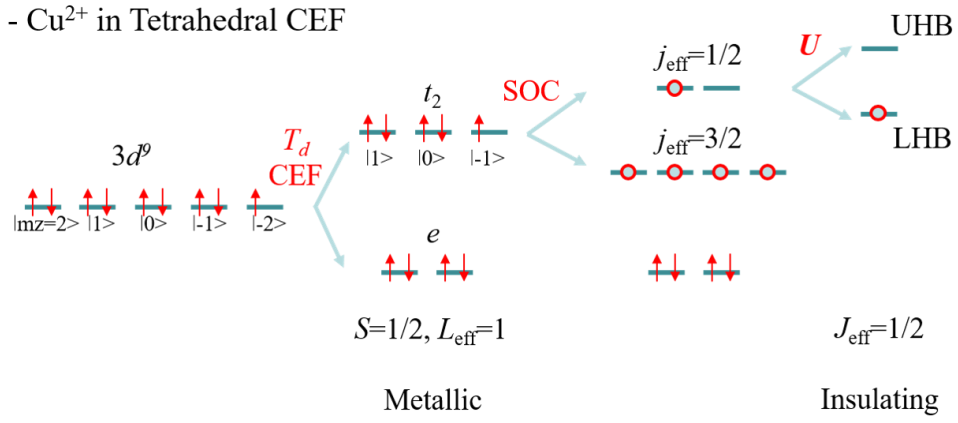


**FIG.3.3 $Cu^{2+}$ ion in tetrahedral CEF induces Mott insulating $J_{eff}$ = 1/2 ground state.**

## 3.2.2 Candidate material: $CuAl_2O_4$

Using single-crystal XRD, the crystal structure of $CuAl_2O_4$ was verified. The identified space group is *F d* -3 *m* (No. 227) and the lattice parameter is *a* = 8.083 ¡ [Ref.3.11]. This structure forms a cubic spinel-type structure $AB_2O_4$. The $Cu^{2+}$ ion on the A-site makes a tetrahedron with four neighboring oxygen ions and the $Al^{3+}$ ion on the B-site. The $CuO_4$ tetrahedral units form a diamond structure and these units are well separated from each other.

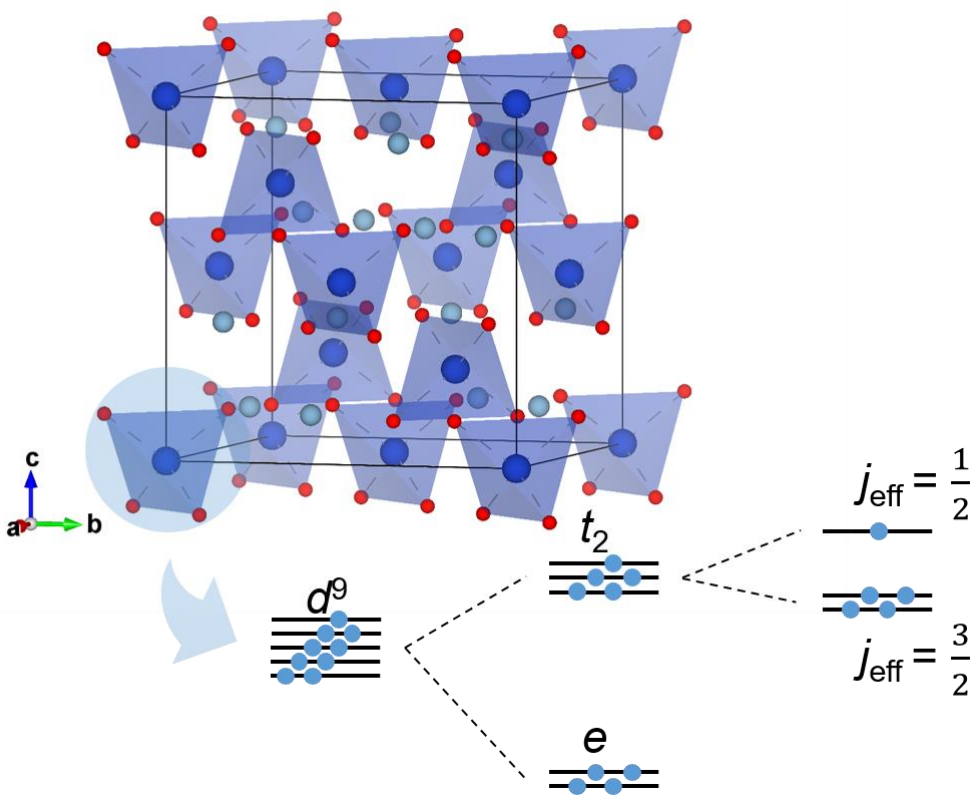


**FIG.3.4 Crystal structure of $CuAl_2O_4$. The blue, grey, and red spheres represent Cu, Al, and O atoms, respectively. The $CuO_4$ tetrahedra form a diamond lattice.**

This localized structure of tetrahedral units is expected to induce a narrow band width of the $Cu^{2+}$ $t_2$ band. From the Rietveld refinement result, we could not observe any clue for tetragonal distortion in the unit cell, which means there is no J-T distortion even though $Cu^{2+}$ is an J-T active ion. This cubic structure coincides with the previous report on neutron powder diffraction down to 0.4 K, which shows no J-T distortion and no magnetic long-range ordering [Ref.3.11].

To identify the local environment of $Cu^{2+}$, in addition, Cu K-edge x-ray absorption near edge structure (XANES) analysis was done by utilizing a synchrotron beamline (3A) in the Pohang Accelerator Laboratory in Korea [Ref.3.12]. The spectrum was obtained via fluorescence yield mode.

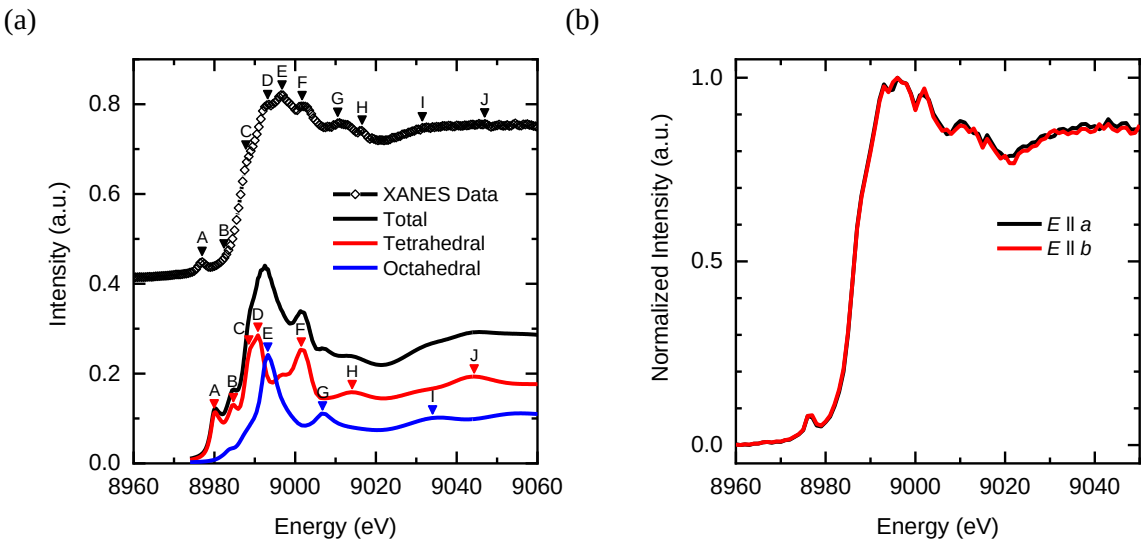


**FIG.3.5 (a) Copper K-edge and a simulation using FEFF8 software. (b) Comparison of spectra for two different polarizations.**

The experimental spectrum (the diamond symbol in FIG.3.5 (a)) has 10 peaks and we assign each peak as A-J. This spectrum can be reproduced by a simulation using FEFF8 software [Ref.3.13] with the crystal structure obtained from the Rietveld refinement result of the single crystal XRD measurement. The red line shows the spectrum from the tetrahedral contribution and the blue one shows that from the octahedral contribution, and the total spectrum (black line) is obtained by superposing the tetrahedral and octahedral contributions in 64:36 ratio following the site-inversion parameter of the $CuAl_2O_4$ system. The overall spectrum shape of the simulation consisting of 10 peaks is similar to the experimental one, which indicates the system has the cubic lattice of the refined structure. The pre-edge peak A in Cu K-edge absorption spectroscopy originates from copper 3*d*-4*p* hybridization of the tetrahedral site without centrosymmetry. Although the unit cell is cubic, to confirm the polarization dependency of the spectrum, we assigned one crystallographic axis as the *a*-axis and another perpendicular direction as the *b*-axis. FIG.3.5 (b) shows the spectra of two different polarizations, which are almost the same with each other. This isotropic polarization dependency of the spectrum also coincides with the cubic symmetry of the system.

The experimental peaks look suppressed as compared with those of the simulation. This is due to the over-absorption effect happening when a single crystal is measured in a fluorescence yield mode. Moreover, since the simulation is based on the Hartree-Fock calculation with the muffin-tin potential, electron correlation is hard to estimate exactly. Due to this limitation, there is a difference in the position of *d*-band.

The electronic transport properties were identified using our home-built transport system

(Keithley, Lake Shore, etc.), flowing the current along the (001) direction of the single-crystal with an octahedral shape. From 225 to 385 K, the resistance of the sample keeps decreasing exponentially. This property of $CuAl_2O_4$ is the characteristic behavior of an insulator with the activation energy of $E_a$ = 0.56(1) eV. A linear fit of the Arrhenius plot was carried out as seen in FIG.3.6.

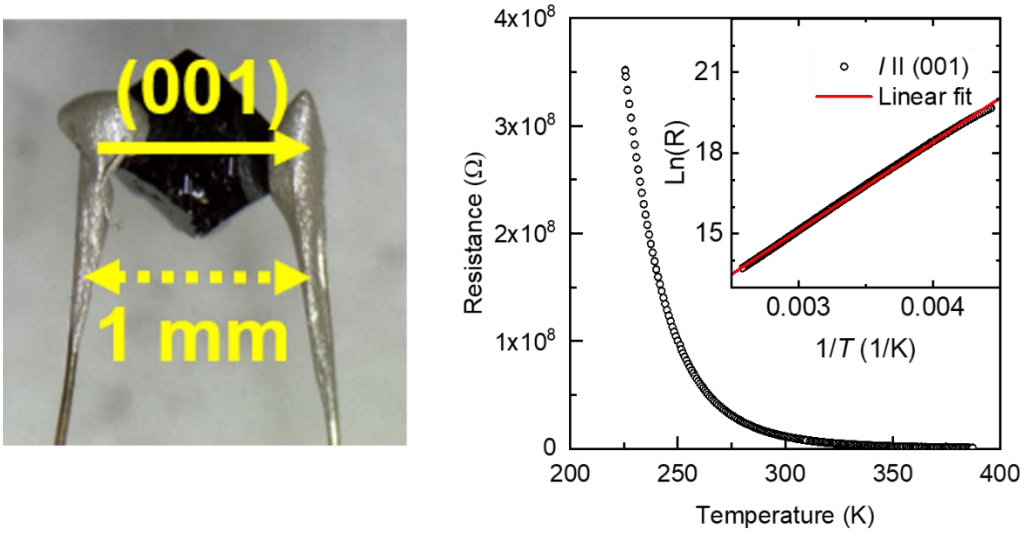


**FIG.3.6 (Left) A photo of a $CuAl_2O_4$ single crystal with two-wire contact. (Right) The resistance measurement data and (inset) the Arrhenius plot and its linear fit to estimate the activation energy.**

$CuAl_2O_4$ is the system following the criteria to induce the $J_{eff}$ = 1/2: $Cu^{2+}$ ion in tetrahedral CEF, no J-T distortion, and insulating. Moreover, many cuprate compounds are reported to be Mott insulators having large electronic correlation $U$ [Ref.3.10,14]. Therefore, $CuAl_2O_4$ is a good candidate to induce a $J_{eff}$ = 1/2 state with strong correlation.

## 3.3 XAS simulation for $CuAl_2O_4$

According to the electric dipolar selection rule, it can be determined the angular momentum quantum number of the unoccupied state which the core electron in 2*p* state will excite to. Since $j_{eff}$ = 1/2 state is branched out from atomic $j$ = 5/2, if the unoccupied state is $j_{eff}$ = 1/2, the $L_2$-edge transition ($2p^{1/2}$ to $j_{eff}$ = 1/2 transition) is forbidden but the $L_3$-edge transition ($2p^{3/2}$ to $j_{eff}$ = 1/2 transition) is allowed [Ref.3.5,15,16 and see Appendix]. The electric dipolar transition rate can be evaluated from the intensity of each transition peak in x-ray absorption spectroscopy (XAS).

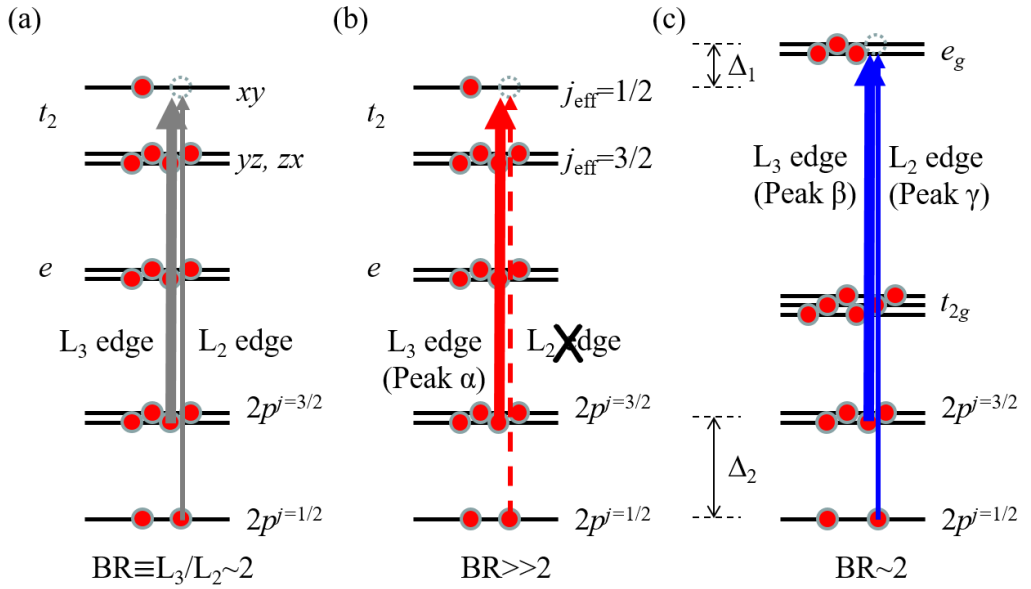


**FIG.3.7 XAS process of $Cu^{2+}$ in (a) tetrahedral A-site with *s* = 1/2 state, (b) tetrahedral A-site with $j_{eff}$ = 1/2 state, and (c) octahedral B-site with *s* = 1/2 state.**

For this reason the size of a branching ratio (BR), the intensity ratio between $L_3$-edge to $L_2$-edge, can be used to evaluate the emergence of $J_{eff}$ = 1/2: BR is close to 2 for conventional *d*-orbital states with quenched orbital angular momentum but BR is much larger than 2 for the $J_{eff}$ = 1/2 state.

In case of the actual $CuAl_2O_4$ single-crystal, ~35 % of site inversion is verified by single crystal XRD. Most of the $Cu^{2+}$ ions occupy the tetrahedral A-site and ~35 % of $Cu^{2+}$ ions sit on the octahedral B-site. If the ground state of the A-site ions is $J_{eff}$ = 1/2, there should be only one peak in $L_3$-edge due to the selection rule and absence of transitions to fully occupied *e* orbitals. The ground state of B-site ions, on the other hand, will be *S* = 1/2, which induces one peak in both $L_2$- and $L_3$-edge and BR should be close to 2. Therefore, the total spectrum looks there are two peaks in the $L_3$-edge originating from both A- and B-site ions and there is only one peak in $L_2$ï edge from B-site ions.

The L-edge of XAS is simulated by the charge transfer multiplet (CTM) calculations using the software óCTM4XASôversion 0.3 [Ref.3.17]. 10Dq of the octahedral site is $10Dq_{oct}$ = 1.8 eV which is reasonable comparing with other cuprates [Ref.3.18] and that of tetrahedral site is $10Dq_{tet} = \frac{۲}{۷}(10Dq_{oct})$ = 0.8 eV. The SOC constant of the copper 3*d* orbital is set to 51.2 meV following recent DFT calculations [Ref.3.12]. For simplicity of the simulation, we set the FWHM of $L_3$ and $L_2$ edges the same values. FIG.3.8 shows the result of the simulation. As we expected from the dipole transition selection rule, there is one peak Ŭat $L_3$ edge for the tetrahedral site copper ions (the red line in FIG.3.8), which supports the emergence of the $J_{eff}$ = 1/2 state.

For the octahedral site (the blue dashed line in FIG. 3.8), there are two peaks, ɓ and ɔ at

the $L_3$ and $L_2$ edge, respectively. Like conventional cuprate systems, having $S = 1/2$, the spectral weights of $L_3$ and $L_2$ should follow the branching ratio, $S_b/S_c$ of 2 and the position difference is æ2 ę 20 eV due to the SOC of the core 2*p* levels [Ref.3.19,20]. The total sum of the spectrum has one peak with a shoulder, which deviates æ1 ę 0.7 eV from the main peak at $L_3$ edge and one other peak without a shoulder at the $L_2$ edge. Since there is site-inversion of ~35 % verified by single crystal diffraction, the spectral weight ratio between peak Ŭand ƀ should be $S_{Ŭ}/S_b = 1.78$ (in this simulation we set the inversion to 36 %).

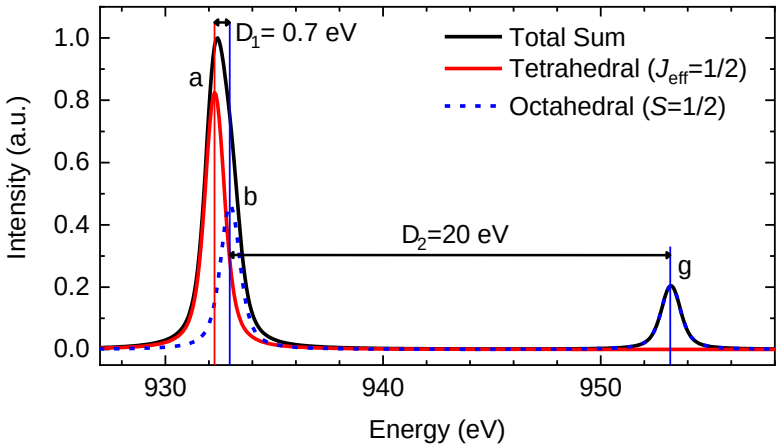


**FIG.3.8 Simulation of XAS using CTM4XAS.**

## 3.4 XAS experiment on $CuAl_2O_4$

X-ray absorption spectroscopy was done on the beamline 2A with the energy resolution of 0.1 eV in the Pohang Accelerator Laboratory. $CuAl_2O_4$ single crystal sample was measured using a total electron yield mode at room temperature. The beam is linearly polarized in a

horizontal direction. The spectrum shows main peaks at ~930 and ~950 eV for $L_3$- and $L_2$-edge transition, respectively. In $L_3$-edge, the main peak looks asymmetric, which indicates the $L_3$-edge is composed of two peaks, Ŭand ɓ but in $L_2$-edge, a peak ɔ has a symmetric shape. This overall shape of the observed spectrum is identical to the simulation results discussed in section 3.3 having the $J_{eff}$ = 1/2 as a ground state for the copper tetrahedral site.

(a) $L_3$ edge (b) $L_2$ edge

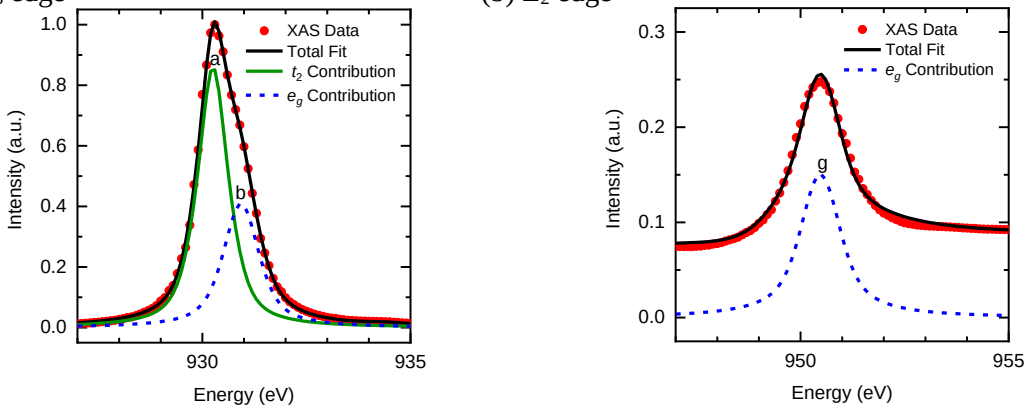


**FIG.3.9 X-ray absorption spectroscopy data for $CuAl_2O_4$. (a) $L_3$ edge is composed of $t_2$ and $e_g$ contributions (peak Ŭand ɓ respectively) (b) $L_2$ edge is composed of $e_g$ contribution only (peak ɔ).**

The experimental results qualitatively coincide with the calculation but to identify the quantitative matching between the experiment and the simulation, the peaks in XAS data was assigned using pseudo-Voight peaks provided by the óAthenaô software, [Ref.3.21]. The background was removed using linear and arctangent functions [Ref.3.19]. The main three peaks: 1, 2, 5, which correspond to the peaks Ŭ, ɓ, ɔ in FIG.3.9 are fitted to pseudo-

Voight functions with the same profile shape factor, ɖ and Gaussian FWHM. The profile of each peak is depicted in FIG.3.10 and TABLE 3.1. The Lorentzian FWHM of the peaks can be a gauge for determining the number of peaks in the $L_2$ edge. If the $L_2$ edge is composed of two peaks like $L_3$, then Lorentzian FWHM of peak 5 should be as large as 1.0 (the averaged Lorentzian FWHM of Ŭand ɓ) + 0.6 (the peak position difference between Ŭand ɓ, æ$_1$) + 0.5 (Coster-Kronig width [Ref.3.22]) = 2.1 eV. However, its real value is 1.4(1) eV, which is rather close to 1.1 (the Lorentzian FWHM of ɓ) + 0.5. The broad humps like peak 3 and 4 can originate from 2*p* to 4*s* and 2*p* to continuum edge transitions [Ref.3.19].

The spectral weight ratio between the peaks Ŭand ɓ, $S_{Ŭ}/S_{ɓ}$ is 1.75(2), which coincides with the inversion of 36 % [see TABLE 3.2]. The distance between Ŭand ɓ, æ$_1$ is 0.6(1) eV which depends on the size of 10Dq and SOC constant corresponds to that of the simulation. The ratio between the peaks ɓ and ɔ, $S_{ɓ}/S_{ɔ}$ is also close to 2, the BR of conventional cuprate systems [Ref.3.23]. Moreover, separation distance between the peaks ɓ and ɔ, æ$_2$ is ~20 eV, which also agrees with the distance between $L_3$- and $L_2$-edge in simple cuprates [Ref.3.19,20]. The overall experimental spectrum can be simulated using a model of localized A- and B-site $Cu^{2+}$ ions.

Comparing the experimental data and the simulation, we can confirm that the shape of the two spectra are the same except that there is an overall shift within a few eV, which frequently happens depending on the calibration of the beamline. The small difference in æ$_2$ can originate from the difference of the SOC constant of 2*p* core level between a free atom (the calculation via CTM model) and the lattice. The deviation of BR from 2 can be

seen both simulation and experiment, which comes from the interplay of the multiplet effect and the SOC of 3*d* orbital. [Ref.3.24].

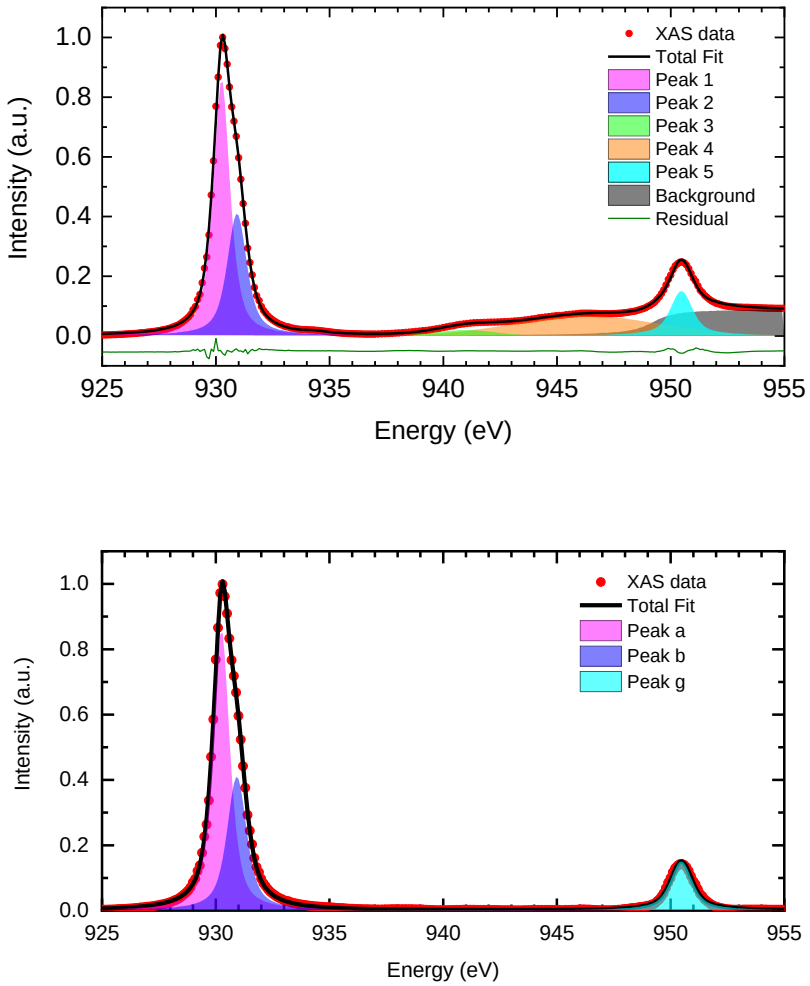


**FIG.3.10. (Upper) Experimental XAS data and the profile of each fitted peak. (Lower) The main three peaks by subtracting background and the humps from charge transfer transitions: 1, 2, 5 correspond to Ŭ, ɓ, ɔ.**

**TABLE 3.1 The profile of the each fitted peak in FIG.3.10.**

| | Position (eV) | Spectral Weight, $S_i$ (a.u.) | ḍ | Gaussian FWHM (eV) | Lorentzian FWHM (eV) |
|---|---|---|---|---|---|
| Peak 1 (Ŭ) | 930.3(1) | 1.05(1) | 0.76(1) | 1.0(1) | 0.8(1) |
| Peak 2 (ɓ) | 930.9(1) | 0.60(1) | 0.76(1) | 1.0(1) | 1.1(1) |
| Peak 3 | 941.0(6) | 0.07(2) | 0 | 3.2(6) | - |
| Peak 4 | 946.3(2) | 0.52(2) | 0 | 7.5(5) | - |
| Peak 5 (ɔ) | 950.5(1) | 0.26(1) | 0.76(1) | 1.0(1) | 1.4(1) |
| Arctan. Bgd. | e0: 949.2(5) | step: 0.092(2) | - | width: 0.7(1) eV | |

**TABLE 3.2 Comparison of the parameters of simulation and experiment.**

| | $æ_1$ (eV) | $S_Ŭ/S_ɓ$ | $æ_2$ (eV) | $S_ɓ/S_ɔ$ |
|---|---|---|---|---|
| Simulation | 0.7 | 1.78 | 20.2 | 2.27 |
| Experiment | 0.6(1) | 1.75(2) | 19.6(1) | 2.29(6) |

## 3.5 Discussion and summary

### 3.5.1 Magnetism of $CuAl_2O_4$

The verification of the ground state of $CuAl_2O_4$ further raises questions about the magnetic properties of the system. The direct current (DC) magnetic susceptibility under 500 Oe and

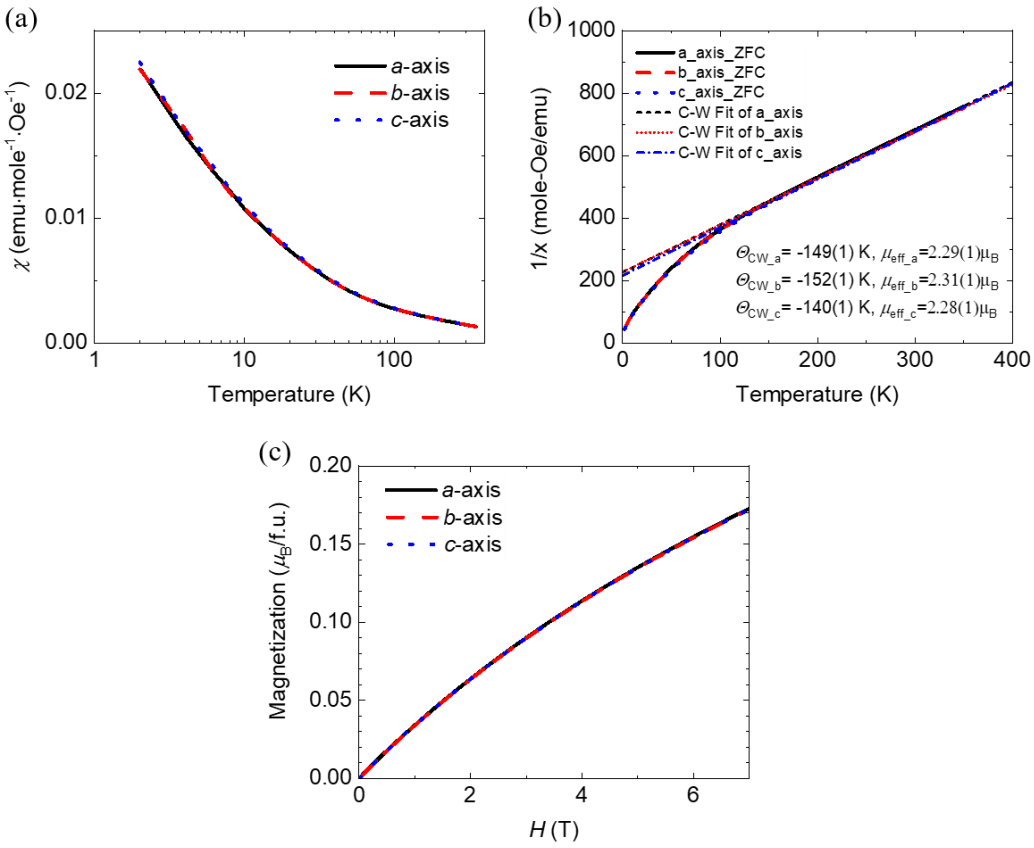


**FIG.3.11. The magnetic properties measurement for $CuAl_2O_4$ along the each crystallographic axis. (a) DC magnetic susceptibility under 500 Oe. (b) The inverse susceptibility and the result of the Curie-Weiss fit for each axis. (c) Magnetization at 2 K.**

the magnetization at 2 K were measured by MPMS-3 (Quantum Design) when the magnetic field is aligned along the each crystallographic axis. Since the lattice is cubic, after the *a*-axis was chosen arbitrarily, then the other orthogonal *b*- and *c*-axes were assigned.

There is no anomaly on each data but it shows paramagnetic behavior down to the Curie-Weiss (C-W) temperature, which indicates the absence of long-range order down to 2 K. Based on the fact that the differences between the data on the each axis is little, this system seems to be almost magnetically isotropic. This also corresponds to the cubic structure of the system because if the system has a distortion, the overlap of the spin-orbital wave function would be different along the each crystallographic axis. This will change the hopping integrals and the magnetic anisotropy of the system. According to the Curie-Weiss fit, the effective moments, $\varepsilon_{eff}$ are ~2.3$\varepsilon_B$ and the Curie-Weiss temperatures, $d_{CW}$ are ī 140-150 K. The effective moment is quite larger than that of $S$ = 1/2 case ($\varepsilon_{eff}$ = 1.73$\varepsilon_B$) but close to that of Ŭ-$RuCl_3$ ($\varepsilon_{eff}$ = 2.2$\varepsilon_B$) [Ref.3.25,26]. It is natural to expect that for the $J_{eff}$ = 1/2 state, the magnetic moment will be larger than that of $S$ = 1/2 due to the contribution of the unquenched effective orbital angular momentum, which is parallel to the spin angular momentum [Ref.3.1] and the effective orbital angular momentum can make Land®$g$-factor larger than 2 [Ref.3.27]. Because $CuAl_2O_4$ is the most localized system among other the $J_{eff}$ = 1/2 systems ($U_{CuAl2O4}$ > 6 eV, $U_{Ŭ\text{-}RuCl3}$ ~ 1.5 eV and $U_{Sr2IrO4}$ ~ 2 eV), it has the largest local moment.

Even though the exchange interaction estimated from $d_{CW}$ is quite large, there is no long-range order down to 2 K, which means that the magnetic moments are frustrated. The frustration factor, $T_N/|d_{CW}|$ is at least larger than 70 and the system, therefore, is a highly

frustrated system. The origin of the frustration can be related to the interplay of nearest and next nearest neighbor exchange interactions ($J_1$ and $J_2$, respectively) in a diamond lattice [Ref.3.28]. If the $J_2/J_1$ is larger than 1/8, the ground state is the spiral quantum spin liquid with the massive degeneracy in the spiral propagation wavevectors. However, according to the previous low-temperature DC magnetic susceptibility and alternating current (AC) magnetic susceptibility measurement [Ref.3.11], the moments of $CuAl_2O_4$ show glassy behavior rather than spin liquid nature. There is a divergence between field-cooled (FC) and zero-field-cooled (ZFC) susceptibility below $T_f$ = 2 K and the position of a peak in AC susceptibility varies with the frequency of AC field.

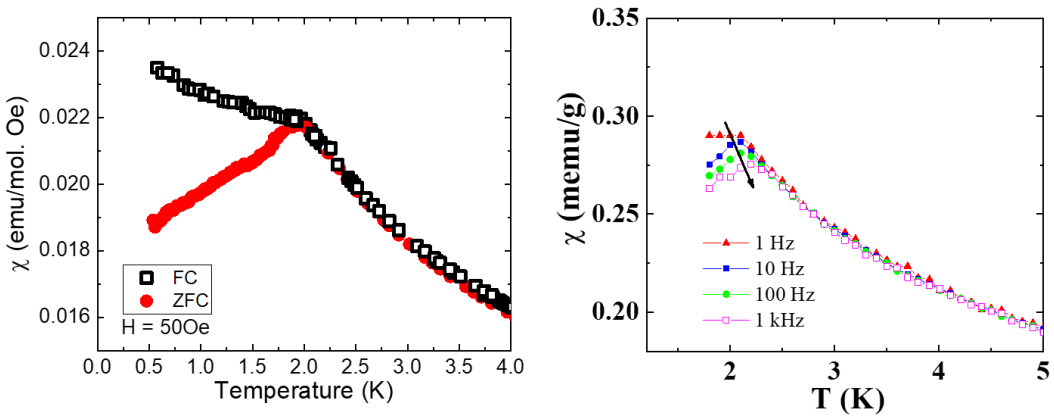


**FIG.3.12. (Left) DC magnetic susceptibility down to 0.5 K using MPMS-XL equipped with $^3$He option. (Right) AC magnetic susceptibility varying the frequency of AC field [Ref.3.11].**

To observe the nature of local moments, muon spin relaxation ($\varepsilon$SR) and nuclear magnetic resonance (NMR) experiments were conducted. First, $\varepsilon$SR is done with polycrystalline $CuAl_2O_4$ sample in ISIS muon source in UK using both dilution and dilution refrigerator

option (down to 0.1-4 K) and cryostat option (2-15 K). FIG.3.13 shows raw asymmetry data of $\varepsilon$SR via two different options. Down to 0.1 K, which is $\frac{1}{20}$ K, the asymmetry doesn't show an oscillation pattern like sinusoidal functions, which is the hallmark of long-range order of magnetic moments but it decreases as a function of time. The moments of $CuAl_2O_4$, therefore, doesn't order down to $\frac{1}{20}$ K.

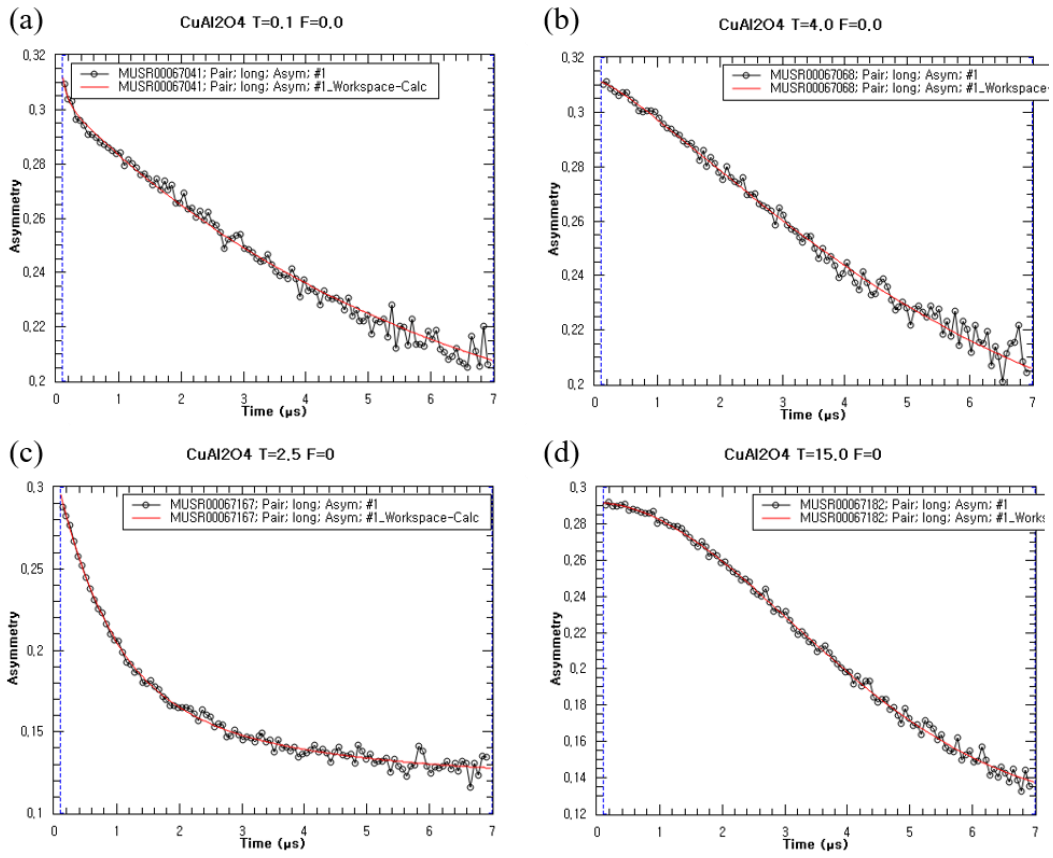


**FIG.3.13. (a), (b) Asymmetry of $\varepsilon$SR experiment data at 0.1 and 4 K, respectively using a dilution refrigerator option. The red lines are fitting lines to the data using 'Mantid'. (c), (d) Asymmetry data at 2.5 and 15 K, respectively using a cryostat option.**

The experimental data were fitted to an empirical decay function, ö ò سٍ öٍ٩ خوف ٩ طى ٣ öٍ٩ خوف [Ref.3.29] by utilizing a $\varepsilon$SR analysis package, ôMantidô [Ref.3.30]. The slow decaying first term originates from contribution of both sample and sample holder, and the other fast decaying term is related to a sample [Ref.3.29]. The result of the fitting is summarized in FIG.3.14.

At $T > T_f$ ę σ+, only the first term is necessary to fit the data. The exponent, $b$ decreases from 2 at high temperature and it saturates to 1 at $T = T_f$ as the temperature decreases. At high temperatures, due to static nuclear moments, the Gaussian relaxation ($b = 2$) dominates and at lower temperatures, the decrease in $b$ is consistent with the slowing down of electron spins [Ref.3.29]. For the both options, at $T_f$ ę 3 K, $A_1$ starts to fall; $\lambda_1$ shows a peak; and $A_2$ and $\lambda_2$ begins to increase as well. The peak in the $\varepsilon$SR relaxation rate is usually related to spin freezing. This overall nature of $\varepsilon$SR data is consistent with that of a spin-glass compound, $Sr_2YReO_6$ [Ref.3.29]. A passing note, the presence of the other sharp peak in $\lambda_1$ around 0.3 K is questionable when we consider the large error bar of $\lambda_2$ below 0.5 K. To identify this aspect, minute scanning below 0.5 K is required.

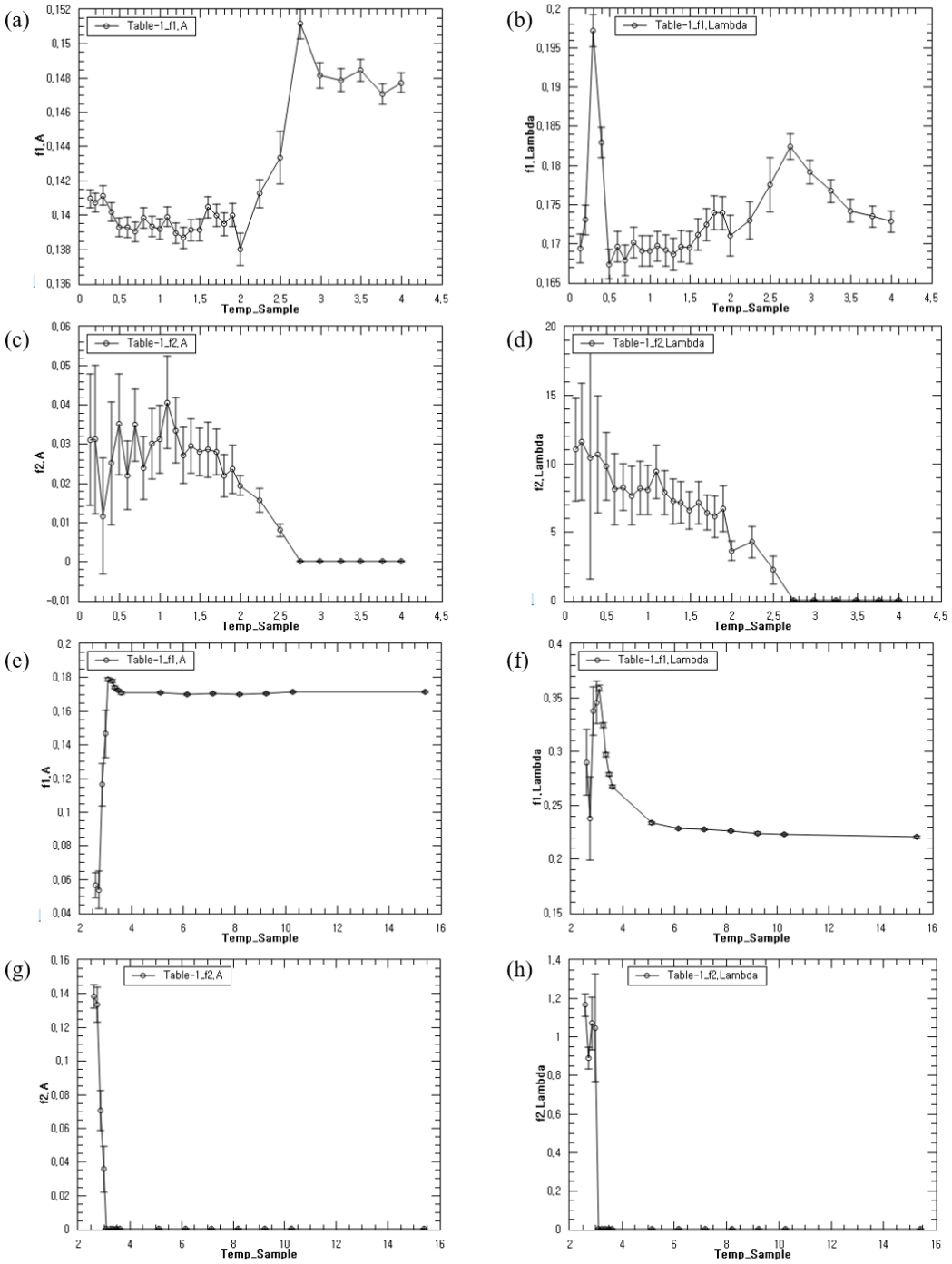


**FIG.3.14. The fitting parameters of (a) $A_1$, (b) $\partial_1$, (c) $A_2$, (b) $\partial_2$, which are obtained by fitting**

**the data from dilution refrigerator option and the fitting parameters of (e) $A_1$, (f) $\partial_1$, (g) $A_2$, (h) $\partial_2$ from cryostat option.**

NMR experiments were done using single-crystal samples at Prof. M. Takigawaôs group in Institute for Solid State Physics (ISSP), The University of Tokyo in Japan. The NMR spectra were detected around the resonance frequency of $^{27}$Al, which has nuclear spin, $I$ = 5/2. Due to the Zeeman splitting and nuclear quadrupolar resonance, there should be one central main peak and four satellite peaks in the spectra. The main peak is positioned at 22.1929 MHz since the magnetic field is 2 T and the nuclear gyromagnetic ratio of $^{27}$Al is ɔ = 11.094 MHz/T. The shift of the main peak from the reference line (the Knight shift) indicate the strength of the internal field. Due to the threefold crystal symmetry and four different trigonal axes on the Al site (site symmetry: -3 *m* and -4 3 *m*), moreover, each peak should be split further by the the crystal electric field acting on the nuclear quadrupole moment. The intensity of the satellite peaks will change with the angle of the magnetic field is rotated and especially, the peaks will be perished when the magnetic field is in (001) because at this angle, nuclear quadrupolar resonance and the splitting due to the threefold crystal symmetry will disappear. Then, the resonance frequency is

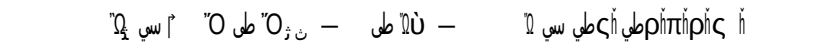

where

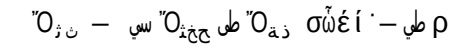

is the magnetic hyperfine field from the Cu moments, and

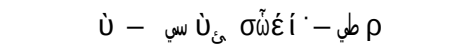

is the quadrupole frequency where $d$ is the angle between (111) and the magnetic field.

The observed spectra show a large main peak at 22.19 MHz, which corresponds to the reference resonance line of $^{27}$Al (see FIG.3.15). However, the satellite peaks are too broad to resolve in our experiments, and even though the direction of the magnetic field is changed, the intensity change of the satellite peaks is not significant. There still are shoulder peaks around the main peak even the field is aligned parallel to (001), where σẅέί·–طيρ سيπ. These characteristics can be interpreted by considering the site-inversion in Al site. The inversion leads inhomogeneous distribution of the magnitude and the direction of principal axis of the electric field like a powder sample and it broadens the peaks. Absence of shift in the main peak from the reference line also coincides with the randomness of the principal axis.

In addition, below the Curie-Weiss temperature and $T_f$, the width of the spectra keeps broadening due to the enhancement of the Cu moment. Even though the internal field of Cu around Al ions also increases, it can't develop the shift of the main peak from the reference line. This aspect shows absence of long-range magnetic order below $T_f$, which also supports glass state. Below $T_f$, the significant deference between the field-cooled (FC) and the zero-field-cooled (ZFC) data starts to evolve. It also strengthens the onset of spontaneous Cu moments at zero-field due to spin-glass freezing (see FIG.3.16). Because of the broadening of the satellite peaks, it is hard to get useful microscopic information on the spin and orbital states of Cu moments but the NMR experiment is still gives apparent information on the emergence of spin-glass state.

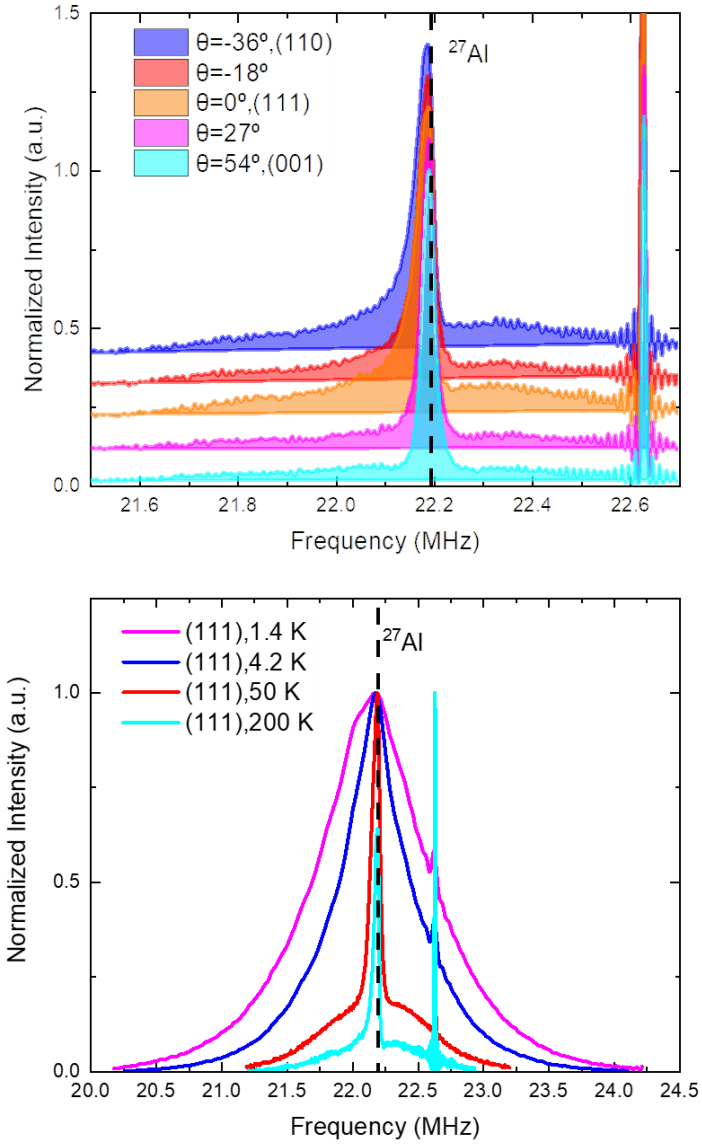


**FIG.3.15. (Upper) $^{27}$Al NMR spectra for single-crystal $CuAl_2O_4$ measured at 200 K under the external magnetic field of 2 T. The angle, *d* between (111) and the field was rotated in the $(0\bar{0}0)$ plane. The dashed line denotes the reference resonance line of $^{27}$Al and a sharp peak near 22.6 MHz comes from $^{63}$Cu in the NMR coil used for calibrating the magnetic**

**field. (Lower) The temperature dependence of NMR spectra at 1.4, 4.2, 50, and 200 K under the external field of 2 T along (111).**

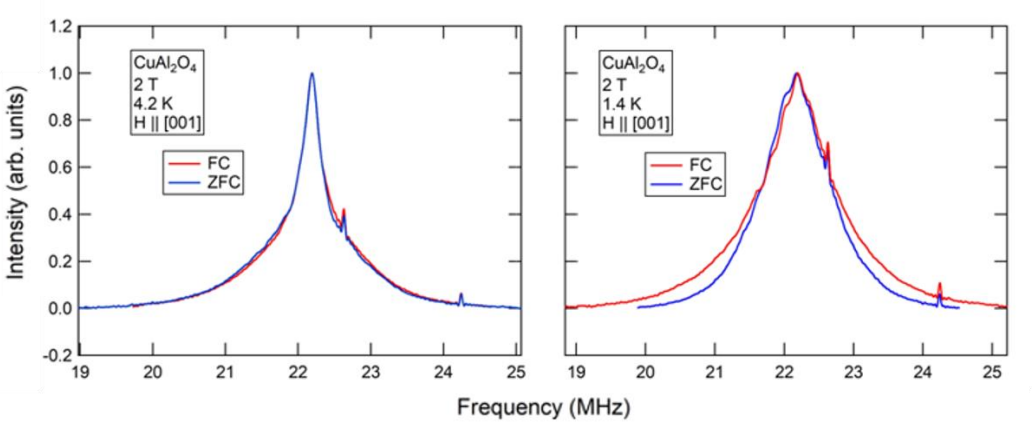


**FIG.3.16. The field-cooled and zero-field-cooled spectra below and above $T_f$. Small two peaks are from $^{63}$Cu and $^{65}$Cu in the NMR coil, respectively.**

The site-inversion of the system and the strong quantum fluctuations of the frustrated $J_{\text{eff}}$ = 1/2 wavefunctions can be the origins of the absence of a long-range order but lead to the glassy nature on the spin-orbital entangled $J_{\text{eff}}$ = 1/2 state instead of the liquid phase. This glassy nature may further related to the absence of static J-T distortion even in the octahedron site.

## 3.5.2 Summary

Using high quality $CuAl_2O$ single-crystal sample, the ground state of the system is verified to be the Mott insulating $J_{eff}$ = 1/2 state via resistance measurement, single-crystal XRD, Cu K-edge and L-edge XAS techniques. The single-crystal XRD and the K-edge spectrum show that the crystal structure of $CuAl_2O_4$ is cubic without any structural distortions even though $Cu^{2+}$ is J-T active. The possible answer for the cubic structure is the emergence of the $J_{eff}$ = 1/2 state, which is composed of the equal contribution of the *xy*, *yz*, and *zx* orbitals. The occurrence of the $J_{eff}$ = 1/2 is verified by the L-edge XAS which, shows the main peak (Ŭ) with the shoulder peak (ɓ) in the $L_3$-edge but the only one peak (ɓ) at the $L_2$-edge, which gives extraordinary larger BR of 6.3(1) than that of the conventional cuprates. Moreover, from the magnetic properties measurement, the moment of the spin-orbital $J_{eff}$ = 1/2 state is verified to be highly frustrated without a long-range order. With previous studies on the glassy nature of $CuAl_2O_4$, the ground state of this system is a novel ǿspin-orbital glassôstate.

## References

[Ref.3.1] B. J. Kim, Hosub Jin, S. J. Moon, J.-Y. Kim, B.-G. Park, C. S. Leem, Jaejun Yu, T. W. Noh, C. Kim, S.-J. Oh, J.-H. Park, V. Durairaj, G. Cao, and E. Rotenberg, Phys. Rev. Lett. **101**, 076402 (2008).

[Ref.3.2] Hideo Hosono, Keiichi Tanabe, Eiji Takayama-Muromachi, Hiroshi Kageyama, Shoji Yamanaka, Hiroaki Kumakura, Minoru Nohara, Hidenori Hiramatsu, and Satoru Fujitsu, Sci. Technol. Adv. Mater. **16**, 3 (2015).

[Ref.3.3] Y.‐J. Yan, M.‐Q. Ren, H.‐C. Xu, B.‐P. Xie, R. Tao, H.‐Y. Choi, N. Lee, Y.‐J. Choi, T. Zhang, and D.‐L. Feng, Phys. Rev. X **5**, 041018 (2015).

[Ref.3.4] Jaehong Jeong, Yvan Sidis, Alex Louat, V®onique Brouet, and Philippe Bourges, Nat. Commun. **8**, 15119 (2017).

[Ref.3.5] K. W. Plumb, J. P. Clancy, L. J. Sandilands, V. Vijay Shankar, Y. F. Hu, K. S. Burch, Hae-Young Kee, and Young-June Kim, Phys. Rev. B **90**, 041112(R) (2014).

[Ref.3.6] Seung-Hwan Do, Sang-Youn Park, Junki Yoshitake, Joji Nasu, Yukitoshi Motome, Yong Seung Kwon, D. T. Adroja, D. J. Voneshen, Kyoo Kim, T.-H. Jang, J.-H. Park, Kwang-Yong Choi, and Sungdae Ji, Nat. Phys. **13**, 1079 (2017).

[Ref.3.7] Y. Kasahara, T. Ohnishi, Y. Mizukami, O. Tanaka, Sixiao Ma, K. Sugii, N. Kurita, H. Tanaka, J. Nasu, Y. Motome, T. Shibauchi, and Y. Matsuda, Nature **559**, 227 (2018).

[Ref.3.8] Xiangang Wan, Ari M. Turner, Ashvin Vishwanath, and Sergey Y. Savrasov, Phys. Rev. B **83**, 205101 (2011).

[Ref.3.9] A. B. Sushkov, J. B. Hofmann, G. S. Jenkins, J. Ishikawa, S. Nakatsuji, S. Das

Sarma, and H. D. Drew, Phys. Rev. B **92**, 241108(R) (2015).

[Ref.3.10] Manabu Takahashi and Jun-ichi Igarashi, Phys. Rev. B **59**, 7373 (1999).

[Ref.3.11] R Nirmala, Kwang-Hyun Jang, Hasung Sim, Hwanbeom Cho, Junghwan Lee, Nam-Geun Yang, Seongsu Lee, R M Ibberson, K Kakurai, M Matsuda, S-W Cheong, V V Gapontsev, S V Streltsov, and Je-Geun Park, J. Phys.: Condens. Matter **29** 13LT01 (2017).

[Ref.3.12] Choong-Hyun Kim, Ara Go, Hwanbeom Cho, Santu Baidya, Vladimir V. Gapontsev, Byeong-Gwan Cho, Deok-Yong Cho, Taehun Kim, Younghak Kim, Tae Yeong Koo, Sergey V. Streltsov, Daniel I. Khomskii, Hosub Jin, and Je-Geun Park, (under review).

[Ref.3.13] A. L. Ankudinov, B. Ravel, J. J. Rehr, and S. D. Conradson, Phys. Rev. B **58**, 7565 (1998).

[Ref.3.14] K. Maiti, D. D. Sarma, T. Mizokawa, and A. Fujimori, Phys. Rev. B **57**, 1572 (1998).

[Ref.3.15] J. P. Clancy, N. Chen, C. Y. Kim, W. F. Chen, K. W. Plumb, B. C. Jeon, T. W. Noh, and Young-June Kim, Phys. Rev. B **86**, 195131 (2012).

[Ref.3.16] Min Yong Jeong, Seo Hyoung Chang, Beom Hyun Kim, Jae-Hoon Sim, Ayman Said, Diego Casa, Thomas Gog, Etienne Janod, Laurent Cario, Seiji Yunoki, Myung Joon Han, and Jungho Kim, Nat Commun. **8**, 782 (2017).

[Ref.3.17] Hidekazu Ikeno, Frank M F de Groot, Eli Stavitski, and Isao Tanaka, J. Phys.: Condens. Matter **21**, 104208 (2009).

[Ref.3.18] Seung Woo Jang, Takao Kotani, Hiori Kino, Kazuhiko Kuroki, and Myung Joon Han, Scientific Reports **5**, 12050 (2015).

[Ref.3.19] Ritimukta Sarangi, Nermeen Aboelella, Kiyoshi Fujisawa, William B. Tolman,

Britt Hedman, Keith O. Hodgson, and Edward I. Solomon, J. Am. Chem. Soc. **128**, 8286 (2006).

[Ref.3.20] K O Kvashnina, S M Butorin, A Modin, I Soroka, M Marcellini, J-H Guo, L Werme, and J Nordgren, J. Phys.: Condens. Matter **19**, 226002 (2007).

[Ref.3.21] B. Ravel and M. Newville, J. Synchrotron Rad. **12**, 537 (2005).

[Ref.3.22] E. Antonides, E. C. Janse, and G. A. Sawatzky, Phys. Rev. B **15**, 1669 (1977).

[Ref.3.23] Ritimukta Sarangi, Serena DeBeer George, Deanne Jackson Rudd, Robert K. Szilagyi, Xavi Ribas, Concepci· Rovira, Manuel Almeida, Keith O. Hodgson, Britt Hedman, and Edward I. Solomon, J. Am. Chem. Soc. **129**, 2316 (2007).

[Ref.3.24] F. Groot, Physica B **208-209**, 15 (1995).

[Ref.3.25] Y. Kobayashi, T. Okada, K. Asai, M. Katada, H. Sano, and F. Ambe, Inorg. Chem. **31**, 4570 (1992).

[Ref.3.26] S. Agrestini, C.-Y. Kuo, K.-T. Ko, Z. Hu, D. Kasinathan, H. B. Vasili, J. Herrero-Martin, S. M. Valvidares, E. Pellegrin, L.-Y. Jang, A. Henschel, M. Schmidt, A. Tanaka, and L. H. Tjeng, Phys. Rev. B **96**, 161107(R) (2017).

[Ref.3.27] Daniel I. Khomskii, *Transition Metal Compounds*, (Cambridge University Press, Cambridge, 2014).

[Ref.3.28] Doron Bergman, Jason Alicea, Emanuel Gull, Simon Trebst, and Leon Balents, Nat. Phys. **3**, 487 (2007).

[Ref.3.29] A. A. Aczel, Z. Zhao, S. Calder, D. T. Adroja, P. J. Baker, and J.-Q. Yan, Phys. Rev. B **93**, 214407 (2016).

[Ref.3.30] O. Arnold, J. C. Bilheux, J. M. Borreguero, A. Buts, S. I. Campbell, L. Chapon,

M. Doucet, N. Draper, R. Ferraz Leal, M. A. Gigg, V. E. Lynch, A. Markvardsen, D. J. Mikkelson, R. L. Mikkelson, R. Miller, K. Palmen, P. Parker, G. Passos, T. G. Perring, P. F. Peterson, S. Ren, M. A. Reuter, A. T. Savici, J. W. Taylor, R. J. Taylor, R. Tolchenov, W. Zhou, J. Zikovsky, Nucl. Instrum. Methods Phys. Res. A **764**, 156 (2014).

# Chapter 4
# Properties of $S$ = 1/2 Triangular-Lattice Antiferromagnets $CuY_2Ge_2O_8$ and $CuLa_2Ge_2O_8$

## 4.1 Quantum 2D triangular lattice

### 4.1.1 Enhancement of quantum fluctuation effects in 2D quantum triangular lattice

A Heisenberg model is a convenient theoretical tool that can be used to understand the ground state of an isotropic magnetic system. When the exchange interaction between neighboring spins is of antiferromagnetic (AF) nature, two competing ground states capture the landscape of possibilities: a simple Néel-type long-range ordered (LRO) state described within the framework of classical mechanics [Ref.4.1] and a spin-singlet state formed by a superposition of spin states, which is a purely quantum mechanical concept [Ref.4.2]. The energy of the Néel-type ground state is $-\frac{z}{2}S^2J$ per spin with $z$ being the number of the nearest neighbors. This ground state energy varies depending on whether the system is a one-dimensional (1D) chain, a two-dimensional (2D) square lattice, or a three-dimensional (3D) cubic system. On the other hand, the energy per spin of the singlet ground state is

$-\frac{1}{2}S(S+1)J$ for all three cases. Dimensionality therefore naturally controls the competition.

Specifically, the singlet state is a competitive ground state for 1D quantum spin ($S$ = 1/2) systems because of its lower energy whereas the Néel-ordered state wins over the singlet ground state for 3D systems. For 2D systems, however, there is competition between the Néel-ordered state and the singlet state since the energies of both cases become very similar to one another. This argument makes the 2D magnetic systems interesting and explains why, as compared with either 1D or 3D systems, 2D systems have a tendency of singlet and Néel ordered ground states found in close proximity in the parameter space of physical quantities [Ref.4.3-14]. In addition, geometrical frustration can further prevent a system from ordering in either simple Néel type or singlet type states and thus can lead to exotic physical phenomena at low temperatures [Ref.4.6-18]. This is especially true for 2D triangular lattice systems as compared with 2D square lattice systems, the latter of which is often found in the Néel-ordered state due to the weakness of the diagonal next-nearest neighbor interactions [Ref.4.19].

Remarkably, in 2D triangular Heisenberg antiferromagnet (HAFM) systems, quantum mechanics can do its work in another way. For 2D HAFM systems that enter an LRO ground state, various spin configurations appear suddenly under magnetic fields [Ref.4.6-12,15-18]. For classical spins, the ground state is expected to be the so-called 120° structure with the ground state being continuously degenerate [Ref.4.20]. As an external magnetic field is applied and increases in strength, spins become preferentially aligned along the field direction. Therefore one would naturally expect a monotonous magnetic field

dependence of the magnetization curve $M(H)$ [Ref.4.16,20,21]. However, in real quantum 2D triangular systems, the combination of low dimensionality, geometric frustration, and quantum spin nature remarkably enhances quantum fluctuations that break the otherwise degenerate ground state. Consequently, there are sometimes abrupt changes between different spin configurations leading to plateau-type behavior in the $M(H)$ curves [Ref.4.15-18].

## 4.1.2 Quantum phase transitions in 2D triangular HAFM driven by quantum fluctuations

Triangular HAFMs host various kinds of quantum phase transitions driven by quantum fluctuations. For example, a 1⁄3 plateau phenomenon was observed some time ago in $Cs_2CuBr_4$, a system regarded as a quasi-2D HAFM system [Ref.4.6] and again more recently in $Ba_3CoSb_2O_9$, a system regarded as an ideal 2D HAFM system [Ref.4.7]. In both cases, the 120° ordered spin configuration changes to an up-up-down (*uud*) configuration, inducing the emergence of the plateau with one-third of the saturated magnetization, $M_S$ in the $M(H)$ curve. The magnetic structure further changes into a coplanar configuration at higher magnetic fields. Moreover, other anomalies in $M(H)$ have been reported at higher fractions of $M$s that can originate from other competing quantum spin phases. Notable examples of such phases include those at 1⁄2, 5⁄9, and 2⁄3 of $M_S$ in $Cs_2CuBr_4$ [Ref.4.8] and a phase with 3⁄5 of $M$s in $Ba_3CoSb_2O_9$, [Ref.4.9-11]. Interestingly, $Cs_2CuCl_4$, isostructural with $Cs_2CuBr_4$, is reported to have a fractional quantum spin-liquid phase above the

transition temperature of the LRO ground state [Ref.4.14]. On the other hand, in $CsCuCl_3$, another quasi-2D HAFM system, a quantum phase transition was previously identified at a transition point from an umbrellalike configuration to a coplanar configuration when the magnetic field is applied along the *c*-axis. This quantum phase transition originates from the competition between quantum fluctuations and a magnetic anisotropic energy, which yields a step like behavior in the *M*(*H*) curve [Ref.4.12].

### 4.1.3 Candidate material for 2D triangular HAFM: Cu$R_2Ge_2O_8$ (*R* = Y, La)

As demonstrated many times in the field before, finding a new sample has been one of the key driving forces in pushing the boundary of quantum magnetism and so unearthing new phenomena. In particular, materials with a new lattice have been a fertile ground for finding novel physics. Here, a possibly new form of 2D quantum magnetism in Cu$R_2Ge_2O_8$ (*R* = Y and La) is identified. For example, one earlier structural work reported that the $CuNd_2Ge_2O_8$ system (*C*1*m*1, monoclinic) has a quasi-1D copper octahedral ($CuO_6$) corner-shared zigzag chain along the *a* axis, while neodymium oxide dodecahedral ($NdO_8$) co-linked chains are running along the *c* axis [Ref.4.22]. Spectroscopic measurements were also performed to investigate various types of germanium oxide polyhedral by classifying vibration modes [Ref.4.22,23]. In these previous works, the $Nd^{3+}$ ion (total angular momentum, $J = 9/2$) plays a dominant role in determining the physical properties of $CuNd_2Ge_2O_8$ system. Unfortunately, this dominant role played by Nd then makes it harder

to study the otherwise interesting physical phenomena arising from the 1D copper quantum spins. For instance, magnetic measurements have shown simple paramagnetic behavior with an anomaly attributed to the crystal-field splitting of Nd ions [Ref.4.22]. There have been no single-crystal studies on the same chemical formula with nonmagnetic rare-earth element such as Y and La. Furthermore, it is very important to determine the chemical structure accurately using a single-crystal sample in order to understand better the physical properties.

This work reports a comprehensive study of the crystal structure and physical properties of Cu$R_2Ge_2O_8$ ($R$ = Y, La) by using both single-crystal and polycrystalline samples. By choosing a nonmagnetic version of the Cu$R_2Ge_2O_8$ system with Y and La, the physical phenomena solely related to the quantum spin of $Cu^{2+}$ are aimed to be studied and its behavior in the new low-dimensional lattice is explored. By carrying out bulk measurements down to 0.08 K and up to 90 kOe, in addition to high-resolution single-crystal and powder diffraction measurements, it is demonstrated that the Cu$R_2Ge_2O_8$ system is a new quantum magnetic system revealing a 2D triangular lattice and novel magnetic field induced phase transitions.

## 4.2 Crystal structure of Cu$R_2Ge_2O_8$ ($R$ = Y, La)

The structure analysis using x-ray and neutron diffraction instruments confirms that all the samples of Cu$R_2Ge_2O_8$ ($R$ = Y, La) form in the space group $I1m1$ [see the Chapter 2]. The refined crystal structure of the Cu$R_2Ge_2O_8$ system is found to have a 2D triangular magnetic

lattice as shown in FIG.4.1, where the blue, green, and grey balls represent the Cu, La, and Ge atoms, respectively. Oxygen atoms are omitted for clarity and instead their positions are indicated by the red ends of sticks stretched from the copper atoms to the corner of the germanium oxide polyhedra. The final structures also show the $CuO_6$ corner-shared chains running along the *a* axis by linking the copper and oxygen atoms as in the $CuNd_2Ge_2O_8$ case [Ref.4.22] with the *C*1*m*1 unit cell setting [for the *I*1*m*1 unit cell setting the chain direction runs along the $J_3$ direction as shown in FIG.4.1(b)]. However, there is one striking difference between the current refined final structure and that reported of $CuNd_2Ge_2O_8$ [Ref.4.22]; which is that according to the present analysis the copper octahedra are highly distorted due to the Jahn-Teller effect, while the earlier work shows a significantly smaller distortion. For example, in this structural model the bond lengths between the central copper and oxygen atoms in the distorted equatorial plane (O6, O7, O8, and O9) are about 1.76(1)-1.98(1) Å whereas the bond lengths between the copper and two apical oxygen atoms (O10) are 2.63(2) and 2.71(1) Å, respectively [see FIG.4.1(c)]. As the apical bond lengths are larger than 2.13 Å, which is the sum of ionic radii of $Cu^{2+}$ and $O^{2-}$, the orbital overlap between $Cu^{2+}$ and $O^{2-}$ is expected to be very small along the apical direction. Therefore, the copper oxide polyhedra of $CuR_2Ge_2O_8$ (*R* = Y, La) do not have the usual $CuO_6$ octahedron, which is rather unusual among Cu oxides. Instead, the $CuO_4$ plaquette should be considered as a basic building block. This then leads to a rethink about the crystal structure. After trials with several other possibilities, it can be concluded that in contrast to the previous claim for $CuNd_2Ge_2O_8$ [Ref.4.22] there is no evidence of the 1D chain in the present final refined crystal structure of $CuLa_2Ge_2O_8$.

Since there is no 1D chain along the *a* axis, there is no reason to stick with the *C*1*m*1 unit cell setting used in [Ref.4.22]. Thus, instead, the *I*1*m*1 cell setting is adopted in the structural analysis, which is more appropriate for the description of the coordination of the copper ion by transforming the *c* and *a*+*c* vectors of *C*1*m*1 to *a* and *c* unit vectors of *I*1*m*1, respectively. Typical refinement results are shown in FIG.2.5. TABLE 2.1 summarizes the structural information of the lattice parameters, atomic positions, thermal parameters, and agreement factors for $CuLa_2Ge_2O_8$.

For the benefit of the later discussion on the bulk properties, and in particular the magnetic properties, the crystal structure should be examined further in detail. The distorted $CuO_4$ plaquette can interact with the adjacent ones so that the four different exchange integrals: $J_1$, $J_2$, $J_3$, and $J_4$ [see FIG.4.1 (a)] can be assigned. The direct distances between the neighboring copper ions along each path are 5.16(1)-5.21(1) ($J_1$, $J_2$, $J_3$) and 6.48(2) Å ($J_4$), respectively. Therefore the exchange interactions along $J_1$, $J_2$, and $J_3$ are expected to be about the same, while $J_4$ should be smaller than the other three. In this scenario, the magnetic lattice of Cu ions in the $CuR_2Ge_2O_8$ ($R$ = Y, La) system becomes a 2D triangular lattice within the *ac* plane [see FIG.4.1 (b)]. At the same time, the actual magnitude of the exchange interaction is expected to be significantly smaller than that of other Cu oxides including cuprates [Ref.4.27-29] for the following reason. The neighboring $CuO_4$ plaquettes are well separated by germanium and the rare earth atoms; Ge1 and Ge2 atoms make $GeO_4$ tetrahedra that form a grid in the *ac* plane separating copper oxide triangular plane [see FIG.4.1(a)], whereas Ge3 atoms construct $GeO_5$ trigonal bipyramids that block the copper-oxygen-copper link in the triangle [see FIG.4.1(c)].

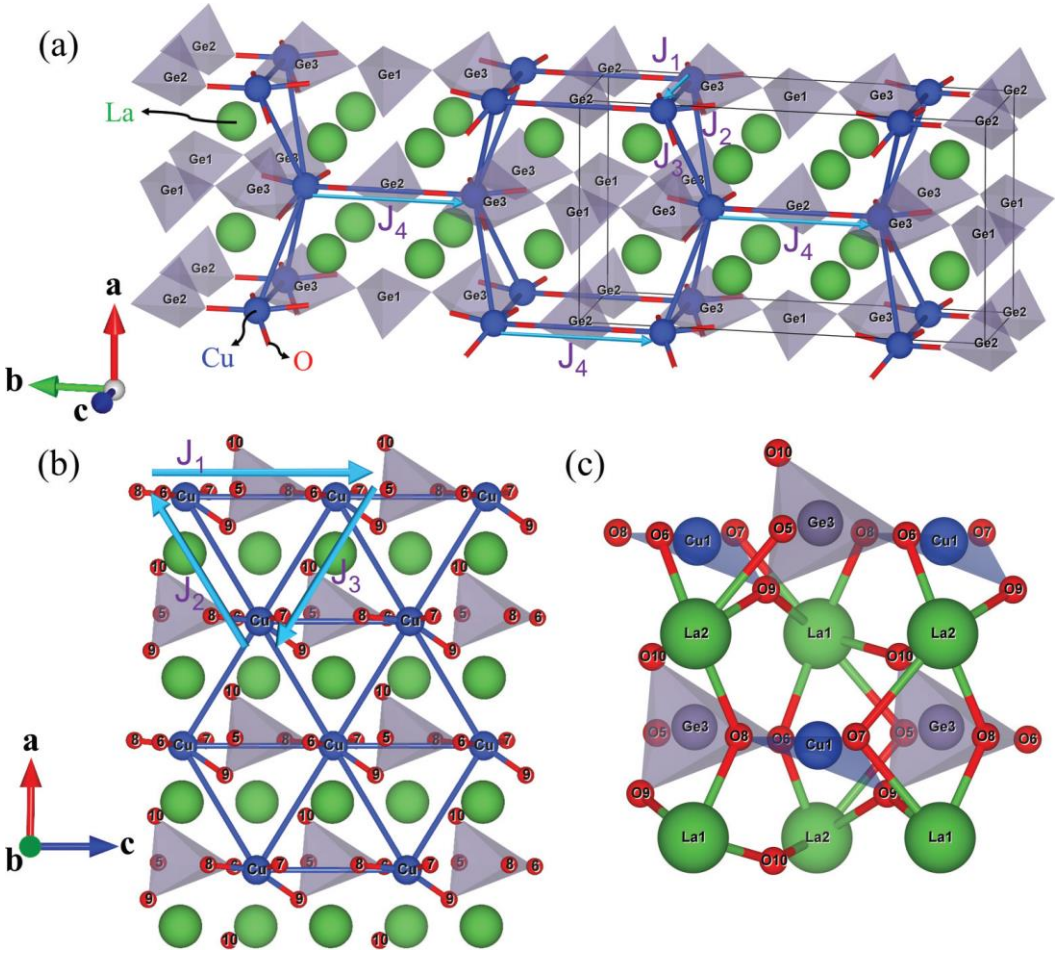


**FIG.4.1 Crystal structure of $CuLa_2Ge_2O_8$ in the *I*1*m*1 unit cell setting. The blue, green, and grey spheres indicate the copper, lanthanum, and germanium atoms, respectively. (a) There are four different exchange paths: $J_1$, $J_2$, $J_3$, and $J_4$. Ge1 and Ge2 atoms make $GeO_4$ tetrahedra that form a grid in the *ac* plane and Ge3 atoms construct $GeO_5$ trigonal bipyramids. (b) $CuO_4$ plaquette forms a 2D triangular lattice within the *ac* plane. (c) The Cu-O10 lengths are much longer than Cu-O lengths on the distorted equatorial plane while La and Ge atoms are separating the nearest $CuO_4$ plaquettes and so prohibiting the**

**formation of the Cu-O-Cu bonding between the adjacent $CuO_4$ plaquettes.**

## 4.3 Bulk properties of $Cu\boldsymbol{R}_2Ge_2O_8$ ($\boldsymbol{R}$ = Y, La)

### 4.3.1 Magnetic measurements

To orient single crystals for bulk measurements, an Imaging Plate XRD Laue Camera (IP-XRD, IPX Co., Ltd.) was used before magnetic measurements. For example, a photo in FIG.2.5 shows a single crystal with the *b* axis of the sample perpendicular to the flat plane with an area of 750×374 $\mu m^2$: this particular sample was used for the magnetization measurements. Magnetic and thermodynamic properties of polycrystalline samples were characterized from 0.4 to 350 K using MPMS-XL5 and PPMS-9ECII (Quantum Design) equipped with a $^3$He option. Moreover, an MPMS-3 (Quantum Design) is used to measure the magnetization of the small single-crystal samples for the La case as well. For further low-temperature measurements of $CuY_2Ge_2O_8$, a collaborator Dr. Carley Paulsen of CNRS, Grenoble, France employed a home-made SQUID magnetometer equipped with a dilution refrigerator with a base temperature of 84 mK.

The temperature-dependent direct current (dc) magnetic susceptibility was measured using the polycrystalline samples. Two anomalies are immediately obvious in the data shown in FIG.4.2 (a): a broad hump centered at 0.89(1) and 1.40(4) K and an inflection point (indicated by an arrow) at $T_{LRO}$=0.50(1) and 0.93(2) K for Y and La, respectively.

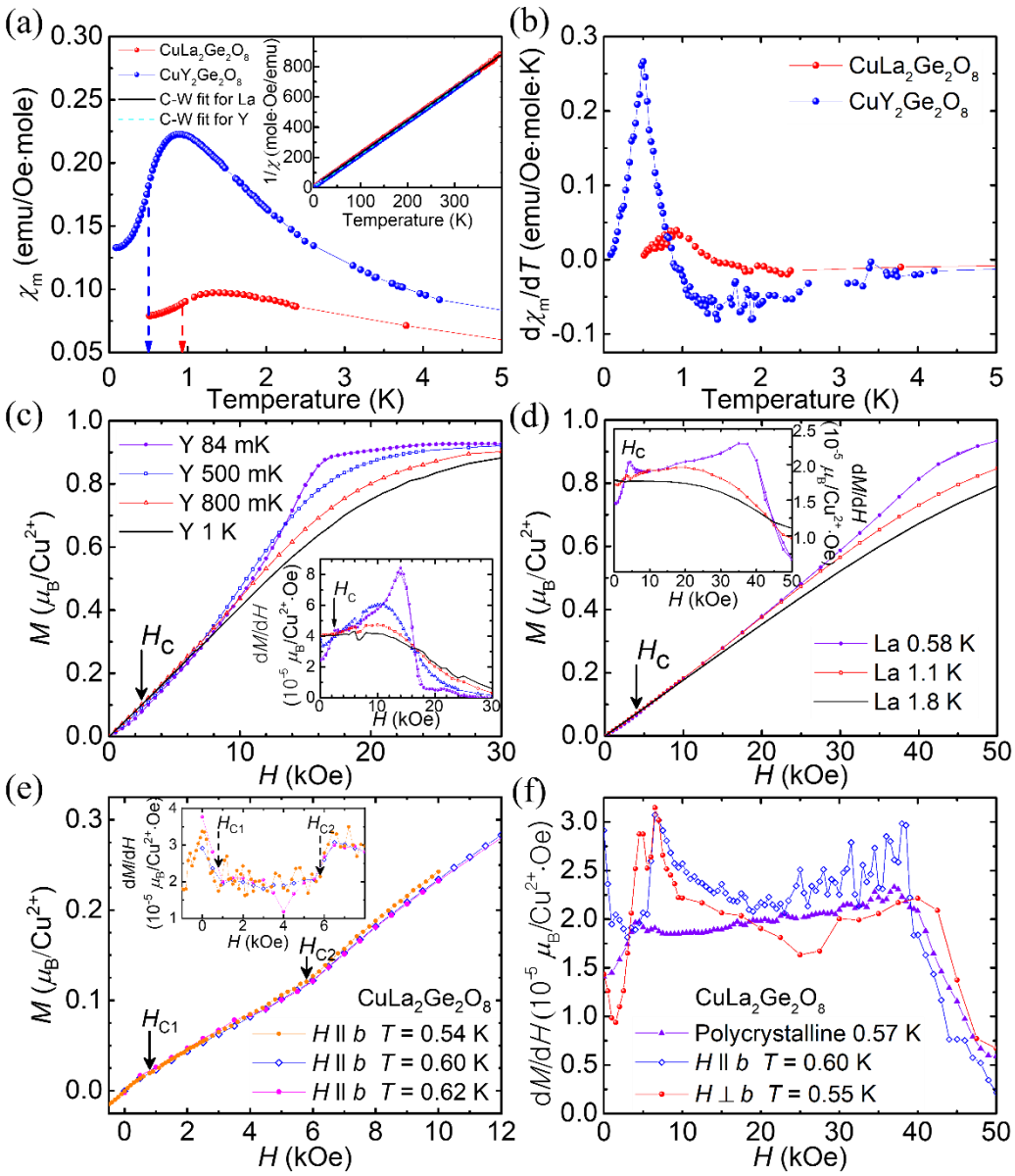


**FIG.4.2 (a) Temperature-dependent DC magnetic susceptibility $\chi_m$ of Cu$R_2$Ge$_2$O$_8$ ($R$ = Y and La). The arrows indicate the inflection points originating from long-range order. The inset shows the inverse susceptibility curves and the Curie-Weiss fitting results (dashed lines). (b) Temperature derivative of the magnetic susceptibility of Cu$R_2$Ge$_2$O$_8$ ($R$ = Y and**

**La). (c) Field-dependent magnetization $M(H)$ at various temperatures using polycrystalline $CuLa_2Ge_2O_8$. The first derivatives for both systems are shown in the inset. The position of the magnetic field-induced phase transition is indicated by an arrow. (d) Field-dependent magnetization $M(H)$ for polycrystalline $CuY_2Ge_2O_8$ and its first derivative are shown in the inset. The position of the magnetic field-induced phase transition is indicated by an arrow. (e) Magnetization $M(H)$ in $H \parallel b$ for the $CuLa_2Ge_2O_8$ single crystal at various temperatures and the first derivatives of $M(H)$ are shown in the inset. (f) Comparison of d$M$/d$H$ of the polycrystalline sample and single crystal in the crystallographic orientations $H \parallel b$ and $H \perp b$, respectively.**

The broad maximum is usually a characteristic sign of low-dimensional magnetic systems due to the AF short-range interaction [Ref.4.30-38]. In FIG.4.2(b), a peak appears clearly in the temperature derivative of the susceptibility curve as the inflection point in the susceptibility. This anomaly can originate from various kinds of phase transitions such as spin-glass and LRO. However, discussed together with the thermodynamic data later in the paper, the anomaly in $\chi(T)$ then suggests an onset of the LRO state.

From the Curie-Weiss fit [see the insert of FIG.4.2 (a)], the same effective moment value of $\mu_{\text{eff}} = 1.94(1)\mu_B$/f.u. was obtained for both $CuR_2Ge_2O_8$ ($R$ = Y, La) and the Curie-Weiss temperature $\theta_{\text{CW}} = -1.1(1)$ and $-5.7(4)$ K for the Y and La compounds. The following formula, $\chi(T) = \chi_0 + C/(T - \theta_{\text{CW}})$ is used, to fit the data over the temperature region of 6.8-350 K and 19.7-398 K for the Y and La compounds, respectively. In the equation, $\chi_0$ represents the temperature independent Van Vleck paramagnetism and diamagnetism from

elements other than Cu ($\chi_0 \cong -2\times10^{-5}$ emu mole$^{-1}$ Oe$^{-1}$ for both cases) and $C$ is the Curie constant of the Cu spins. The effective moment obtained from the fit is comparable with the theoretical effective moment of $S = 1/2$ for $Cu^{2+}$ [$g_J\mu_B(S(S+1))^{1/2} = 1.73\mu_B$], supporting the scenario of the quantum spin system being realized in $CuR_2Ge_2O_8$ ($R$ = Y, La). The negative value of $\theta_{CW}$ shows the averaged exchange interaction to be of antiferromgnetic origin. The frustration factor $f = \theta_{CW}/T_{LRO}$ is found to be larger than unity for both cases [$f_Y$ = 2.2(2) and $f_{La}$ = 6.1(4)]. This could have an origin in the effects of the geometrical frustration in the 2D triangular AF ground state [Ref.4.39]. Also, the average value of the exchange interaction estimated from the transition temperature is smaller by 2-3 orders of magnitude than in the well-known cuprate systems [Ref.4.27,28,40,41].

FIG.4.2(c) and (d) present the $M(H)$ curves measured on the polycrystalline samples at various temperatures around $T_{LRO}$ and the insets show the first derivative of $M(H)$. The magnetization and its first derivative show typical behavior of a low-dimensional quantum spin system and magnetic field-induced phase transitions. For example, the overall shape of the $M(H)$ curve is convex rather than a straight line, which is consistent with the behavior of low-dimensional quantum systems [Ref.4.6,15,21,32,42]. In the inset of FIG.4.2(c) and (d) for both La and Y compounds, the $dM/dH$ curve shows paramagnetic behavior above $T_{LRO}$: the slope decreases gradually to zero as the external magnetic field approaches the saturation field. As the temperature decreases below $T_{LRO}$, a new field-induced phase transition appears. Around zero field, the slope gets reduced compared to the $T > T_{LRO}$ case. As the external field increases, $M(H)$ displays an abrupt change at a low critical field $H_C$ [2.5(3) and 4.0(3) kOe for the Y and La compounds]. Of further interest, the $M(H)$ curve

shows a kink at $H_C$ for both compounds and there is no hysteresis around $H_C$ at the base temperature, indicative of a second order phase transition. After the abrupt change, the slope gradually increases with the magnetic field and finally reaches a maximum before decreasing to zero with the magnetization value approaching its saturation moment value. The saturation field of both compounds [14.0(3) and 38.0(3) kOe for Y and La compounds, respectively] is also comparable with the energy scales of the exchange interactions estimated from $\theta_{CW}$. The saturated magnetization value is close to $1\mu_B/Cu^{2+}$, corresponding to a quantum spin system where $gS = 1$ ($g = 2$ is the Landé $g$ factor and $S = 1/2$ is the spin angular momentum number).

In order to examine the field-induced transitions more closely, the $M(H)$ is measured with magnetic field applied along two perpendicular directions using the single crystal of $CuLa_2Ge_2O_8$ as shown in FIG.2.5. Upon increasing the magnetic field along the $b$ axis perpendicular to the triangular plane, $M(H)$ increases but its derivative decreases until $H_{C1}$ = 0.80(5) kOe, where the slope becomes constant [see FIG.4.2(e)]. This behavior at very low fields is difficult to see in the data obtained from the polycrystalline samples. When the magnetic field reaches $H_{C2}$ = 5.8(1) kOe, the $dM/dH$ starts to increase abruptly in a qualitatively similar manner to the polycrystalline $M(H)$ data and the magnetization keeps increasing with magnetic field. The second anomaly, $H_{C2}$ = 5.8(1) kOe corresponds to the critical point $H_C \cong 4.0(3)$ kOe observed in the polycrystalline samples; the difference between these two values could come from slightly different anisotropy values of the two samples measured. Note that there is a small difference in behavior in $M(H)$ between the polycrystalline and single-crystal samples. This difference is likely to be due to the fact that

some defects present in the polycrystalline sample either mask or weaken the transitions seen in the single-crystalline sample. When the external magnetic field is applied perpendicular to the *b* axis in the in-plane direction [see FIG.4.2(f)], the overall behavior of d*M*/d*H* is similar to that of the polycrystalline case and also to the behavior for $H \perp b$, except for the fact that $H_{C1}$ and $H_{C2}$ are too close to be distinguishable in the data for $H \perp b$. Because the overall shape of *M*(*H*) for both crystallographic orientations is similar, the anisotropy seems to be small.

## 4.3.2 Heat capacity measurements

The heat capacity data of both the Y and La samples show a lambda-like sharp peak, which cannot occur for spin-glass transition, at $T_N$ = 0.51(1) and 1.09(4) K, respectively [see FIG.4.3 (a)]. These values are consistent with $T_{LRO}$ obtained from the magnetic susceptibility measurements, which confirms further that both systems have a magnetically ordered ground state at low temperatures. In order to calculate the magnetic entropy change below the transition temperature the phonon contribution was subtracted from the raw data by using a $T^3$ fit with a Debye temperature of 381(1) and 332(2) K for the Y and La samples, respectively [see the inset in FIG.4.3 (a)]. The estimated magnetic entropy [$S_Y$ = 5.83(8) and $S_{La}$ = 5.52(3) J mole$^{-1}$ K$^{-1}$] is comparable to the theoretical entropy for a quantum spin system ($R$ln2 = 5.763 J mole$^{-1}$ K$^{-1}$). In order to examine the field dependence of the phase transition, the field-dependent heat capacity of $CuLa_2Ge_2O_8$ was also measured, which has a higher transition temperature. As shown in FIG.4.3 (b), the peak in the heat capacity gets

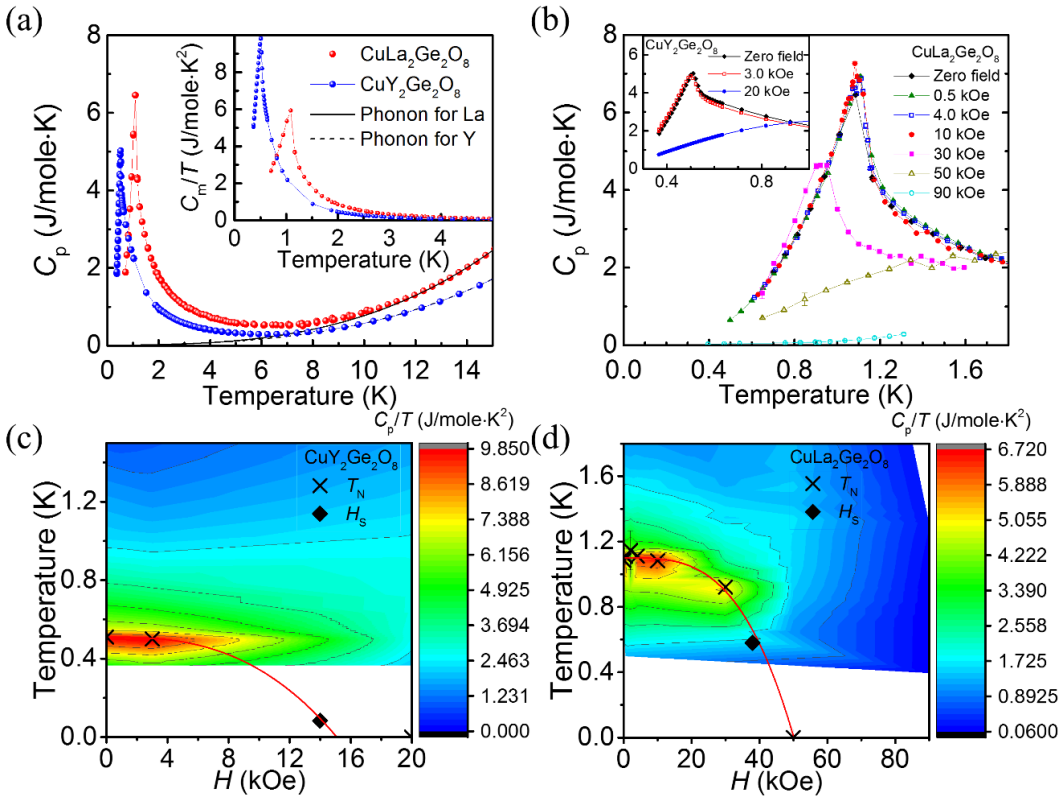


**FIG.4.3 Heat capacity $C_p(T)$ of $CuR_2Ge_2O_8$ ($R$ = Y and La). (a) There is a lambda-like sharp peak in both systems indicating a long-range order. The solid and dashed lines are fits for the $T^3$ law to remove the phonon contribution. The inset shows the temperature dependence of magnetic heat capacity $C_m$ divided by temperature. (b) The field-dependent heat capacity measured data on $CuY_2Ge_2O_8$ (inset) and $CuLa_2Ge_2O_8$, which show the suppression of the long-ranged order with the external magnetic field. (c) and (d) The field-dependent transition points for the Y and La samples, respectively. The black crosses represent the Néel temperatures ($T_N$) at each fields and the black diamond shows the saturation field ($H_S$) from the magnetization data. The solid line is the guide to eyes, indicating the existence of a critical field value, where the magnetic phase transition gets suppressed to the absolute**

**zero temperature.**

substantially suppressed upon the application of magnetic field and eventually becomes lower than the base temperature of the $^3$He set-up. Looking at the phase diagram of FIG.4.3 (d), the transition temperature gets suppressed down to absolute zero temperature at around 50 kOe. The measurements on $CuY_2Ge_2O_8$ show similar behavior [see the inset of FIG.4.3 (b)] but in this case, $T_N$ goes down to zero at around 15 kOe [see the solid line in FIG.4.3(c)].

A passing comment, the observation of the sharp peak in the heat capacity [see FIG.4.3(a)] is at variance with what is expected from the Bonner and Fisher 1D HAFM model [Ref.4.32]. Thus it further supports the view that the magnetic lattice of the Cu ions of $CuR_2Ge_2O_8$ ($R$ = Y and La) is more of a 2D triangular lattice, not a 1D HAFM chain system.

### 4.3.3 DFT calculation

A collaborator Dr. Choong Hyun Kim of IBS-CCES, Korea carried out the electronic structure calculations and the density of states (DOS) using the local density approximation with the Hubbard $U$ (LDA+$U$) density functional theory (DFT) with the software Vienna *ab initio* simulation package (VASP) [Ref.4.25,26]. In order to gain further insights into the ground-state properties and, in particular, the density of states of $CuLa_2Ge_2O_8$, the first-principles density functional theory calculations was performed using a LDA+$U$ method with the Perdew-Burke-Ernzerhof exchange-correlation density functional (PBEsol) form of exchange correlation functional as implemented in the VASP [25,26] program. A local

Hubbard interaction of $U$ = 5 eV is used for Cu 3$d$ electrons, which gives a reasonable value of a band gap of about 2 eV in the density of states (DOS) [see FIG.4.4(a)]. This value is consistent with the blue color of the single crystal samples [see FIG.2.5]. A comparison of the total DOS with the partial DOS from the copper $d$ orbitals in FIG.4.4(b) shows that the main contribution to the bands comes from the copper $d$ orbitals. However, the calculations also demonstrate that the germanium and lanthanum atoms contribute significantly to the DOS of the conduction band while the oxygen atoms contribute more

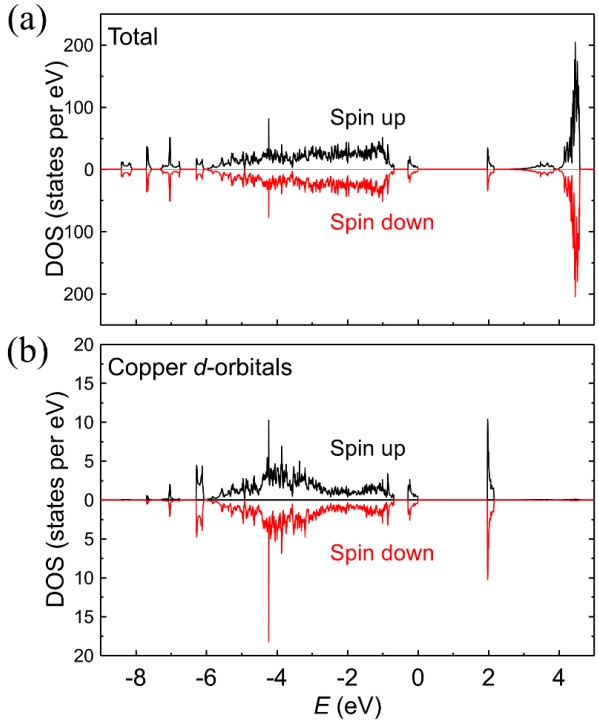


**FIG.4.4 (a) The total density of states calculated using the crystal structure of $CuLa_2Ge_2O_8$ with the Coulomb interaction, $U$ = 5 eV. (b) The partial density of states projected on the copper *d* orbitals.**

to the DOS of the valence band. As a result, the valence band is mainly hybridized oxygen *p*-bands and copper *d* bands. Therefore this system can be considered as a charge-transfer-type insulator like many cuprates [Ref.4.43,44].

## 4.4 Discussion and summary

### 4.4.1 Novel quasi 2D triangular lattice: Cu$R_2Ge_2O_8$

From the crystal structure, magnetic and thermodynamic measurements, and DFT calculation results together, I suggest that the Cu$R_2Ge_2O8$ ($R$ = Y, La) systems are new quantum 2D triangular charge transfer insulator. They exhibit the clear sign of long-range order at low temperatures and magnetic field-induced phase transitions at a low field range. The LRO is probably suppressed due to the combined effects of quantum spins, geometrical frustration, and low-dimensionality. To illustrate the uniqueness of this Cu$R_2Ge_2O_8$ system, I would like to compare the physical properties of Cu$R_2Ge_2O_8$ with those of other known quantum 2D triangular systems in the following paragraphs. There are only few inorganic quantum 2D triangular AF systems which have LRO ground states: $CsCuCl_3$ [Ref.4.45,46], $Cs_2CuBr_4$ (and $Cs_2CuCl_4$) [Ref.4.13,47-50], and $Ba_3CoSb_2O_9$ [Ref.4.7,9,51]. Compared with the three other systems, Cu$R_2Ge_2O_8$ reveals a $CuO_4$ plaquette as a magnetic unit forming a 2D triangular lattice within the *ac* plane with the planes stacking along the *b* axis. In FIG.4.5, the crystal structure of Cu$R_2Ge_2O_8$ is compared with those of the three other compounds. In the *ac* plane of Cu$R_2Ge_2O_8$, the distances between adjacent copper ions are

almost the same ($J_1 \approx J_2 \approx J_3$) and they are shorter by 1.3(1) Å than the interlayer distance ($J_4$). However, unlike the other 2D triangular systems having triangular lattices on a relatively flat plane, in Cu$R_2$Ge$_2$O$_8$ the triangular plane corrugates in a zigzag shape by 146.19(4) degrees along the *a* axis [see FIG.4.1 (a)]. This then is likely to introduce a larger value of Dzyaloshinskii-Moriya interaction, which would then have quite significant effect on the magnetic structure as well as spin dynamics as seen in many other systems such as multiferroic $BiFeO_3$ [Ref.4.52-55]. This corrugated plane and the mirror symmetry perpendicular to the *b* axis suggest two types of the interlayer distances; along the *b* axis the interlayer distance alternates between short and long ones, giving the unique structure for Cu$R_2$Ge$_2$O$_8$. From this lattice structure, the system is expected to have an exotic magnetic lattice with a strong and regular triangular interaction within the *ac* plane. As a result, the average exchange interaction is of an AF type and a weak interlayer interaction is formed along the *b* axis alternatively. It is rather common that 2D triangular AF systems show jump like transitions in their $M(H)$ data: $CsCuCl_3$ [Ref.4.56]; $Cs_2CuBr_4$ and $Ba_3CoSb_2O_9$ [Ref.4.6-11]. An exception is $Cs_2CuCl_4$ that does not show the $1/3M_s$ plateau [Ref.4.57]. In comparison, CuLa$_2$Ge$_2$O$_8$ shows two magnetic field-induced phase transitions at $H_{C1}$ = 0.80(5) kOe and $H_{C2}$ = 5.8(1) kOe [in the Y-based compound, $H_C$ = 2.5(3) kOe]. As the slope between two critical points is constant, the spin state at this region seems to sustain its configuration, similar to the plateau-like behavior of the *uud* state in a regular triangular lattice. However, the fractions of $M(H)$ to $M_s$ are 0.019 and 0.117 at $H_{C1}$ = 0.80(5) kOe and $H_{C2}$ = 5.8(1) kOe, respectively: $M(H_C)/M_s$ = 0.084 for the Y-based compound. To my best knowledge, such small fraction numbers have not been reported

before for a 2D triangular system. To understand further the field-induced phases, neutron diffraction studies at low temperature are necessary.

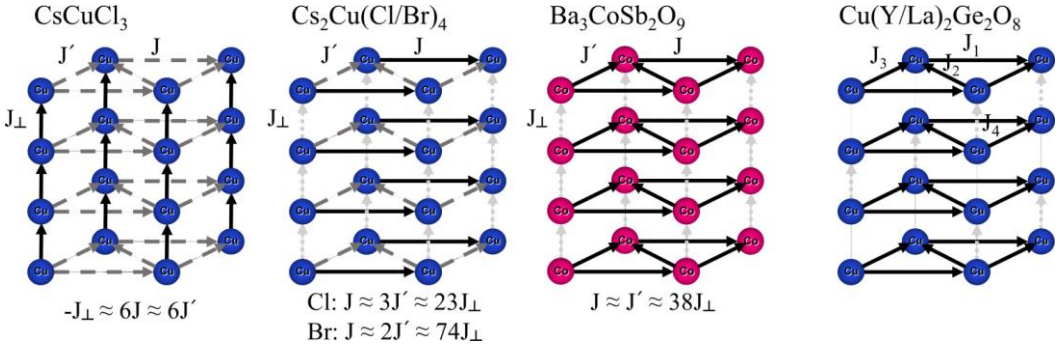


**FIG.4.5 Diagrams of magnetic lattices of selected inorganic quantum 2D triangular systems. The solid arrows depict the strong exchange interactions and the dashed ones depict the weak exchange interactions. $CsCuCl_3$ has strong FM interlayer ($J_\perp$) interactions but weak AF triangular interactions ($J$, $J'$), whereas $Cs_2CuBr_4$ and $Cs_2CuCl_4$ have strong AF chain interactions ($J$) but weak AF inter-chain interactions ($J'$) and weak interlayer interactions ($J_\perp$). $Ba_3CoSb_2O_9$ shows a strong and regular AF triangular interaction ($J$, $J'$) but weak AF interlayer interaction ($J_\perp$). On the other hand, $CuR_2Ge_2O_8$ ($R$ = Y and La) has a strong and regular AF triangular interaction ($J_1 \approx J_2 \approx J_3$) but weak interlayer interaction ($J_4$) formed alternatively along the stacking axis.**

## 4.4.2 Summary

To summarize, extensive studies of the bulk properties of $CuR_2Ge_2O_8$ ($R$ = Y, La) have been carried out including crystal structure analysis, magnetic and thermodynamic measurements, and DFT calculations. These results taken together suggest that the system

should be a charge-transfer type quantum quasi 2D triangular antiferromagnet with clear signs of an antiferromagnetic transition at $T_N$ = 0.51(1) and 1.09(4) K for Y and La, respectively. Remarkably, a field-tuned phase transition arises between this magnetic order and a plateau phase with a small magnetization fraction.

## References

[Ref.4.1] L. Néel, Ann. Phys. (Paris) **5**, 232 (1936).

[Ref.4.2] J. Friedel, Phys. Today **54**, 88 (2001).

[Ref.4.3] Y. Shimizu, K. Miyagawa, K. Kanoda, M. Maesato, and G. Saito, Phys. Rev. Lett. **91**, 107001 (2003).

[Ref.4.4] T. Itou, A. Oyamada, S. Maegawa, M. Tamura, and R. Kato, Phys. Rev. B **77**, 104413 (2008).

[Ref.4.5] M. Fu, T. Imai, T. Han, and Y. Lee, Science **350**, 655 (2015).

[Ref.4.6] T. Ono, H. Tanaka, H. Aruga Katori, F. Ishikawa, H. Mitamura, and T. Goto, Phys. Rev. B **67**, 104431 (2003).

[Ref.4.7] Y. Shirata, H. S. Tanaka, A. Matsuo, and K. Kindo, Phys. Rev. Lett. **108**, 057205 (2012).

[Ref.4.8] N. A. Fortune, S. Hannahs, Y. Yoshida, T. E. Sherline, T. Ono, H. Tanaka, and Y. Takano, Phys. Rev. Lett. **102**, 257201 (2009).

[Ref.4.9] T. Susuki, N. Kurita, T. Tanaka, H. Nojiri, A. Matsuo, K. Kindo, and H. Tanaka, Phys. Rev. Lett. **110**, 267201 (2013).

[Ref.4.10] G. Koutroulakis, T. Zhou, Y. Kamiya, J. D. Thompson, H. D. Zhou, C. D. Batista, and S. E. Brown, Phys. Rev. B **91**, 024410 (2015).

[Ref.4.11] D. Yamamoto, G. Marmorini, and I. Danshita, Phys. Rev. Lett. **114**, 027201 (2015).

[Ref.4.12] T. Nikuni and H. Shiba, J. Phys. Soc. Jpn. **62**, 3268 (1993).

[Ref.4.13] S. A. Zvyagin, D. Kamenskyi,M. Ozerov, J.Wosnitza, M. Ikeda, T. Fujita, M. Hagiwara, A. I. Smirnov, T. A. Soldatov, A. Y. Shapiro, J. Krzystek, R. Hu, H. Ryu, C. Petrovic, and M. E. Zhitomirsky, Phys. Rev. Lett. **112**, 077206 (2014).

[Ref.4.14] R. Coldea, D. A. Tennant, A. M. Tsvelik, and Z. Tylczynski, Phys. Rev. Lett. **86**, 1335 (2001).

[Ref.4.15] A. Honecker, J. Phys.: Condens. Matter **11**, 4697 (1999).

[Ref.4.16] D. Farnell, R. Zinke, J. Schulenburg, and J. Richter, J. Phys.: Condens. Matter **21**, 406002 (2009).

[Ref.4.17] T. Sakai and H. Nakano, Phys. Rev. B **83**, 100405(R) (2011).

[Ref.4.18] K. Yokota, N. Kurita, and H. Tanaka, Phys. Rev. B **90**, 014403 (2014) and references therein.

[Ref.4.19] Y. Wang, Phys. Rev. B **43**, 3786(R) (1991).

[Ref.4.20] H. Kawamura and S. Miyashita, J. Phys. Soc. Jpn. **54**, 4530 (1985)

[Ref.4.21] J. Parkinson and D. Farnell, *An Introduction to Quantum Spin Systems* (Springer, Berlin, 2010).

[Ref.4.22] J. Campá, E. Gutiérrez-Puebla, M. Monge, C. Valero, J. Mira, J. Rivas, C. Cascales, and I. Rasines, J. Solid State Chem. **120**, 254 (1995).

[Ref.4.23] E. Baran and C. Cascales, J. Raman Spectros. **30**, 77 (1999).

[Ref.4.24] J. Rodriguez-Carvajal, Physica B **192**, 55 (1993).

[Ref.4.25] G. Kresse and J. Hafner, Phys. Rev. B **47**, 558(R) (1993).

[Ref.4.26] G. Kresse and D. Joubert, Phys. Rev. B **59**, 1758 (1999).

[Ref.4.27] M. Hase, I. Terasaki, and K. Uchinokura, Phys. Rev. Lett. **70**, 3651 (1993).

[Ref.4.28] N. Motoyama, H. Eisaki, and S. Uchida, Phys. Rev. Lett. **76**, 3212 (1996).

[Ref.4.29] J. Longo and P. Raccah, J. Solid State Chem. **6**, 526 (1973).

[Ref.4.30] N. Kini, E. Kaul, and C. Geibel, J. Phys.: Condens. Matter **18**, 1303 (2006).

[Ref.4.31] R. Feyerherm, S. Abens, D. Günther, T. Ishida, M. Meißner, M. Meschke, T. Nogami, and M. Steiner, J. Phys.: Condens.Matter **12**, 8495 (2000).

[Ref.4.32] J. Bonner and M. Fisher, Phys. Rev. **135**, A640 (1964).

[Ref.4.33] S. Eggert, I. Affleck, and M. Takahashi, Phys. Rev. Lett. **73**, 332 (1994).

[Ref.4.34] A. Klümper and D. C. Johnston, Phys. Rev. Lett. **84**, 4701 (2000).

[Ref.4.35] A. Cuccoli, T. Roscilde, V. Tognetti, R. Vaia, and P. Verrucchi, Phys. Rev. B **67**, 104414 (2003).

[Ref.4.36] M. S. Makivić and H.-Q. Ding, Phys. Rev. B **43**, 3562 (1991).

[Ref.4.37] J.-K. Kim and M. Troyer, Phys. Rev. Lett. **80**, 2705 (1998).

[Ref.4.38] N. Elstner, R. R. P. Singh, and A. P. Young, Phys. Rev. Lett. **71**, 1629 (1993).

[Ref.4.39] A. Ramirez, Annu. Rev. Mater. Sci. **24**, 453 (1994).

[Ref.4.40] S. Blundell, *Magnetism in Condensed Matter* (Oxford University Press, New York, 2001).

[Ref.4.41] K. B. Lyons, P. A. Fleury, J. P. Remeika, A. S. Cooper, and T. J. Negran, Phys. Rev. B **37**, 2353(R) (1988).

[Ref.4.42] U. Schollwöck, J. Richter, D. Farnell, and R. Bishop, *Quantum Magnetism* (Springer, Berlin, 2004).

[Ref.4.43] M. Imada, A. Fujimori, and Y. Tokura, Rev. Mod. Phys. **70**, 1039 (1998).

[Ref.4.44] C. Weber, K. Haule, and G. Kotliar, Nat. Phys. **6**, 574 (2010).

[Ref.4.45] V. P. Plakhty, J. Wosnitza, N. Martin, Y. Marchi, O. P. Smirnov, B. Grenier, and S. V. Gavrilov, Phys. Rev. B **79**, 012410 (2009).

[Ref.4.46] J. Goodenough, *Magnetism and the Chemical Bond* (Interscience, New York, 1963).

[Ref.4.47] N. Krüger, S. Belz, F. Schossau, A. Haghighirad, P. Cong, B. Wolf, S. Gottlieb-Schoenmeyer, F. Ritter, and W. Assmus, Crystal Growth Design **10**, 4456 (2010).

[Ref.4.48] J. McGinnety, J. Am. Chem. Soc. **94**, 8406 (1972).

[Ref.4.49] R. Puget, M. Jannin, R. Perret, L. Godefroy, and G. Godefroy, Ferroelectrics **107**, 229 (1990).

[Ref.4.50] R. Coldea, D. A. Tennant, K. Habicht, P. Smeibidl, C. Wolters, and Z. Tylczynski, Phys. Rev. Lett. **88**, 137203 (2002).

[Ref.4.51] S. Istomin, V. Koutcenko, E. Antipov, F. Lindberg, and G. Svensson, Mater. Res. Bull. **39**, 1013 (2004).

[Ref.4.52] I. Sosnowska, T. Peterlin-Neumaier, and E. Steichele, J. Phys. C **15**, 4835 (1982).

[Ref.4.53] Jaehong Jeong, E. A. Goremychkin, T. Guidi, K. Nakajima, Gun Sang Jeon, Shin-Ae Kim, S. Furukawa, Yong Baek Kim, Seongsu Lee, V. Kiryukhin, S-W. Cheong, and Je-Geun Park, Phys. Rev. Lett. **108**, 077202 (2012); **113**, 107202 (2014).

[Ref.4.54] M. Matsuda, R. S. Fishman, T. Hong, C. H. Lee, T. Ushiyama, Y. Yanagisawa, Y. Tomioka, and T. Ito, Phys. Rev. Lett. **109**, 067205 (2012).

[Ref.4.55] For review, see Je-Geun Park, Manh Duc Le, Jaehong Jeong, and Sanghyun Lee, J. Phys.: Condens. Matter **26**, 433202 (2014).

[Ref.4.56] J. Shibuya, M. Akaki, Y. Kohama, A. Miyake, M. Tokunaga, and H. Tanaka, J.

Phys.: Conf. Ser. **568**, 042030 (2014).

[Ref.4.57] Y. Tokiwa, T. Radu, R. Coldea, H. Wilhelm, Z. Tylczynski, and F. Steglich, Phys. Rev. B **73**, 134414 (2006).

# Chapter 5
# Outlook and Summary

## 5.1 Outlook

The study on $CuAl_2O_4$ shows that in the specific case of the large $U$ and localized spins, leading to a narrow bandwidth, the small SOC which is even less than 0.1 eV actually can change the whole nature of the ground state. This study implies that the small SOC in 3$d$ compounds should not be ignored and it can further suggest the emergence of other $J_{eff}$-multiplets. For example, an A-site spinel (or normal spinel $(A_{1-x}B_x)_{tetra}(B_{2-x}A_x)_{octa}X_4$, where X is a chalcogen, which has the inversion x less than 0.5) which has $Ni^{2+}$ ions in its A-site could have a $J_{eff} = 0$ state as a ground state and a B-site spinel (or inverse spinel, which has the x>0.5) could have $J_{eff} = 3/2$ states for B = $Ti^{3+}$.

For the study on quasi 2D triangular HAF Cu$R_2Ge_2O_8$ ($R$ = Y, La), novel magnetic transitions are found in the La compound at low magnetic fields of $H_{C1}$ = 0.80(5) kOe and $H_{C2}$ = 5.8(1) kOe, which make a plateau like shape in the $M(H)$ curve. As many other 2D triangular HAFs show unique magnetic transitions induced by their characteristic lattice structure, the novel interlayer interactions expected from the structure can lead this phenomenon. Neutron scattering experiments would be an appropriate tool to identify the

magnetic structure of the system and the role of the interlayer couplings making the magnetic phases in 2D triangular HAFs. This study will widen the understandings on the magnetic phases in 2D triangular lattice with interlayer couplings.

## 5.2 Summary

To find exotic emergent phenomena induced by quantum fluctuations, I explored two new cuprate systems: $CuAl_2O_4$ and $CuR_2Ge_2O_8$ ($R$ = Y, La). For studies on a $CuAl_2O$ single-crystal sample, via single-crystal XRD, resistance measurements, and Cu K-edge and L-edge XAS techniques, the ground state of the system is identified to be the Mott insulating spin-orbital entangled $J_{eff}$ = 1/2 state. The single-crystal XRD and the K-edge spectrum show the lattice structure of $CuAl_2O_4$ is cubic without any structural distortions. The emergence of the $J_{eff}$ = 1/2 state, being composed of equal contributions of the *xy*, *yz*, and *zx* orbitals is a possible answer for the cubic symmetry. The advent of the $J_{eff}$ = 1/2 is further verified by the L-edge XAS. The spectra show the main peak (α) with the shoulder peak (β) in the $L_3$-edge but only one peak (β) at the $L_2$-edge, which gives extraordinary larger BR of 6.3(1) than that of the conventional cuprates. Moreover, the magnetic properties measurements show the moment of the spin-orbital $J_{eff}$ = 1/2 state is highly frustrated without long-range order. With previous studies on the glassy nature of $CuAl_2O_4$, the ground state of this system is a novel 'spin-orbital glass' state.

The studies on the bulk properties of $CuR_2Ge_2O_8$ ($R$=Y, La) are done including crystal structure analysis, magnetic and thermodynamic measurements, and DFT calculations.

These results taken together suggest that the system should be a charge-transfer type quantum quasi 2D triangular antiferromagnet rather than the 1D chain speculated in the previous research. These systems show clear signs of an antiferromagnetic transition at $T_N$ = 0.51(1) and 1.09(4) K for Y and La, respectively. Remarkably, field-tuned phase transitions arise, making a plateau phase with small magnetization fractions. This phenomenon seems to originate from the interplay of strong quantum fluctuations and novel interlayer interactions expected from the buckled layer.

From the studies on quantum magnetism on the novel cuprate compounds: $CuAl_2O_4$ and $Cu\mathit{R}_2Ge_2O_8$, I found a novel ground state, 'spin-orbital glass' based on a significant effect of SOC and quantum fluctuations strengthened by frustration, and novel magnetic phase transition which is related to the interactions of interlayer couplings and strong quantum fluctuations.

# Appendix
# Electric Dipole Transitions

The Hamiltonian for the motion of a particle of mass *m* and charge *e* in an electromagnetic field described by the potentials **A** with an additional potential energy *V*, is following [Ref.A1]

$$H = \frac{1}{2m}\left(\boldsymbol{p} - \frac{e}{c}\boldsymbol{A}\cdot e^{i\boldsymbol{q}\cdot\boldsymbol{r}}\right)^2 + V(\boldsymbol{r})$$

In the case of transverse wave without an external magnetic field,

$$H \cong \left(\frac{\boldsymbol{p}^2}{2m} + V\right) - \frac{e}{mc}e^{i\boldsymbol{q}\cdot\boldsymbol{r}}\boldsymbol{A}\cdot\boldsymbol{p} + O(A^2) \cong H_0 + H_1,$$

where

$$H_0 = \left(\frac{\boldsymbol{p}^2}{2m} + V\right) \;\; and \;\; H_1 = -\frac{e}{mc}e^{i\boldsymbol{q}\cdot\boldsymbol{r}}\boldsymbol{A}\cdot\boldsymbol{p}$$

According to Fermi's golden rule the matrix element of $H_1$ is a transition amplitude.

Moreover, for the constant **A**,

$$e^{i\boldsymbol{q}\cdot\boldsymbol{r}}\boldsymbol{A}\cdot\boldsymbol{p} = (\boldsymbol{A}\cdot\boldsymbol{p}) + \frac{i}{2}(\boldsymbol{A}\times\boldsymbol{q})\cdot(\boldsymbol{r}\times\boldsymbol{p}) - \frac{i}{2}\{(\boldsymbol{q}\cdot\boldsymbol{r})(\boldsymbol{A}\cdot\boldsymbol{p}) + (\boldsymbol{A}\cdot\boldsymbol{r})(\boldsymbol{q}\cdot\boldsymbol{p})\}\ldots$$

The first and second terms mean *k*=1 an irreducible tensor operator for electric dipole transitions and magnetic dipole transitions, respectively, and the third one indicates *k*=2 electric quadrupole transitions.

Therefore, the transition amplitude for electric dipole transitions is

$$\langle j_f, m_f | T(k,q) | j_i, m_i \rangle,$$

where $|j_f, m_f\rangle$ and $|j_i, m_i\rangle$ are final and initial states, and $T(k, q)$ is a reducible tensor operator. Then,

$$\boldsymbol{A} \cdot \langle j_f, m_f | \boldsymbol{p} | j_i, m_i \rangle = \left( \frac{1}{m}\boldsymbol{p} = \frac{d}{dt}\boldsymbol{r} = \frac{1}{i\hbar}[\boldsymbol{r}, H_0] \right) = \boldsymbol{A} \cdot \langle j_f, m_f | [\boldsymbol{r}, H_0] | j_i, m_i \rangle$$
$$= -(E_f - E_i)\boldsymbol{A} \cdot \langle j_f, m_f | \boldsymbol{r} | j_i, m_i \rangle,$$

where $E_i$ and $E_f$ are energy eigenvalues of initial and finial states, respectively.

Therefore, $T = T(k=1, q=0,\pm1)$ ($x = \frac{1}{2}\{T(1, -1) - T(1, 1)\}$, $y = \frac{i}{2}\{T(1, -1) + T(1, 1)\}$, $z = T(1, 0)$, whereas $T = T(k=1, q=\pm1)$ for circular polarizations). Then, the transition rate, or the intensity of the transitions is

$$\left| \langle j_f, m_f | \boldsymbol{r} | j_i, m_i \rangle \right|^2$$

ignoring other constants, which are the same in transition processes described here.

In case of $j_{\text{eff}} = 1/2$ states, the initial states of core electrons are following

$$2p^{1/2} = |j_i = 1/2, m_i = \pm 1/2\rangle \text{ and } 2p^{3/2} = |j_i = 3/2, m_i = \pm 1/2, \pm 3/2\rangle$$

and the final state is $j_{\text{eff}} = 1/2$ states [Ref.A2]

$$|j_{\text{eff}} = 1/2, m_{j_{\text{eff}}} = 1/2\rangle = \frac{1}{\sqrt{3}}(|yz, \sigma\rangle - i|zx, \sigma\rangle - |xy, -\sigma\rangle)$$
$$|j_{\text{eff}} = 1/2, m_{j_{\text{eff}}} = -1/2\rangle = \frac{1}{\sqrt{3}}(|yz, -\sigma\rangle + i|zx, -\sigma\rangle + |xy, \sigma\rangle)$$

where $|\pm\sigma\rangle$ is spinor of $|s = 1/2, m_s = \pm 1/2\rangle$ and the slater orbitals can be written as following [Ref.A3]

$$t_{2g}\begin{cases}|xy\rangle = \dfrac{-i}{\sqrt{2}}(|l=2,m_l=2\rangle - |l=2,m_l=-2\rangle)\\ |zx\rangle = \dfrac{-1}{\sqrt{2}}(|l=2,m_l=1\rangle - |l=2,m_l=-1\rangle\\ |yz\rangle = \dfrac{i}{\sqrt{2}}(|l=2,m_l=1\rangle + |l=2,m_l=-1\rangle\end{cases}$$

$$e_g\begin{cases}|z^2\rangle = |l=2,m_l=0\rangle\\ |x^2{-}y^2\rangle = \dfrac{1}{\sqrt{2}}(|l=2,m_l=2\rangle + |l=2,m_l=-2\rangle)\end{cases}$$

Then, the transition amplitude for $L_2$-edge is

$$\left\langle j_{eff}=1/2, m_{j_{eff}}=\pm 1/2\middle|\boldsymbol{r}\middle|j_i=1/2, m_i=\pm 1/2\right\rangle$$

and the transition amplitude for $L_3$-edge is

$$\left\langle j_{eff}=1/2, m_{j_{eff}}=\pm 1/2\middle|\boldsymbol{r}\middle|j_i=3/2, m_i=\pm 1/2, \pm 3/2\right\rangle$$

According to Wigner-Eckart theorem

$$|j,m_j\rangle = \sum_{q,m_i} T(k,q)|j_i,m_i\rangle\langle q,m_i|j,m_j\rangle$$

where $\langle q,m_i|j,m_j\rangle$ is Clebsch-Gordan coefficient. Several Clebsch-Gordan tables which will be used for calculating the transition amplitude are following

$j_1$=1, $j_2$=1/2

| $m_1$ $m_2$ \ $j$ $m_j$ | 3/2 3/2 | 3/2 1/2 | 1/2 1/2 | 3/2 -1/2 | 1/2 -1/2 | 3/2 -3/2 |
|---|---|---|---|---|---|---|
| 1 1/2 | 1 | | | | | |
| 1 -1/2 | | $\sqrt{1/3}$ | $\sqrt{2/3}$ | | | |
| 0 1/2 | | $\sqrt{2/3}$ | $-\sqrt{1/3}$ | | | |
| 0 -1/2 | | | | $\sqrt{2/3}$ | $\sqrt{1/3}$ | |
| -1 1/2 | | | | $\sqrt{1/3}$ | $-\sqrt{2/3}$ | |
| -1 -1/2 | | | | | | 1 |

$j_1$=2, $j_2$=1/2

| $m_1$ $m_2$ \ $j$ $m_j$ | 5/2 5/2 | 5/2 3/2 | 3/2 3/2 | 5/2 1/2 | 3/2 1/2 | 5/2 -1/2 | 3/2 -1/2 | 5/2 -3/2 | 3/2 -3/2 | 5/2 -5/2 |
|---|---|---|---|---|---|---|---|---|---|---|
| 2 1/2 | 1 | | | | | | | | | |
| 2 -1/2 | | $\sqrt{1/5}$ | $\sqrt{4/5}$ | | | | | | | |
| 1 1/2 | | $\sqrt{4/5}$ | $-\sqrt{1/5}$ | | | | | | | |
| 1 -1/2 | | | | $\sqrt{2/5}$ | $\sqrt{3/5}$ | | | | | |
| 0 1/2 | | | | $\sqrt{3/5}$ | $-\sqrt{2/5}$ | | | | | |
| 0 -1/2 | | | | | | $\sqrt{3/5}$ | $\sqrt{2/5}$ | | | |
| -1 1/2 | | | | | | $\sqrt{2/5}$ | $-\sqrt{3/5}$ | | | |
| -1 -1/2 | | | | | | | | $\sqrt{4/5}$ | $\sqrt{1/5}$ | |
| -2 1/2 | | | | | | | | $\sqrt{1/5}$ | $-\sqrt{4/5}$ | |
| -2 -1/2 | | | | | | | | | | 1 |

$j_1$=2, $j_2$=1/2

| $j$ / $m_j$ / $m_1$ $m_2$ | 5/2 5/2 | 5/2 3/2 | 3/2 3/2 | 5/2 1/2 | 3/2 1/2 | 5/2 -1/2 | 3/2 -1/2 | 5/2 -3/2 | 3/2 -3/2 | 5/2 -5/2 |
|---|---|---|---|---|---|---|---|---|---|---|
| 2 1/2 | 1 | | | | | | | | | |
| 2 -1/2 | | $\sqrt{1/5}$ | $\sqrt{4/5}$ | | | | | | | |
| 1 1/2 | | $\sqrt{4/5}$ | $-\sqrt{1/5}$ | | | | | | | |
| 1 -1/2 | | | | $\sqrt{2/5}$ | $\sqrt{3/5}$ | | | | | |
| 0 1/2 | | | | $\sqrt{3/5}$ | $-\sqrt{2/5}$ | | | | | |
| 0 -1/2 | | | | | | $\sqrt{3/5}$ | $\sqrt{2/5}$ | | | |
| -1 1/2 | | | | | | $\sqrt{2/5}$ | $-\sqrt{3/5}$ | | | |
| -1 -1/2 | | | | | | | | $\sqrt{4/5}$ | $\sqrt{1/5}$ | |
| -2 1/2 | | | | | | | | $\sqrt{1/5}$ | $-\sqrt{4/5}$ | |
| -2 -1/2 | | | | | | | | | | 1 |

$j_1$=3/2, $j_2$=1

| $j$ / $m_j$ / $m_1$ $m_2$ | 5/2<br>5/2 | 5/2<br>3/2 | 3/2<br>3/2 | 5/2<br>1/2 | 3/2<br>1/2 | 1/2<br>1/2 | 5/2<br>-1/2 | 3/2<br>-1/2 | 1/2<br>-1/2 | 5/2<br>-3/2 | 3/2<br>-3/2 | 5/2<br>-5/2 |
|---|---|---|---|---|---|---|---|---|---|---|---|---|
| $\frac{3}{2}$ 1 | 1 | | | | | | | | | | | |
| $\frac{3}{2}$ 0 | | $\sqrt{2/5}$ | $\sqrt{3/5}$ | | | | | | | | | |
| $\frac{1}{2}$ 1 | | $\sqrt{3/5}$ | $-\sqrt{2/5}$ | | | | | | | | | |
| $\frac{3}{2}$ -1 | | | | $\sqrt{1/10}$ | $\sqrt{2/5}$ | $\sqrt{1/2}$ | | | | | | |
| $\frac{1}{2}$ 0 | | | | $\sqrt{3/5}$ | $\sqrt{1/15}$ | $-\sqrt{1/3}$ | | | | | | |
| $\frac{-1}{2}$ 1 | | | | $\sqrt{3/10}$ | $-\sqrt{8/15}$ | $\sqrt{1/6}$ | | | | | | |
| $\frac{1}{2}$ -1 | | | | | | | $\sqrt{3/10}$ | $\sqrt{8/15}$ | $\sqrt{1/6}$ | | | |
| $\frac{-1}{2}$ 0 | | | | | | | $\sqrt{3/5}$ | $-\sqrt{1/15}$ | $-\sqrt{1/3}$ | | | |
| $\frac{-3}{2}$ 1 | | | | | | | $\sqrt{1/10}$ | $-\sqrt{2/5}$ | $\sqrt{1/2}$ | | | |
| $\frac{-1}{2}$ -1 | | | | | | | | | | $\sqrt{3/5}$ | $\sqrt{2/5}$ | |
| $\frac{-3}{2}$ 0 | | | | | | | | | | $\sqrt{2/5}$ | $-\sqrt{3/5}$ | |
| $\frac{-3}{2}$ -1 | | | | | | | | | | | | 1 |

Therefore,

$$T(1,0)|j_i = 1/2, m_i = \pm 1/2\rangle$$

$$= \begin{cases} N(\sqrt{2/3}\,|j = 3/2, m_j = 1/2\rangle - \sqrt{1/3}\,|j = 1/2, m_j = 1/2\rangle) \\ N(\sqrt{2/3}\,|j = 3/2, m_j = -1/2\rangle + \sqrt{1/3}\,|j = 1/2, m_j = -1/2\rangle) \end{cases}$$

$T(1,0)|j_i = 3/2, m_i = \pm 3/2, \pm 1/2\rangle$

$$= \begin{cases} N(\sqrt{2/5}\,|j = 5/2, m_j = 3/2\rangle + \sqrt{3/5}\,|j = 3/2, m_j = 3/2\rangle) \\ N\left(\sqrt{2/5}\,|j = 5/2, m_j = -3/2\rangle - \sqrt{3/5}\,|j = 3/2, m_j = -3/2\rangle\right) \\ N\left(\sqrt{3/5}\,|j = 5/2, m_j = 1/2\rangle + \sqrt{1/15}\,|j = 3/2, m_j = 1/2\rangle - \sqrt{1/3}\,|j = 1/2, m_j = 1/2\rangle\right) \\ N(\sqrt{3/5}\,|j = 5/2, m_j = -1/2\rangle - \sqrt{1/15}\,|j = 3/2, m_j = -1/2\rangle - \sqrt{1/3}\,|j = 1/2, m_j = -1/2\rangle) \end{cases}$$

$T(1,-1)|j_i = 1/2, m_i = \pm 1/2\rangle$

$$= \begin{cases} N(\sqrt{1/3}\,|j = 3/2, m_j = -1/2\rangle - \sqrt{2/3}\,|j = 1/2, m_j = -1/2\rangle) \\ N(|j = 3/2, m_j = -3/2\rangle) \end{cases}$$

$T(1,-1)|j_i = 3/2, m_i = \pm 3/2, \pm 1/2\rangle$

$$= \begin{cases} N\left(\sqrt{1/10}\,|j = 5/2, m_j = 1/2\rangle + \sqrt{2/5}\,|j = 3/2, m_j = 1/2\rangle + \sqrt{1/2}\,|j = 1/2, m_j = 1/2\rangle\right) \\ N(|j = 5/2, m_j = -5/2\rangle) \\ N\left(\sqrt{3/10}\,|j = 5/2, m_j = -1/2\rangle + \sqrt{8/15}\,|j = 3/2, m_j = -1/2\rangle + \sqrt{1/6}\,|j = 1/2, m_j = -1/2\rangle\right) \\ N\left(\sqrt{3/5}\,|j = 5/2, m_j = -3/2\rangle + \sqrt{2/5}\,|j = 3/2, m_j = -3/2\rangle\right) \end{cases}$$

$T(1,1)|j_i = 1/2, m_i = \pm 1/2\rangle$

$$= \begin{cases} N(|j = 3/2, m_j = 3/2\rangle) \\ N(\sqrt{1/3}\,|j = 3/2, m_j = 1/2\rangle + \sqrt{2/3}\,|j = 1/2, m_j = 1/2\rangle) \end{cases}$$

$T(1,1)|j_i = 3/2, m_i = \pm 3/2, \pm 1/2\rangle$

$$= \begin{cases} N(|j = 5/2, m_j = 5/2\rangle) \\ N(\sqrt{1/10}\,|j = 5/2, m_j = -1/2\rangle - \sqrt{2/5}\,|j = 3/2, m_j = -1/2\rangle + \sqrt{1/2}\,|j = 1/2, m_j = -1/2\rangle) \\ N(\sqrt{3/5}\,|j = 5/2, m_j = 3/2\rangle - \sqrt{2/5}\,|j = 3/2, m_j = 3/2\rangle) \\ N(\sqrt{3/10}\,|j = 5/2, m_j = 1/2\rangle - \sqrt{8/15}\,|j = 3/2, m_j = 1/2\rangle + \sqrt{1/6}\,|j = 1/2, m_j = 1/2\rangle) \end{cases}$$

where N is a normalization factor.

In a similar way,

$$|xy\rangle\otimes|\pm\sigma\rangle$$

$$=\begin{cases}-i(\sqrt{1/2}\,|j=5/2,m_j=5/2\rangle-\sqrt{1/10}\,|j=5/2,m_j=-3/2\rangle+\sqrt{2/5}\,|j=3/2,m_j=-3/2\rangle)\\ -i(\sqrt{1/10}\,|j=5/2,m_j=3/2\rangle+\sqrt{2/5}\,|j=3/2,m_j=3/2\rangle-\sqrt{1/2}\,|j=5/2,m_j=-5/2\rangle)\end{cases}$$

$$|zx\rangle\otimes|\pm\sigma\rangle=\begin{cases}-\sqrt{2/5}\,|j=5/2,m_j=3/2\rangle+\sqrt{1/10}\,|j=3/2,m_j=3/2\rangle+\sqrt{1/5}\,|j=5/2,m_j=-1/2\rangle\\ -\sqrt{3/10}\,|j=3/2,m_j=-1/2\rangle\\ -\sqrt{1/5}\,|j=5/2,m_j=1/2\rangle-\sqrt{3/10}\,|j=3/2,m_j=1/2\rangle+\sqrt{2/5}\,|j=5/2,m_j=-3/2\rangle\\ +\sqrt{1/10}\,|j=3/2,m_j=-3/2\rangle\end{cases}$$

$$|yz\rangle\otimes|\pm\sigma\rangle=\begin{cases}i(\sqrt{2/5}\,|j=5/2,m_j=3/2\rangle-\sqrt{1/10}\,|j=3/2,m_j=3/2\rangle+\sqrt{1/5}\,|j=5/2,m_j=-1/2\rangle\\ -\sqrt{3/10}\,|j=3/2,m_j=-1/2\rangle)\\ i(\sqrt{1/5}\,|j=5/2,m_j=1/2\rangle+\sqrt{3/10}\,|j=3/2,m_j=1/2\rangle+\sqrt{2/5}\,|j=5/2,m_j=-3/2\rangle\\ +\sqrt{1/10}\,|j=3/2,m_j=-3/2\rangle)\end{cases}$$

Then,

$$\langle xy,\pm\sigma|T(1,0)|j_i=1/2,m_i=\pm1/2\rangle=\begin{cases}++:0\\ +-:0\\ -+:0\\ --:0\end{cases}$$

$$\langle zx,\pm\sigma|T(1,0)|j_i=1/2,m_i=\pm1/2\rangle=\begin{cases}++:0\\ +-:(-N/\sqrt{5})\\ -+:(-N/\sqrt{5})\\ --:0\end{cases}$$

$$\langle yz,\pm\sigma|T(1,0)|j_i=1/2,m_i=\pm1/2\rangle=\begin{cases}++:0\\ +-:(-iN/\sqrt{5})\\ -+:(iN/\sqrt{5})\\ --:0\end{cases}$$

$$\langle xy, \pm\sigma|T(1,0)|j_i = 3/2, m_i = \pm 3/2\rangle = \begin{cases} ++: 0 \\ +-: (iN(1+\sqrt{6})/5) \\ -+: (-iN(1+\sqrt{6})/5) \\ --: 0 \end{cases}$$

$$\langle xy, \pm\sigma|T(1,0)|j_i = 3/2, m_i = \pm 1/2\rangle = \begin{cases} ++: 0 \\ +-: 0 \\ -+: 0 \\ --: 0 \end{cases}$$

$$\langle zx, \pm\sigma|T(1,0)|j_i = 3/2, m_i = \pm 3/2\rangle = \begin{cases} ++: (-N(2/5-\sqrt{3/50})) \\ +-: 0 \\ -+: 0 \\ --: (N(2/5-\sqrt{3/50})) \end{cases}$$

$$\langle zx, \pm\sigma|T(1,0)|j_i = 3/2, m_i = \pm 1/2\rangle = \begin{cases} ++: 0 \\ +-: (N(\sqrt{3}/5+\sqrt{1/50})) \\ -+: (-N(\sqrt{3}/5+\sqrt{1/50})) \\ --: 0 \end{cases}$$

$$\langle yz, \pm\sigma|T(1,0)|j_i = 3/2, m_i = \pm 3/2\rangle = \begin{cases} ++: (iN(2/5-\sqrt{3/50})) \\ +-: 0 \\ -+: 0 \\ --: (iN(2/5-\sqrt{3/50})) \end{cases}$$

$$\langle yz, \pm\sigma|T(1,0)|j_i = 3/2, m_i = \pm 1/2\rangle = \begin{cases} ++: 0 \\ +-: (iN(\sqrt{3}/5+\sqrt{1/50})) \\ -+: (iN(\sqrt{3}/5+\sqrt{1/50})) \\ --: 0 \end{cases}$$

$$\langle xy, \pm\sigma|T(1,-1)|j_i = 1/2, m_i = \pm 1/2\rangle = \begin{cases} ++: 0 \\ +-: (-iN\sqrt{2/5}) \\ -+: 0 \\ --: 0 \end{cases}$$

$$\langle zx, \pm\sigma|T(1,-1)|j_i = 1/2, m_i = \pm 1/2\rangle = \begin{cases} ++: (-N/\sqrt{10}) \\ +-: 0 \\ -+: 0 \\ --: (N/\sqrt{10}) \end{cases}$$

$$\langle yz, \pm\sigma|T(1,-1)|j_i = 1/2, m_i = \pm 1/2\rangle = \begin{cases} ++: (-iN/\sqrt{10}) \\ +-: 0 \\ -+: 0 \\ --: (iN/\sqrt{10}) \end{cases}$$

$$\langle xy, \pm\sigma|T(1,-1)|j_i = 3/2, m_i = \pm 3/2\rangle = \begin{cases} ++: 0 \\ +-: 0 \\ -+: 0 \\ --: (iN/\sqrt{2}) \end{cases}$$

$$\langle xy, \pm\sigma|T(1,-1)|j_i = 3/2, m_i = \pm 1/2\rangle = \begin{cases} ++: 0 \\ +-: (iN(\sqrt{3/50} - 2/5)) \\ -+: 0 \\ --: 0 \end{cases}$$

$$\langle zx, \pm\sigma|T(1,-1)|j_i = 3/2, m_i = \pm 3/2\rangle = \begin{cases} ++: 0 \\ +-: 0 \\ -+: (-N(\sqrt{1/50} + \sqrt{3}/5)) \\ --: 0 \end{cases}$$

$$\langle zx, \pm\sigma|T(1,-1)|j_i = 3/2, m_i = \pm 1/2\rangle = \begin{cases} ++: (N(\sqrt{3/50} - 2/5)) \\ +-: 0 \\ -+: 0 \\ --: (N(\sqrt{6}/5 + 1/5)) \end{cases}$$

$$\langle yz, \pm\sigma|T(1,-1)|j_i = 3/2, m_i = \pm 3/2\rangle = \begin{cases} ++: 0 \\ +-: 0 \\ -+: (Ni(\sqrt{1/50} + \sqrt{3}/5)) \\ --: 0 \end{cases}$$

$$\langle yz, \pm\sigma|T(1,-1)|j_i = 3/2, m_i = \pm 1/2\rangle = \begin{cases} ++: (iN(\sqrt{3/50} - 2/5)) \\ +-: 0 \\ -+: 0 \\ --: (iN(\sqrt{6}/5 + 1/5)) \end{cases}$$

$$\langle xy, \pm\sigma|T(1,1)|j_i = 1/2, m_i = \pm 1/2\rangle = \begin{cases} ++: 0 \\ +-: 0 \\ -+: (-iN(\sqrt{2/5})) \\ --: 0 \end{cases}$$

$$\langle zx, \pm\sigma|T(1,1)|j_i = 1/2, m_i = \pm 1/2\rangle = \begin{cases} ++: (N/\sqrt{10}) \\ +-: 0 \\ -+: 0 \\ --: (-N/\sqrt{10}) \end{cases}$$

$$\langle yz, \pm\sigma|T(1,1)|j_i = 1/2, m_i = \pm 1/2\rangle = \begin{cases} ++: (-iN/\sqrt{10}) \\ +-: 0 \\ -+: - \\ --: (iN/\sqrt{10}) \end{cases}$$

$$\langle xy, \pm\sigma|T(1,1)|j_i = 3/2, m_i = \pm 3/2\rangle = \begin{cases} ++: (-iN/\sqrt{2}) \\ +-: 0 \\ -+: 0 \\ --: 0 \end{cases}$$

$$\langle xy, \pm\sigma|T(1,1)|j_i = 3/2, m_i = \pm 1/2\rangle = \begin{cases} ++: 0 \\ +-: 0 \\ -+: (-iN(\sqrt{3/50} - 2/5)) \\ --: 0 \end{cases}$$

$$\langle zx, \pm\sigma|T(1,1)|j_i = 3/2, m_i = \pm 3/2\rangle = \begin{cases} ++: 0 \\ +-: (iN(\sqrt{1/50} + \sqrt{3}/5)) \\ -+: 0 \\ --: 0 \end{cases}$$

$$\langle zx, \pm\sigma|T(1,1)|j_i = 3/2, m_i = \pm 1/2\rangle = \begin{cases} ++: (-N(1+\sqrt{6})/5) \\ +-: 0 \\ -+: 0 \\ --: (N(2/5 - \sqrt{3/50})) \end{cases}$$

$$\langle yz, \pm\sigma|T(1,1)|j_i = 3/2, m_i = \pm 3/2\rangle = \begin{cases} ++: 0 \\ +-: (iN(\sqrt{1/50} + \sqrt{3}/5)) \\ -+: 0 \\ --: 0 \end{cases}$$

$$\langle yz, \pm\sigma|T(1,1)|j_i = 3/2, m_i = \pm 1/2\rangle = \begin{cases} ++: (iN(1+\sqrt{6})/5) \\ +-: 0 \\ -+: 0 \\ --: (iN(\sqrt{3/50} - 2/5)) \end{cases}$$

In case that the incident beam is linearly polarized along $x = \frac{1}{2}\{T(1, -1) - T(1, 1)\}$,

$$\langle xy, \pm\sigma|x|j_i = 1/2, m_i = \pm 1/2\rangle = \begin{cases} ++: 0 \\ +-: (-iN/\sqrt{10}) \\ -+: (iN/\sqrt{10}) \\ --: 0 \end{cases}$$

$$\langle zx, \pm\sigma|x|j_i = 1/2, m_i = \pm 1/2\rangle = \begin{cases} ++: (-N/\sqrt{10}) \\ +-: 0 \\ -+: 0 \\ --: (N/\sqrt{10}) \end{cases}$$

$$\langle yz, \pm\sigma|x|j_i = 1/2, m_i = \pm 1/2\rangle = \begin{cases} ++: 0 \\ +-: 0 \\ -+: 0 \\ --: 0 \end{cases}$$

$$\langle xy, \pm\sigma|x|j_i = 3/2, m_i = \pm 3/2\rangle = \begin{cases} ++: (iN/\sqrt{8}) \\ +-: 0 \\ -+: 0 \\ --: (iN/\sqrt{8}) \end{cases}$$

$$\langle xy, \pm\sigma|x|j_i = 3/2, m_i = \pm 1/2\rangle = \begin{cases} ++: 0 \\ +-: (iN(\sqrt{3/200} - 1/5)) \\ -+: (iN(\sqrt{3/200} - 1/5)) \\ --: 0 \end{cases}$$

$$\langle zx, \pm\sigma|x|j_i = 3/2, m_i = \pm 3/2\rangle = \begin{cases} ++: 0 \\ +-: (-N(\sqrt{1/200} + \sqrt{3}/10)) \\ -+: (-N(\sqrt{1/200} + \sqrt{3}/10)) \\ --: 0 \end{cases}$$

$$\langle zx, \pm\sigma|x|j_i = 3/2, m_i = \pm 1/2\rangle = \begin{cases} ++: (N(\sqrt{27/200} - 1/10)) \\ +-: 0 \\ -+: 0 \\ --: (N(\sqrt{27/200} - 1/10)) \end{cases}$$

$$\langle yz, \pm\sigma|x|j_i = 3/2, m_i = \pm 3/2\rangle = \begin{cases} ++: 0 \\ +-: (-iN(\sqrt{1/200} + \sqrt{3}/10)) \\ -+: (iN(\sqrt{1/200} + \sqrt{3}/10)) \\ --: 0 \end{cases}$$

$$\langle yz, \pm\sigma|x|j_i = 3/2, m_i = \pm 1/2\rangle = \begin{cases} ++: (-iN(\sqrt{3/200} + 3/10)) \\ +-: 0 \\ -+: 0 \\ --: (iN(\sqrt{3/200} + 3/10)) \end{cases}$$

and the transition amplitude of $L_2$-edge is

$$\begin{aligned} &\langle j_{eff} = 1/2, m_{jeff} = 1/2|x|j_i = 1/2, m_i = \pm 1/2\rangle \\ &\quad = \sqrt{1/3}\,(\langle yz, \sigma| - i\langle zx, \sigma| - \langle xy, -\sigma|)x|j_i = 1/2, m_i = \pm 1/2\rangle = 0 \\ &\langle j_{eff} = 1/2, m_{jeff} = -1/2|x|j_i = 1/2, m_i = \pm 1/2\rangle \\ &\quad = \sqrt{1/3}\,(\langle yz, -\sigma| + i\langle zx, -\sigma| + \langle xy, \sigma|)x|j_i = 1/2, m_i = \pm 1/2\rangle = 0 \end{aligned}$$

Finally, the transition rate of $L_2$-edge is zero.

and the transition amplitude of $L_3$-edge is

$$\langle j_{eff} = 1/2, m_{jeff} = 1/2 | x | j_i = 1/2, m_i = \pm 3/2 \rangle$$
$$= \sqrt{1/3}\,(\langle yz, \sigma| - i\langle zx, \sigma| - \langle xy, -\sigma|)x|j_i = 1/2, m_i = \pm 3/2\rangle$$
$$= \begin{cases} 0 \\ (-iN/\sqrt{24}) \end{cases}$$

$$\langle j_{eff} = 1/2, m_{jeff} = 1/2 | x | j_i = 1/2, m_i = \pm 1/2 \rangle$$
$$= \sqrt{1/3}\,(\langle yz, \sigma| - i\langle zx, \sigma| - \langle xy, -\sigma|)x|j_i = 1/2, m_i = \pm 1/2\rangle$$
$$= \begin{cases} (-iN/\sqrt{8}) \\ 0 \end{cases}$$

$$\langle j_{eff} = 1/2, m_{jeff} = -1/2 | x | j_i = 1/2, m_i = \pm 3/2 \rangle$$
$$= \sqrt{1/3}\,(\langle yz, -\sigma|+i\langle zx, -\sigma| + \langle xy, \sigma|)x|j_i = 1/2, m_i = \pm 3/2\rangle$$
$$= \begin{cases} (iN/\sqrt{24}) \\ 0 \end{cases}$$

$$\langle j_{eff} = 1/2, m_{jeff} = -1/2 | x | j_i = 1/2, m_i = \pm 1/2 \rangle$$
$$= \sqrt{1/3}\,(\langle yz, -\sigma|+i\langle zx, -\sigma| + \langle xy, \sigma|)T(1,0)|j_i = 1/2, m_i = \pm 1/2\rangle$$
$$= \begin{cases} 0 \\ (iN/\sqrt{8}) \end{cases}$$

Finally, the transition rate of $L_3$-edge is finite and the branching ratio is infinite.

However, when a $CuO_4$ tetrahedron is distorted by the Jahn-Teller effect, the ground state of the compressed tetrahedron is $|xy\rangle \otimes |\pm\sigma\rangle$. In this case, the transition rate of $L_2$-edge is $N^2/5$ and that of $L_3$-edge is $(9 - \sqrt{6})N^2/25$, and the branching ratio is finite (~1.3, this

branching ratio depends on the polarization of incident beam. One can find a condition of polarization to make the branching ratio of 2 by setting $\boldsymbol{A} \cdot \boldsymbol{p} = A_x p_x + A_y p_y + A_z p_z$).

# References

[Ref.A1] Leonard I. Schiff, *Quantum Mechanics. Third Edition* (McGraw-Hill Companies, New York, 1968).

[Ref.A2] B. J. Kim, Hosub Jin, S. J. Moon, J.-Y. Kim, B.-G. Park, C. S. Leem, Jaejun Yu, T. W. Noh, C. Kim, S.-J. Oh, J.-H. Park, V. Durairaj, G. Cao, and E. Rotenberg, Phys. Rev. Lett. **101**, 076402 (2008).

[Ref.A3] Daniel I. Khomskii, *Transition Metal Compounds*, (Cambridge University Press, Cambridge, 2014).

# Publication lists

[1] Choong H. Kim*, Ara Go*, **Hwanbeom Cho*** (*equal contribution), Santu Baidya, Vladimir V. Gapontsev, Byeong-Gwan Cho, Deok-Yong Cho, Taehun Kim, Younghak Kim, Tae Yeong Koo, Sergey V. Streltsov, Daniel I. Khomskii, Hosub Jin, and Je-Geun Park, "Spin-orbital-entangled $J_{\text{eff}}$=1/2 state in 3*d* transition metal oxide $CuAl_2O_4$", (under review at Nature Communications).

[2] Jaeseok Son, Byung Cheol Park, C. H. Kim, **Hwanbeom Cho**, So Yeun Kim, L. J. Sandilands, C. H. Sohn, Je-Geun Park, S. J. Moon, and T. W. Noh, "Phonon renormalization via the Dzyaloshinskii-Moriya interaction in 5*d* pyrochlore iridates", submitted.

[3] Suhan Son, Matthew J. Coak, Nahyun Lee, Jonghyeon Kim, Tae Yun Kim, Hayrullo Hamidov, **Hwanbeom Cho**, Cheng Liu, David M. Jarvis, Philip A.C. Brown, Jae Hoon Kim, Cheol-Hwan Park, Daniel I. Khomskii, Siddharth S. Saxena, and Je-Geun Park, "Bulk properties of van-der-Waals hard ferromagnet $VI_3$", Phys. Rev. B **99**, 041402(R) (2019).

[4] Pyeongjae Park, Joosung Oh, Klára Uhlířová, Jerome Jackson, András Deák, László Szunyogh, Ki Hoon Lee, **Hwanbeom Cho**, Ha-Leem Kim, Helen C. Walker, Devashibhai Adroja, Vladimír Sechovský, Je-Geun Park, "Magnetic Excitations in Non-Collinear Antiferromagnetic Weyl Semimetal $Mn_3Sn$", npj Quantum Materials **3**, 63 (2018).

[5] Garam Han, Sungkyun Choi, **Hwanbeom Cho**, Byungmin Sohn, Je-Geun Park, and Changyoung Kim, "Structural investigation of the insulator-metal transition in $NiS_{2-x}Se_x$ compounds", Phys. Rev. B **98**, 125114 (2018).

[6] Woo Jin Kim, John H. Gruenewald, Taekoo Oh, Sangmo Cheon, Bongju Kim, Oleksandr B. Korneta, **Hwanbeom Cho**, Daesu Lee, Yoonkoo Kim, Miyoung Kim, Je-Geun Park, Bohm-Jung Yang, Ambrose Seo, and Tae Won Noh, "Unconventional anomalous Hall effect from antiferromagnetic domain walls of $Nd_2Ir_2O_7$ thin films", Phys. Rev. B **98**, 125103 (2018).

[7] **Hwanbeom Cho**, Marie Kratochvílová, Nahyun Lee, Hasung Sim, and Je-Geun Park, "Frustrated antiferromagnetic honeycomb-tunnel-like lattice Cu$R_2Ge_2O_8$ ($R$=Pr, Nd, Sm, and Eu)", Phys. Rev. B **96**, 224427 (2017).

[8] **Hwanbeom Cho**, Marie Kratochvílová, Hasung Sim, Ki-Young Choi, Choong Hyun Kim, Carley Paulsen, Maxim Avdeev, Darren C. Peets, Younghun Jo, Sanghyun Lee, Yukio Noda, Michael J. Lawler, and Je-Geun Park, "Properties of spin-1/2 triangular-lattice antiferromagnets $CuY_2Ge_2O_8$ and $CuLa_2Ge_2O_8$", Phys. Rev. B **95**, 144404 (2017).

[9] R. Nirmala, Kwang-Hyun Jang, Hasung Sim, **Hwanbeom Cho**, Junghwan Lee, Nam-Geun Yang, Seongsu Lee, R. M. Ibberson, K. Kakurai, M. Matsuda, S-W Cheong, V. V. Gapontsev, S. V. Streltsov, and Je-Geun Park, "Spin glass behavior in frustrated quantum spin system $CuAl_2O_4$ with a possible orbital liquid state", J. Phys.: Condens. Matter **29**, 13LT01 (2017).

[10] X B Yan, Y Xu, L P He, J K Dong, **Hwanbeom Cho**, D C Peets, Je-Geun Park, and S Y Li, "Nodeless superconductivity in the noncentrosymmetric superconductor BiPd", Supercond. Sci. Technol. **29**, 065001 (2016).

## 국문초록

# 새로운 구리 2+ 산화물을 기반으로 한 양자 자성 연구

조환범
물리천문학부 물리학전공
서울대학교 대학원

응집물질물리학에서 양자 자성은 고전적으로는 예측될 수 없는 강한 양자역학적인 요동에 의해 유도되는 새로운 현상들에 초점이 맞춰진 흥미로운 분야이다. 특별히 산화수가 2+인 구리산화물은 스핀-$S$ = 1/2의 강한 양자 요동과 큰 쿨롱 상호작용 때문에 양자 스핀 액체, 반강자성 삼각격자에서의 $uud$ 상전이, 그리고 스피논 (spinon), 홀론 (holon), 오비톤 (orbiton)으로의 전자 붕괴와 같은 양자 자성을 연구하는데 있어 유망한 대상이 되어 왔다. 이 논문에서 강한 양자 요동과 전자 상관의 상호작용으로 인해 유도되는 새로운 현상들을 새 구리 산화물 시스템인 $CuAl_2O_4$와 $CuR_2Ge_2O_8$ ($R$ = Y, La)을 연구함으로써 발견하였다.

스핀-궤도가 얽혀진 유사 스핀 상태인 $J_{eff}$ = 1/2는 Kitaev 양자 스핀 액체와 같은 발현 현상과 연관되어 있어 응집물질물리에서 흥미로운 주제가 되었다. 이 상태를 연구하기 위해서 4$d$나 5$d$ 전이금속 화합물들이 많은 주목을 받아왔었던 반면 3$d$ 시스템은 주목받지 못하였다. 이는 3$d$ 이온의

스핀-궤도 결합이 루테늄 (4d)이나 이리듐 (5*d*) 이온보다 작기 때문이며 많은 3*d* 시스템이 궤도 각운동량의 소멸을 야기하는 뒤틀린 결정 구조를 갖기 때문이다. 하지만 이 연구를 통해서 구리 산화물 $CuAl_2O_4$에서 $J_{eff}$ = 1/2 state가 나타남을 입증하였다. 엑스선 회절 및 구리 K-끝머리 엑스선 흡수에 의해 확인된 결정 구조의 입방 대칭성은 $J_{eff}$ = 1/2의 발현을 지지한다. 또한 구리 L-끝머리 엑스선 흡수는 $J_{eff}$ = 1/2 상태 발현의 직접적인 증거를 제공한다. 더욱이 이 시스템의 격자 반전은 쩔쩔맴 상태에 있는 $J_{eff}$ = 1/2 파동함수의 강한 양자 요동과 더불어 자기 모멘트의 장거리 정렬을 막고 스핀-궤도가 얽힌 $J_{eff}$ = 1/2에 대한 유리 상태를 유발시킨다.

다음 연구는 새로운 이차원 양자 반강자성 시스템인 Cu$R_2$Ge$_2$O$_8$ ($R$ = Y와 La)에 초점을 맞추었다. 고분해능 엑스선 그리고 중성자 회절 실험 분석에 의하면, Cu$R_2$Ge$_2$O$_8$의 구리 그물망은 *b*축에 수직하게 약한 결합으로 연결되어 있는 이차원 삼각 격자를 나타낸다. 0.08에서부터 400 K까지의 덩치 성질은 Cu$R_2$Ge$_2$O$_8$가 각각 이트륨 시스템에서는 0.51(1) K 그리고 란타넘 시스템에서는 1.09(4) K에서 장거리 정렬함을 보인다. 또한 흥미롭게도 이들은 자기장에 의해 유도되는 특이한 상전이를 보여준다. 이론적인 이해를 위해 밀도 함수 이론 (DFT) 띠 구조 계산이 수행되었고 그 결과 띠틈이 약 2 eV인 전형적인 전하-전달류의 (charge-transfer type) 부도체임을 확인하였다. 종합해보면, 이러한 관측결과들은 Cu$R_2$Ge$_2$O$_8$ ($R$ = Y, La)가 낮은 온도에서 자기 정렬이 있는 이차원 양자 스핀 삼각 반강자성체의 추가적인 사례가 되도록 한다.

**주요어:** 양자 자성, Mott 부도체, 스핀-궤도 결합, 쩔쩔맴, 구리 산화물, 스피넬, 삼각격자, 시료 합성.

**학 번:** 2013-20384

# 감사의 글

The studies in this thesis could not have been carried out without the help and support of many people. I would like to express my appreciation first of all to my supervisor Je-Geun Park for mentoring me over the period of my Ph.D. course. His insights guided me to study topics in spin-orbital coupling in 3 transition metal compounds and to find novel frustrated systems. He has supported me to learn how to manage a project as well as experimental skills on characterizing bulk properties of samples, and gave me assistance to analyze the data and write this thesis. I genuinely thank him for his patience and confidence in me.

I would especially like to thank Dr. Matthew Coak for his kind help on revision of this thesis and interview preparation for my next position in Oxford.

I also want to thank Prof. Kee Hoon Kim, Cheol-Hwan Park, Dohun Kim, and Yukio Noda for examining this thesis and giving me warm advice to help me complete it.

The success of the studies could be accomplished with the aids of experimental and theoretical collaborators. I would like to thank Prof. Yukio Noda for helping me analyze x-ray and neutron diffraction data. I would like to thank Prof. Donghoon Seoung, Prof. Hiroyuki Kagi, and Dr. Kazuki Komatsu for helping me acquire and analyze high-pressure XRD data. I would like to thank Prof. Masashi Takigawa, Dr. Hikaru Takeda, Mr. Nobuyoshi Mera, Prof. R. Nimala, and Dr. Peter Baker, for helping me conduct the NMR and SR experiment. I would like to Dr. Maxim Avdeev in ANSTO and Carley Paulsen of CNRS for neutron diffraction and low-temperature magnetic measurements, respectively.